Subsidence, Exhumation, and Overpressure of the Fish Creek Vallecito Basin Within the Northern Gulf of California Rift

By

ELAINE K. YOUNG
DISSERTATION

Submitted in partial satisfaction of the requirements for the degree of

DOCTOR OF PHILOSOPHY

in

Earth and Planetary Sciences

in the

OFFICE OF GRADUATE STUDIES

of the

UNIVERSITY OF CALIFORNIA

DAVIS

Approved:

Michael E. Oskin, Chair

Dawn Sumner

Magali Billen

Committee in Charge

2023

For Jasper

TABLE OF CONTENTS

LIST OF FIGURES

LIST OF FIGURES, CONTINUED

LIST OF TABLES

LIST OF PLATES

ACKNOWLEDGEMENTS

This work was partially supported by NSF/GSA Graduate Student Geoscience Grant # 12952-20, which is funded by NSF Award # 1949901. Additional support from a USGS EDMAP Program award to Oskin and Young, Mildred E Mathias Graduate Student Research Grant Program Award, a UC Davis Earth and Planetary Sciences Durrell Award, and an AGeS award to Young. This material is based upon work supported by the National Science Foundation under Grant Nos. EAR-1759200 and EAR-1759353. Any opinions, findings, and conclusions or recommendations expressed in this material are those of the authors and do not necessarily reflect the views of the National Science Foundation. Thank you to the AGeS program for its support. Mineral separations and apatite (U-Th)/He analyses conducted at the UTChron Laboratories (U-Th)/He lab - thank you to the students in there for their help. Fieldwork was supported by the Steele-Burnand Anza Borrego Desert Research Center and Anza Borrego Desert State Park; thank you specifically to Elaine Tulving and Jim Dice for their field support. This research and dissertation benefited greatly from conversations and collaborations with Dawn Sumner, Magali Billen, Sujoy Mukhopadhyay, Susan Kidwell, Codey Colleps, Danny Stockli, Rudra Chatterjee, Rebecca Dorsey, Gary Axen, Janis Hernandez, and Francesca Rodriguez. Thank you to Levi Pettyjohn, Amelia Rutan, Allison Pang, Veronica Guerra, Angelo Campiglio, Cassidy Ross, Ryan Malloy, Hannah Zampaglione, Danée Felix, Layla Mustafa, Huy Le, Kyle Mui, Mary Young, Andy Young, and Elizabeth Grant for their assistance in the office and the field - without them this work would not be possible. Thank you to my advisor, Mike Oskin, for his exceptional mentorship and understanding during unprecedented times. Last, thank you to my family and friends for their unwavering support.

DISSERTATION ABSTRACT

Subsidence, Exhumation, and Overpressure of the Fish Creek Vallecito Basin Within the Northern Gulf of California Rift

The Fish Creek Vallecito basin (FCVB) provides an extensive and continuous exposure of strata equivalent to the modern Salton trough rift basin in the northernmost Gulf of California. The FCVB exposes a continuous ~6 km thick sedimentary section deposited between 8 and 1 Ma. However, compaction of strata in the FCVB appears inconsistent with ~6 km burial, requiring an alternative structural and depositional model and/or anomalously high pore-pressure conditions. To test these hypotheses, I present geologic mapping that documents new fault strands and associated stratigraphic facies changes between FCVB and the Vallecito Mountains. I show that basin subsidence was partitioned across two normal fault hanging walls: the newly identified Proto-Vallecito fault, active from ~8 to 4.4Ma, and the West Salton Detachment fault, which accelerated after ~4.4 Ma and ceased activity at ~1 Ma. My structural model reduces the total burial depth required of the FCVB section from ~6 km to a maximum of ~4 km and requires significantly lower and less rapid exhumation than previous models. I validate my structural model using (U-Th)/He (AHe) thermochronology. Preservation of detrital age signatures and sparse AHe ages younger than the depositional ages imply that temperature at the base of the FCVB section may not have exceeded the AHe partial retention zone (<~55-80°C). To extract additional information from the AHe data, I use a combination of forward and inverse modeling to constrain post-depositional thermal histories while considering the effects of radiation damage and detrital inheritance. From the dates and modeling, I determine that maximum burial temperature of the FCVB was about 80-90°C and confirm that the burial depth of the exhumed

section was likely ≤4km. Best-fit thermal histories from inverse modeling are consisted with uplift and tilting commencing as early as 4Ma, when activity shifted to the West Salton Detachment, and 3 Myr prior to the onset of transpression at 1.2 Ma. Using this newly established structural context, I use a one-dimensional model of basin deposition and compaction to test for overpressure conditions in the FCVB. The model results show that overpressure conditions likely developed here due to both rapid sedimentation and the presence of low permeability caprock layers. Such overpressure conditions may be present in the modern Salton Trough, promoting earthquake triggering and fault creep in this region.

CHAPTER 1

Evidence for partitioned subsidence of the Fish Creek-Vallecito basin in the Salton Trough, Northern Gulf of California

ABSTRACT

Exposures along the Gulf of California provide a rare insight into early continental margins prior to burial by passive margin depositional processes. The late Miocene to Pleistocene Fish Creek Vallecito Basin (FCVB), a subbasin of the Salton Trough in the northern Gulf of California, is a key reference section for major events like the arrival of the Colorado River to the Gulf of California and provides an extensive and continuous exposure of strata equivalent to the modern Salton trough. This study uses geologic mapping and stratigraphic facies changes between Fish Creek Wash and the Vallecito Mountains to examine the structural controls of subsidence of the FCVB, the magnitude of subsidence, and the mechanism and amount of uplift. The proto-Vallecito fault is identified and mapped, new basin-margin units are added to the FCVB stratigraphy, and an updated structural history for the FCVB is proposed. This new mapping and stratigraphy show that FCVB subsidence was partitioned across two normal fault hanging walls, the proto-Vallecito fault from ~8-4.4 Ma and the West Salton Detachment fault from ~4.4 (or older) to ~1 Ma. This partitioning reduces the total burial depth of the FCVB section along Fish Creek Wash to ~4 km, and the updated structural model requires significantly lower exhumation rates and magnitudes than previous structural models. These updates bring the structural history in better alignment with prior stratigraphic observations.

INTRODUCTION

The Gulf of California is one of the few localities actively transitioning from continental rupture to seafloor spreading. It provides a rare insight into what early continental margins look like before they are deeply buried by passive margin depositional processes (Axen and Fletcher, 1998). The Salton Trough, which is the northern portion of the Gulf of California rift, is characterized by rapid deposition from the Colorado River Delta that initiated almost immediately after rifting began (Dorsey et al., 2011). As a result, the new crust formed here is transitional and composed mostly of sediment with some magmatic crust (Fuis et al., 1984; Dorsey et al., 2007; Han et al., 2016). The Fish Creek-Vallecito basin (FCVB), a subbasin of the Salton Trough, preserves a 5.5 km thick, late Miocene to Pleistocene sedimentary archive of the formation of the Salton Trough and northern Gulf Extensional Provence, including the introduction of Colorado River-derived sediment, and the transition from rifting to strike-slip faulting through the Peninsular Ranges in the past 1.2 Ma (Figure 1.1, Dorsey et al., 2011, 2012).

The FCVB is a key reference location for understanding major events like the Gulf of California marine incursion, the arrival of the Colorado River to the Gulf of California, and ultimately, the formation of landmarks like the Grand Canyon. The FCVB section also provides an extensive and continuous exposure of strata equivalent to the modern stratigraphy and depositional setting in the Salton trough. The FCVB thus offers an opportunity to understand sedimentary and, by proxy, hydrologic conditions at seismogenic depths in the Salton trough without the need for expensive deep drilling projects. Several major fault zones, like the San Andreas, San Jacinto, Elsinore, Imperial, etc., are located in or near the Salton trough, so

understanding how the depositional setting affects fault behavior is important for understanding fault mechanics as well as seismic hazards.

The purpose of this study is to understand the structural controls of subsidence of the FCVB and, from this information, constrain the mechanism and amount of uplift that has occurred since basin deposition ceased ca. 0.9 Ma. This problem is important for confirming if this exposure reveals part of the upper seismogenic zone (>4 km depth, Harris, 2017; Ross et al., 2019), analogous to the presently active San Andreas fault and other faults present within the Salton Trough. Dorsey et al. (2012) proposed that the entire 5.5 km of FCVB strata were deposited in the hanging wall of the West Salton Detachment fault (Model1, Figure 1.2), a major rift-bounding low-angle normal fault (Shirvell et al., 2009 *and references therein*). In contradiction to this model, the lower marine part of the FCVB section contains proximally derived coarse sediments from upper-plate basement rocks of the Vallecito Mountains and Fish Creek Mountains. This observation suggests that the FCVB may have been deposited over a set of basin-and-range style normal faults (Model2, Figure 1.2) rather than only in the hanging wall of the West Salton Detachment fault.

Model 1 assumes relatively consistent stratigraphic thickness throughout the basin and thus implies 5.5 km of burial (Figure 1.2). The compaction of strata in the FCVB appears inconsistent with ~5.5 km burial, requiring an alternative structural model, anomalously high pore-pressure conditions, or both. In its present-day configuration, the FCVB exposes a complete section from basement rocks to Quaternary sediments. Model 1 suggests that 5.5 km of strata and underlying basement rocks were uplifted and eroded in the last 1.2 million years at a rate of >4 mm/yr. Such rapid exhumation rates are unusual, and as such, one would expect

to find significant shortening structures underlying the basin to explain this rapid uplift. Alternatively, if the basin was deposited over multiple normal faults, as shown in Model2, the depth of burial may have been much less than the total sediment thickness, reducing the amount of subsequent uplift and erosion required.

To address the structural controls for subsidence and uplift of the FCVB, I present new geologic mapping of the basin between Fish Creek Wash and the Vallecito Mountains, focused along the present-day left-lateral Vallecito fault. This work 1) redefines the stratigraphy proximal to the Vallecito fault, 2) documents the presence of a proto-Vallecito normal fault through outcrop exposures and stratigraphic relationships, and 3) provides an updated and detailed structural analysis of the FCVB. I conclude that the lower basin strata interfinger with facies derived from the foot wall scarp of the proto-Vallecito fault, indicating that it originated as one of a set of Mio-Pliocene normal faults that controlled early basin subsidence. This proto-Vallecito fault may have acted as an early breakaway of the West Salton detachment fault, partitioning FCVB subsidence into at least two subbasins and allowing for reduced (<5.5 km) burial of the lower FCVB section. I also compile my mapping with adjacent mapping (Todd 1977; Winker and Kidwell, 1996; Dibblee 1996; Kairouz, 2005; Shirvell, 2006; and Dorsey et al., 2012) to produce a uniform, detailed geologic map of the northern FCVB. On the basis of this mapping, I conclude that the uplift and exhumation of the FCVB could have been accomplished through the observed folding and tilting of basin strata, without a need to invoke a large amount of reverse motion on faults east of the FCVB.

BACKGROUND

Tectonic Setting

The FCVB is located ~35 km southwest of the Salton Sea and about 40 km north of the US-Mexico border in the Salton Trough (Figure 1.1). The region marks an important transition of the Pacific-North American plate boundary, where the southern San Andreas fault system (SAFS) ends and the Gulf of California extensional province (GEP) begins. Throughout the GEP there are a series of right-lateral faults connecting rift segments that have been accommodating nearly all of the plate boundary motion in this region since ~6Ma (Oskin et al., 2001; Oskin and Stock, 2003; Bennett and Oskin, 2014). In the southern Gulf of California, extension has progressed to seafloor spreading with magnetically lineated oceanic crust (Larson et al., 1968; DeMets, 1995). In the northern Gulf of California continental rupture is recent, and most of the crust is not-yet broken but extremely thinned from extension (Martin-Barajas, 2013; Han et al., 2016; van Wijk et al., 2019).

The Salton Trough comprises the Coachella Valley, Salton Sea, Imperial Valley, and Mexicali Valley. The Salton Trough began as a normal-fault-bound, terrestrial basin that transitioned to an evaporitic basin around 7 Ma, eventually becoming a marine basin around 6 Ma due to breaches in overlapping extensional basins during the development of the Gulf of California Seaway (Umhoefer et al., 2018). The Salton Trough was then translated north via the San Andreas fault system, eventually passing through the axis of the Colorado River Delta to its present-day location (Dorsey et al., 2011). The Salton Trough is now the northern onshore equivalent to the Gulf of California (Han et al., 2016), with several right-lateral strike-slip faults

separated by extensional stepovers. Early extension in the Salton Trough was accommodated on the Miocene-Pleistocene active low-angle West Salton Detachment fault, with total displacement estimated at 8-10km (Shirvell et al., 2009; Dorsey et al., 2011). At ~1.2 Ma (Dorsey et al., 2012), right-lateral faults initiated within the Salton Trough to the west of the San Andreas fault, including the San Felipe fault, the San Jacinto fault, and the Elsinore fault. These strike-slip faults crosscut and offset exposures of the West Salton Detachment and remain active today as part of the southern San Andreas fault system.

The FCVB is situated north of the Elsinore fault system and south of the San Felipe and San Jacinto fault systems and, along with the surrounding mountain ranges, contains exposures of the West Salton Detachment along its western and northern margins (Figure 1.1. In the FCVB there are active right-lateral faults trending northwest-southeast, parallel to the major right-lateral faults, as well active left-lateral faults oriented approximately perpendicular to the right-lateral systems (Dorsey et al., 2012; this study). There are three important faults surrounding the eastern, basal exposures of the FCVB: the Vallecito fault, the Split Mountain fault, and the Fish Creek Mountain fault. The Vallecito fault is an active, northeast-striking fault that hosts scarps indicative of recent left-lateral slip (Dorsey et al., 2012; this study). In this study, I show that the Vallecito fault had an earlier extensional history. The Split Mountain fault has undefined slip direction that occurs along a strike from the Split Mountain Anticline within the Fish Creek Mountains. The Fish Creek Mountains fault bounds basement exposures east of the FCVB. This fault is enigmatic; its age, current level of activity, and sense of motion, both now and in the past, are not well documented. The FCVB strata are folded into west-plunging anticline-syncline pairs with wavelengths decreasing from ~5km to ~1 km from south to north.

The Split Mountain anticline, located at the northeastern end of Split Mountain Gorge, is a member of this fold set and exposes the lowest part of the FCVB strata and basement rocks in its core. The youngest and uppermost part of the FCVB stratigraphy (≤1.2 Ma), located in the southwestern FCVB, displays fanning dips indicative of tilting after ~1.2 Ma (Dorsey et al., 2012).

Prior Mapping in the FCVB

The geology of the FCVB and surrounding region has been studied since the mid-1900s (Figure 1.3), with early mapping by T.W. Dibblee conducted in the 1940s (available in Dibblee 1996). Prior mapping in this region exists at a variety of scales. The southern part of the region lies on the El Cajon USGS 30'x60' quadrangle (Todd, 2004). The top half lies on the Borrego Springs 30'x 60' quadrangle that is in the process of being mapped by the California Geological Survey. As part of that mapping effort, there are 7.5' quadrangles with preliminary geologic mapping, including the Agua Caliente Springs quadrangle (Todd, 1977) from which some of the lines, foliation measurements, and unit labels used in the compilation were derived. Detailed prior mapping focused on the basin strata was conducted by Woodard (1963), by Kerr (1982; 1984, et al., 1979), and by Winker (1987; and Kidwell, 1996) in the late 1970s-early 1980s. These detailed maps were focused on documenting the stratigraphic history of the FCVB, and those papers set the nomenclature that most authors use in the area today. The map by Winker and Kidwell (1996) used in this compilation was made at 1:12,000 to 1:20,000 using USGS topographic base maps and aerial photographs. Later detailed mapping includes two master's theses by Kairouz (2005) and Shirvell (2006) at scales of 1:12000 and by Dorsey et al. (2012) at scales of 1:10,000-20,000, also using a topographic base and aerial photographs. Figure 1.4

shows how the map units for this compilation were broken out or combined overtime by the authors of the maps used and by this study. This study attempts to reconcile differences in map units between the compiled maps, especially where new units were defined outside of the canonical stratigraphy described below. These differences were reconciled into the map units presented here through detailed reading of the descriptions, inspection of available field photographs and diagrams, and field checking where possible. The abbreviated descriptions of map units are in Plate 1.

Stratigraphic Overview

Sediments in the FCVB have two sources. The first is the surrounding higher topography of the Peninsular Ranges (local or L-suite), and the second is the Colorado River (C-suite). L-suite sediments are plagioclase-rich and typically contain small pebbles and coarse sand of crystalline rocks, mostly tonalite, from the Peninsular Ranges batholith and associated metamorphic framework rocks, as well as fragments of volcanic rocks and reworked nonmarine sediments capping the range (Winker and Kidwell, 1996). L-suite beds are often slightly darker in color compared to C-suite beds. C-suite sediments are distinguished by well-rounded and well-sorted grains with orange to red hematite coatings. C-suite marine siltstone and claystone are generally gray or pale yellow (Winker and Kidwell, 1996). Colorado River sediments first appeared in the FCVB at 5.3 Ma (Dorsey et al., 2007; 2011). Crow et al. (2021) proposes a later arrival of Colorado River sediment at 4.80-4.63 Ma; however, this younger date requires stratigraphic duplication by faults cutting the FCVB that is not yet documented. Significant deposition of Colorado River-derived sediments into the FCVB continued until about ~2.8 Ma (Dorsey et al., 2011). Inter-fingering of Colorado River-derived and local sediments occurred

during the early and late phases of Colorado River deposition in the FCVB (Winker and Kidwell, 1986; Dorsey et al., 2007, 2011). As Colorado River deposition progressed, the depositional setting transitioned from marine to fluvial deltaic with progradation of the Colorado River delta and tectonic translation past the river mouth, which is fixed to the North America plate at Yuma, Arizona (Winker and Kidwell, 1986; Dorsey et al., 2007, 2011). This transition in depositional setting accompanied a transitional return to locally sourced units. The FCVB strata are also characterized based on facies – proximal facies, which I interpret as foot-wall scarp derived, and distal facies. Most distal facies are C-suite, and all proximal facies are L-suite, but some L-suite units are proximal, and others are distal. This division is imperfect and subjective because of the inherently transitional and gradational nature of facies changes within the basin. With that caveat, these distinctions are a useful way of describing and classifying the units mapped in the FCVB.

The FCVB strata are a 5.5-6 km thick succession of southwest-dipping late Miocene (~8 Ma) to Pleistocene (<0.8 Ma) (Dorsey et al., 2011, 2012) rocks canonically divided into three Groups: the Split Mountain Group, the Imperial Group, and the Palm Spring Group as defined by Winker (1987) and Winker and Kidwell, (1996) and others. Most of the stratigraphic nomenclature used in describing these suites of basin strata is from Winker (1987) and Winker and Kidwell (1996). Similarly, the stratigraphic descriptions are primarily from Winker (1987) and Dorsey et al. (2011), and stratigraphic thicknesses are from Dorsey et al. (2011). Figure 1.3 shows the evolution and development of FCVB stratigraphy and nomenclature from 1951 to 1996. This study adds additional units to the stratigraphy with a focus on proximal facies. The

previously reported stratigraphy will be described following a northeast to southwest transect up section and approximately parallel to Fish Creek Wash.

Crystalline Rocks and pre-FCVB Conglomerate and Breccia

The Vallecito Mountains, Fish Creek Mountains, and the FCVB basement rocks are all Paleozoic to early Mesozoic meta-sedimentary and early Cretaceous meta-volcanic rocks intruded by the eastern Cretaceous Peninsular Ranges batholith. The lower plate rocks in the foot wall of the West Salton detachment fault and the Vallecito fault are mostly Late Cretaceous La Posta pluton (Todd, 1977). This mostly tonalite pluton intruded the Granite Mountain pluton and Paleozoic to Jurassic metasedimentary rocks that occur as relatively spatially limited outcrops of schist and gneiss. These crystalline rocks will be referred to collectively as the basement. Where stratigraphic units are in depositional contact with basement rocks (nonconformities), there is often a thin layer of grus (gs) at the base of the strata.

Perched on the crystalline basement in the Vallecito Mountains is a conglomerate, interbedded with coarse-grained sandstone that has gravel-sized Eocene Poway type clasts (pcgl; Kairouz, 2005; Abbott and Smith, 1978; Kies and Abbott, 1983). Below parts of this conglomerate is a grus layer. Unit pcgl is interpreted by Kairouz (2005) as braided stream deposits that include reworked grus. Kairouz (2005) also describes four breccias located east of Whale Peak in the Vallecito Mountains. Two of these breccias (Tbx1&2), located northeast of Hapaha Flat, are interpreted stratigraphically as Neogene rock fall deposits that sit unconformably on pcgl, however there is no independent age control for these units (Kairouz,

2005). The other two breccias (Tbx3&4) described by Kairouz (2005) are located near the southeastern end of the Vallecito fault and will be described with the basin stratigraphy below. In this study, the breccias described by Kairouz (2005) are mapped as four distinct map units due to a lack of certainty in correlating these breccias with other map units. Further investigation focused on these breccia outcrops could allow for unit correlation and grouping.

FCVB stratigraphy, as previously documented along Fish Creek Wash

The Split Mountain Group (Miocene) is composed of nonmarine L-suite clastic sedimentary rocks and is divided into the Red Rock Formation, the Elephant Trees Formation, and the lower megabreccia. The mid-Miocene Red Rock Formation, composed of alluvial and eolian sandstone, is, according to Winker and Kidwell (1996), exposed as a small sliver in the core of the Split Mountain anticline in Split Mountain Gorge. The late Miocene Elephant Trees Formation is an alluvial fan conglomerate with sandstone derived from proximal alluvial fans plus distal alluvial fans and streams. In the Split Mountain area, the Elephant Trees Formation is about 500 m thick, thinning to the east (Dorsey et al., 2011). Paleomagnetic dating puts the Elephant Trees at ~8-6.5 Ma (Dorsey et al., 2011). Within the map area, the Elephant Trees Formation consists of boulder conglomerate with thick debris flow beds to ripple laminated sandstone and siltstone and is interpreted to be alluvial fan deposits (Kerr 1982, 1984; Winker and Kidwell, 1996). Some previous studies differentiated the Elephant Trees fan conglomerates based on color (e.g. Kerr 1982, 1984), but Winker (1987) maps them as a single unit with upper and lower subunits. Winker's upper Elephant Trees Formation is described as being laterally continuous with the transitional unit in the lower Lycium member. The arbitrary boundary between transitional Lycium and Elephant Trees is placed at Split Mountain Gorge on maps by

Winker (1987). The Elephant Trees Formation was broken out into three different units by Shirvell (2006): Elephant Trees, lower sandstone member (Me1) is an arkose sandstone interbedded with gritty sandstone. Elephant Trees, conglomerate member (Me2) is a clast-supported cobble to large boulder conglomerate. And Elephant Trees, upper sandstone member (Me3) is a well-bedded course debris-flow sandstone interbedded with pebbles and with boulder conglomerate in medium-grained sandstone. It is likely that Shirvell's (2006) lower sandstone member is equivalent to the Red Rock Formation mapped in Split Mountain Gorge (Winker 1987) and described by Winker and Kidwell (1996). The Red Rock Formation described in Winker and Kidwell (1996) is interpreted to be a sandstone, possibly channel filling, between basement rocks and rift-related alluvial fan conglomerates. For the purposes of this map compilation, I use the more recent nomenclature and include the lower sandstone as part of the Elephant Trees Formation (Me1) (Figure 1.4). Shirvell (2006) maps a basal grus unit below the lower sandstone member, which I incorporate into the Me1 map unit. I also group the conglomerate member and upper sandstone member described by Shirvell (2006) into one map unit (Me2+3). The late Miocene lower megabreccia is a long-runout nonmarine landslide-derived megabreccia sourced from the Vallecito Mountains (Kerr and Abbott, 1996), the thickness of which varies along strike but is ~50 m thick in Split Mountain Gorge.

The Imperial Group (late Miocene-early Pliocene) is composed of both L-suite and C-suite marine fossiliferous clastics, limestones, and evaporites, and is divided into the Fish Creek Gypsum, the Latrania Formation, and the Deguynos Formation. The Fish Creek Gypsum is a thin layer of marine gypsum and anhydrite separating the lower megabreccia in the Split Mountain Group from the Latrania Formation in the Imperial Group. The late Miocene to early Pliocene

Latrania Formation is a ~350 m thick exposure of L-suite marine clastics and has five members exposed in the FCVB: the Lycium member, the upper megabreccia, the Wind Caves member, and the Stone Wash member (Winker and Kidwell, 1996). The Lycium member is ~100 m thick and composed of L-suite marine turbidite-like sandstone with conglomerates. The upper megabreccia is a long-runout marine subaqueous landslide megabreccia sourced from the Fish Creek Mountains (Rightmer and Abbott, 1996) and is <50 m thick, although thickness varies along strike. The Wind Caves member is ~150 m thick and composed of interbedded C-suite and L-suite turbidite sandstones, with a greater proportion of L-suite derived sediments towards the base of the member. This unit represents the oldest recognized input from the Colorado River into the FCVB. The early Pliocene Deguynos Formation is a ~1050 m-thick deltaic succession of C-suite marine clastics. The Deguynos Formation is traditionally divided into the Mud Hills member, the Yuha member, and the Camel's Head member, based on facies changes consistent with Colorado River delta progradation: The Mud Hills member is the prodelta offshore marine facies, the Yuha member is the marine delta platform, and the Camels Head member is the marginal marine delta front. Winker and Kidwell (1996) map and describe an additional unit, the Lavender Canyon member, which is a delta front marine sandstone within the Deguynos Formation. The Stone Wash member is a time-transgressive unit consisting of conglomerate with L-suite sandstone that is laterally continuous with the Lycium member, the Wind Caves member, and the Mud Hills member. Proximal facies of the Stone Wash member are fossiliferous, while distal facies tend to be fossil-poor sediment gravity flows. The Jackson Fork member is a marginal marine L-suite sandstone and conglomerate mapped as laterally

continuous with the Camels Head member and the base of the Palm Spring Group by Winker (1987).

The Palm Spring Group (mid Pliocene-early Pleistocene) is composed of nonmarine clastics with the transition out of C-suite sediments occurring near the base of the Group. It is divided into the Diablo Formation, the Olla Formation, the Tapiado Formation, the Hueso Formation, the Borrego Formation/Bow Willow Beds, and the Canebrake Conglomerate. The Diablo Formation (also referred to as the Arroyo-Diablo) is ~1000 m thick C-suite fluvial sandstone, siltstone, and claystone deposited as part of the nonmarine Colorado River deltaic succession. The Olla Formation is ~1400 m thick, interbedded C-suite and L-suite fluvial sandstone, siltstone, claystone, and conglomerate; the thickness of this unit is known to vary along strike, and much of the Olla Formation is laterally continuous with the Diablo Formation. Together, the Diablo and Olla Formations are the youngest C-suite units in the FCVB. The Hueso Formation thickness varies but is, on average, 700m, and it is composed of fluvial L-suite sandstone with siltstone and conglomerate. The Tapiado Formation also has variable thickness and is an L-suite lacustrine deposit containing two layers of tuff that are 2.6 and 2.65 Ma (Dorsey et al., 2011). The Tapiado Formation is laterally continuous with the Hueso Formation. The Canebrake Conglomerate consists of alluvial fan and scarp-derived landslide deposits and is an L-suite conglomerate laterally continuous with the Hueso, Tapiado, and Olla Formations. The age of the Canebrake Conglomerate spans essentially the entirety of the Palm Spring Group.

Quaternary Units

Non-bedrock Quaternary units include suites of terraces throughout the basin, alluvial fans along the range fronts, and alluvium in washes with ephemeral flow. There are a few generations of significant terraces, all of which are composed of gravels of varying thicknesses that cover the bedrock units. On some of these terraces, there are Poway-type clasts. In the study area, the terraces generally grade away from the Vallecito Mountains and into the center of the FCVB. Based on preliminary observations, the terraces do not seem to be strongly tilted. A Quaternary monolithic breccia with chloritically altered tonalite (Qbx) defined by Kairouz (2005) is mapped along the western margin of the Vallecito Mountains near Whale Peak.

Structures

The Vallecito Fault is previously mapped as an east-dipping or near-vertical fault with left strike-slip and/or oblique dip-slip motion (e.g., Kerr, 1982; Winker 1987; Winker and Kidwell, 1996; Shirvell, 2006; Dorsey et al., 2012). Previous studies speculated on the importance of the Vallecito Fault for early FCVB deposition, especially with respect to the Elephant Trees Formation (e.g. Kerr 1982; Shirvell 2006; Shirvell et al., 2009) and to explain why the timing of rapid subsidence on the WSDF is ~3 Ma younger than the oldest FCVB strata. However, a normal-fault trace for the Vallecito fault was not documented, and the Quaternary active trace seems to contradict the paleocurrent indicators from the basal units in the section (Kerr, 1982; Winker and Kidwell, 1996). Geologic observations that favor the Vallecito fault playing a role in early FCVB deposition are the stratigraphic thickening of the Elephant Trees and other alluvial fan conglomeratic facies towards the Vallecito range front while also thinning

to the east and the presence of locally sourced coarse deposits interfingering with the deltaic sequence in a ribbon roughly parallel to the range front.

The east-dipping West Salton detachment fault (WSDF) occurs as a series of discontinuous sinuous traces throughout the western half of the map area. The WSDF is cut and separated by younger faulting in the region, particularly by the Elsinore fault zone. All of the stratigraphy described in this study with the exception of Quaternary surficial units, occurs in the hanging wall of the WSDF.

There are two previously mapped regions with west plunging folding. The first occurs in the base of the section in Split Mountain Gorge and consists of the Split Mountain anticline-syncline pair. The core of the Split Mountain anticline exposes crystalline basement rocks. The Split Mountain folds occur along strike from the Split Mountain fault and the Gypsum Quarry fault. The northwest to south striking Split Mountain fault has crystalline basement rocks and subsequent FCVB strata occurring on its southwestern side. The second region of folding occurs in the middle upper part of the section in the Palm Springs Group and is located southeast of Whale Peak and West of the southern tip of the Vallecito fault. These folds are also west plunging, and their wavelengths decrease from 5 km to 1 km from south to north.

METHODS

Geologic mapping for this study was conducted in the field on lidar-derived topographic maps at a scale of 1:10,000 (USGS 2021, 3DEP). The map compilation and digital preparation were done using GIS (Geographic Information System) software and are at a scale of 1:12,000. The

compilation mapping was field checked and verified with high-resolution topography from lidar (USGS,2021, 3DEP) and full-color aerial photographs (USDA-FSA-APFO, 2016, NAIP). Structural analysis using stereonets and the creation of a geologic cross-section supplement support the interpretations made from the mapping.

RESULTS

Stratigraphy

The stratigraphy described above is based on a combination of units and descriptions from Winker and Kidwell (1996), Kairouz (2005), Shirvell (2006), and Dorsey et al. (2012). Each time the FCVB near the Vallecito Mountains and Whale Peak was mapped by a new author, additional coarse, proximal facies were broken out, especially towards the bottom of the section. This study correlates unit descriptions across maps and breaks out a new set of units (Figure 1.4), several of which are time transgressive.

I define new units along the Vallecito fault toward the base of the FCVB section. These units are described below and are a zone of tectonically brecciated crystalline basement, sedimentary breccia (sbx), a megabreccia (mbx), and a unit of interbedded silt and conglomerate, herein named the silty Stone Wash member (ssw). I also revisit and expand the definitions for the Stone Wash and Jackson Fork Members. These units are time-transgressive, locally sourced, range-front mantling and foot-wall scarp-derived deposits that generally strike parallel to the range front (broadly northeast) and dip to the southeast. These units interfinger with the canonical stratigraphy, a relationship that is clearly documented at and above the

Lycium member but is difficult to document with clear contacts at the base of the section where the Elephant Trees and the sedimentary breccia are nearly indistinguishable. The relative stratigraphic relationships of these units in the lower FCVB are shown in Figure 1.5, and their locations within the FCVB are on Plate 1.

Proximal to the Vallecito range, where the Elephant Trees Formation and the Lycium Member are in contact with each other rather than separated by the lower megabreccia, I mapped the contact between them as the boundary between the coarse conglomerates and the sandstone respectively. I observed large cobble to boulder-sized clasts in basal beds of the sandstone unit that I interpreted to be the Lycium member (Figure 1.6). I make this distinction because these course beds also appear higher up section away from the contact, proximal to the Vallecito range front, in what is mapped as Lycium according to both Winker (1987) and Shirvell (2006). Therefore, I map these coarser clasts as a basal subunit, or more proximal facies, contained within the Lycium member and not as part of the alluvial fans in the Elephant Trees Formation. Either way, these sandy beds with sparse large clasts or basal conglomerate beds mark the transition from alluvial fan and debris flow deposition to marine deposition that is indicated by the transition from the Elephant Trees and lower megabreccia into the Lycium member in Split Mountain Gorge along Fish Creek Wash. This is a good example of the along strike facies changes and inter-fingering of proximal facies with the marine facies of the basin observed throughout the lower FCVB section.

There are three breccias along the Vallecito fault: a tectonically brecciated basement breccia, a sedimentary breccia, and a megabreccia. The tectonically brecciated basement is heavily fractured basement that lacks disarticulation, meaning features like dikes can be traced

continuously across clasts (Figure 1.7). This tectonic breccia is mapped as part of the basement unit and is indicated by an overlay pattern on the map where observed. The sedimentary breccia (sbx) is an angular, poorly sorted conglomerate supported by a fine silt matrix and exhibiting subtle stratification (Figures 1.8 and 1.9). The megabreccia (mbx) is a clast-supported megabreccia composed of shattered and disarticulated clasts of basement rock (Figure 1.10). Gradationally mantling the sedimentary breccia and megabreccia is a matrix-supported conglomerate unit with cobble-sized clasts and a silty to sandy matrix. This conglomerate may be interpreted as a subunit of the sedimentary breccia but is distinct enough that I mapped it as a separate unit. The tectonically brecciated basement and the sedimentary breccia are time transgressive, occurring relatively continuously throughout lower FCVB deposition. The tectonically brecciated basement is found throughout the entire section, while the sedimentary breccia is restricted to the lower FCVB. Both the tectonically brecciated basement and sedimentary breccia first occur along strike of the Elephant Trees Formation. The last outcrop of sedimentary breccia is located along strike from the Yuha member of the Deguynos Formation.

The Stone Wash member of Winker (1987) is maintained, but its extent is redefined in my mapping. The Stone Wash member (Figures 1.11, 1.12, and 1.13) is laterally equivalent with Wind Caves and Mud Hills members, and it typically extends much further away from the range front and into the basin compared to the other proximal units. While most of the proximal facies occur with an approximately range front parallel strike and dip into the basin, the Stone Wash member is often conformable with the basin strata (i.e., Mud Hills and Wind Caves

members), especially where it occurs closer to the basin axis. The Stone Wash member also extends farther from the range front into the basin compared to other proximal facies.

A yellow-tan, well-bedded alternating conglomerate and sandstone with a silty matrix (ssw) forms a locally time transgressive unit that is typically found overlying the sedimentary breccia, between the basin strata and the sedimentary breccia (Figure 1.14). Unit ssw interfingers with the Mud Hills member of the Deguynos Formation and with the sedimentary breccia in some places. At the northeastern extent of ssw, it interfingers with Mud Hills and occurs along strike from the Lycium member. This occurrence of ssw along strike from the Lycium member was previously mapped by Shirvell (2006) as a coarse facies of the Mud Hills member. However, given my observations of this unit elsewhere along the range front, its distinct sedimentary properties, and its approximately range-parallel bedding orientation, I do not consider this part of the Mud Hills member.

The Jackson Fork member is a marginal marine L-suite sandstone and conglomerate. In this contribution, I expand the definition of the Jackson Fork member to include additional marginal marine L-suite sandstone beds laterally equivalent to the Deguynos Formation. I observe the Jackson Fork member deposited directly on the basement, brecciated basement, and conformably upon sedimentary breccia and along strike from and depositionally interfingered with the Yuha and Camels Head members and the Olla Formation. This expansion is consistent with descriptions of the Jackson Fork member by Winker (1987), where the unit generally grades from conglomeratic at the base to sandy at the top. My newly mapped exposure is to the east of prior mapped exposures and is coarser than the exposures

immediately to the west up section (Figure 1.15). My mapped exposure also sits directly on the basement rocks or the sedimentary breccia.

Near the south end of the Vallecito fault, there are two megabreccias (Tbx3&4) originally mapped by Kairouz (2005) intercalated with the lowermost Canebrake Conglomerate. These breccias crop out in a localized area <1 km across and are not mapped elsewhere. As originally mapped, these breccias were correlated with outcrops of Elephant Trees Formation that I reinterpret as part of the Canebrake Conglomerate. The first breccia (Tbx3) has angular igneous and metamorphic clasts and is matrix-supported with boulders 1-2m and as large as 4m. The second, Tbx4, has angular tonalite clasts 10-50 cm and as large as 1-2m supported by a matrix of crushed and pulverized tonalite. Tbx4 is markedly similar to my new units of sedimentary breccia and tectonically brecciated basement (indicated by overlay polygons on Plate 1). Despite these similarities, I maintain separate unit names and descriptions due to the significant geographic and stratigraphic distance between the units. Additional investigation is required to determine if these units are the same. Alternatively, Tbx3&4 could be interpreted as coarse beds or debris flows within the Canebrake Conglomerate (Kairouz, 2005).

Structures

My mapping reveals a normal fault system subparallel to the Vallecito fault that is defined by buttress unconformity contact relationships between FCVB strata and basement rocks as well as by exposures of the fault in outcrop (Plate 1). The fault occurs as a series of north-northeast to south-southwest striking en echelon strands. At its northern extent within the map area, this fault occurs west of the modern Vallecito fault in the basement rocks, and to

the south of No Return Canyon, it occurs east of the strike-slip Vallecito fault and separates FCVB strata from the basement rocks. At its very southern extent, the discrete surface trace of this fault ends at a subtle anticline in the Mud Hills and Stone Wash hanging wall strata. Southwest of this anticline is a zone of distributed faulting with a small northeast striking and southeast dipping normal fault strand close to the Vallecito range front and a series of south to southwest striking and west to northwest dipping normal fault strands stepping away from the Vallecito Mountains.

In agreement with prior maps, my mapping confirms the location and morphology of a northeast striking (~025) left-lateral strike-slip fault that cuts Quaternary deposits, the Vallecito fault. This fault is located along the range front of the Vallecito Mountains and generally separates crystalline rocks from lower FCVB strata. There are two relatively continuous strands spanning 8 km across the map area and overlapping in a ~200 m left stepover for about 1km. The fault dip and dip direction changes along strike and is generally 60-85 degrees with pure left lateral to oblique left lateral kinematic indicators.

There are two broad sets of additional faulting throughout the mapped area. The first set strikes north-northwest to south-southeast and occurs primarily in the lower part of the section in the region surrounding Split Mountain Gorge between the Vallecito fault and the Fish Creek Mountains. The second set is northeast to east-northeast and southeast to west-southwest striking and occurs throughout the map area, especially in the southeast and northwest quadrants.

DISCUSSION

My new mapping and proximal stratigraphy presented above support the presence of a basin-partitioning normal fault that I call the proto-Vallecito fault. This fault is important to the early depositional history of the FCVB and allows me to propose an updated structural history for the FCVB. The proto-Vallecito fault likely partitioned basin subsidence, thus reducing the amount of both burial and exhumation needed to produce the present-day exposures of the FCVB. This updated structural model provides important context for including the FCVB in discussions of regional tectonic and geomorphic events in the northern Gulf of California.

Evidence for the proto-Vallecito Fault

At the bottom of the FCVB section, the relationships between coarse FCVB strata like the Elephant Trees Formation and the crystalline basement in the Vallecito Mountains suggest the presence of a foot wall scarp and, thus, a normal fault between the two. Paleocurrent indicators and distal thinning and pinch out of the Elephant Trees Formation to the east, near the Fish Creek Mountains, suggest a westward or southwestward source location (Winker and Kidwell, 1996). The basal sandstones below the Elephant Trees have more north-south directed paleocurrents than the alluvial fan conglomerate members of the Elephant Trees Formation (Kerr 1982, 1984, Winker and Kidwell 1996), suggesting a change in sediment source and tectonic-sedimentary setting around the onset of Elephant Trees deposition. Winker observed the proximal part of the Elephant Trees Formation as terminating abruptly against highly fractured plutonic basement in the area of No Return Canyon. The Elephant Trees Formation in my mapping likely grades into what I call the sedimentary breccia, and the two units become

nearly indistinguishable. I agree with prior work (Kerr, 1982; 1984; and Winker and Kidwell, 1996) that the Elephant Trees, or more likely the sedimentary breccia in that location, abruptly terminate against the tectonically brecciated basement. I interpret this buttress unconformity as a product of and evidence for the proto-Vallecito fault.

Observations supporting the presence of the proto-Vallecito fault as the early normal fault controlling subsidence of the FCVB continue down-section to the north and up-section to the south. To the north of No Return Canyon, the proto-Vallecito fault occurs west of the active Vallecito fault. It has significant exposure of crystalline rocks on both the hanging wall and footwall sides. On the hanging wall side, above the basement, are wedges of sedimentary breccia faulted against basement. To the south of no return Canyon, the proto-Vallecito fault is mapped as described in the results section by exposures of faulted outcrops as well as by the along strike continuation of the buttress unconformity between intact or tectonically brecciated basement and proximal facies sedimentary rocks. The discontinuous nature of the fault exposures and the interpretation of the buttress unconformity as indicating the presence of the proto-Vallecito fault is consistent with normal fault slip, especially in a region with high sedimentation rates. As the fault slips and the hanging wall is lowered, material from the foot wall is eroded and deposited on the fault trace and on the hanging wall. Fault slip may not always produce surface ruptures at the bedrock-sediment interface and, therefore, may inconsistently produce fault exposures in the proximal facies.

Previous observations of paleocurrent indicators and distal thinning of units in the lower FCVB that were thought to be inconsistent with the Vallecito fault as the early normal fault for the lower FCVB were based on comparisons with the trace of the modern Vallecito fault.

However, the orientation of the proto-Vallecito fault mapped in this study is more consistent with the paleocurrent indicators and stratigraphic thinning relationships. To further illustrate this, bedding orientations from the proximal units and from the distal units were plotted on a stereogram (Figure 1.16). When the distal units are rotated back to their original horizontal bedding position, the bedding attitudes for the proximal units rotate back to a strike and dip of 014/22, consistent with deposition of coarse facies that may have been deposited with primary inclined bedding off a north-northeast striking, east dipping fault scarp.

The pattern of foot wall tectonically brecciated basement, fault exposure in outcrop, and hanging wall proximal facies buttressed against the fault and inter-fingered with basin strata is repeated in the upper part of the FCVB along outcrops of the West Salton detachment fault. This consistent pattern of faulting and proximal deposition further reinforces the interpretation that the proto-Vallecito fault served as the primary early basin-bounding structure. The mapped geometry for the proto-Vallecito fault also supports that the present-day Vallecito fault, which is strike slip, occurs as a reactivated structure along strands of the proto-Vallecito fault (this study; Shirvell, 2006).

Duration of proto-Vallecito fault Activity

The proto-Vallecito fault was responsible for the subsidence and deposition of the lower FCVB section. The well-dated basin stratigraphy can be used to determine the duration of proto-Vallecito fault activity. As discussed above, the distal FCVB strata are depositionally inter-fingered with proximal facies derived from the normal fault scarp, which are buttressed against the foot wall of the proto-Vallecito fault. I start with the assumption that these basin strata

were approximately horizontal when deposited. The entire section, including the crystalline rocks at the base of the section, is now exposed at the surface due to tilting and exhumation. The proto-Vallecito fault experienced the same tilting and exhumation. Therefore, the present-day map relationships also show an oblique section view of the basin and proto-Vallecito fault. This allows me to use the along strike relationship between proto-Vallecito fault and proximal facies exposures to the distal FCVB basin strata to estimate the duration of proto-Vallecito fault activity. Based on these relationships, activity on the proto-Vallecito fault began around 8 Ma when it created accommodation space that allowed for deposition of the Elephant Trees Formation.

The southern end of the proto-Vallecito fault is collocated with the disappearance of the sedimentary breccia and similar facies, indicating a decline in the relative elevation of the adjacent Vallecito range at this time. The disappearance of the sedimentary breccia coincides with onset of Jackson Fork deposition and with the incursion of Marine strata into paleocanyons within the Vallecito Mountains (Figures 1.17 and 1.18). This is also where the proto-Vallecito fault becomes distributed and where deformation is accommodated on antithetic normal fault strands and by folding in the hanging wall. These changes in deposition and distribution of deformation both occur along strike from the upper Mud Hills and Yuha members, indicating that proto-Vallecito fault activity likely began to wane and cease around 4.4 Ma.

Implications of proto-Vallecito fault on FCVB History

My mapping of the proto-Vallecito fault suggests that early FCVB subsidence was partitioned between two normal faults: the proto-Vallecito fault and the West Salton detachment fault, indicating Model 2 is a more likely structural scenario. While Model 2 indicates two faults partitioned basin subsidence, I am unable to determine definitively with the data presented here whether the proto-Vallecito fault was active before or simultaneously with the West Salton detachment fault. However, the timing of increased FCVB subsidence rate with the onset of Diablo member deposition shortly after evidence for waning proto-Vallecito fault activity suggests that WSDF activity was subdued or absent while the proto-Vallecito fault was active. Subsidence of the foot wall of the proto-Vallecito fault, allowing for incursion of the Yuha member into paleocanyons, suggests an increase or onset of WSDF activity perhaps a few hundred thousand years prior to progradation of the Diablo Formation into the FCVB. In other words, the stratigraphic evidence suggests that as slip on the proto-Vallecito fault slowed, the WSDF took over. The distribution of FCVB strata around the crystalline basement rocks further supports this interpretation. The Canebrake Conglomerate wraps around the transfer zone between the proto-Vallecito fault and the WSDF at Whale Peak. There is no clear outcrop evidence for FCVB deposition northwest of the proto-Vallecito fault until after deposition of the Deguynos Formation ceases. Figure 1.19 summarizes the sequence of major depositional and tectonic events in the FCVB, as suggested by the mapping and Model2, particularly the timing of proto-Vallecito fault and WSDF activity and spatial distribution of various strata. Low-temperature thermochronology on either side of the WSDF near Whale Peak and Yaqui Ridge

suggests that rapid slip on the WSDF occurred between ~5-2 Ma (Shirvell et al., 2009), which is consistent with the observations in this study.

Based on the transition in activity from the proto-Vallecito fault to the WSDF, I construct a model for basin subsidence partitioned between these two faults. This updated structural model suggests only 2-4 km of burial for the lowermost FCVB compared to the 5.5-6 km predicted by Model 1 (Figure 1.2). This shallower burial is more consistent with the amount of, or rather lack of, compaction observed in the outcrops and hand samples of FCVB strata. From this reduced magnitude of burial, I can assume slower rates of exhumation since the onset of strike-slip faulting at 1.2 Ma (~1.6-3.3 mm/yr rather than ~5 mm/yr). Exhumation rates may be even lower if tilting is not fully recorded by the fanning dip interval in the upper Hueso Formation at the top of the section and instead began as the hanging wall tilted against the WSDF prior to the onset of strike-slip faulting.

The orientation and location of folding relative to the basin strata and basement rocks is indicative of northeast to east directed shortening. In addition to the folding, the Fish Creek Vallecito basin may have been uplifted by one or more northwest striking reverse faults. The Split Mountain fault, along strike and to the southeast of the Split Mountain anticline, is a likely candidate for accommodating a large fraction of this shortening. The Fish Creek Mountain fault also may have accommodated shortening at depth; however, with the lower exhumation predicted in this study, the observed folding in the basin combined with the faults in the Split Mountain region is sufficient to accommodate the shortening and uplift without invoking reverse slip on the Fish Creek Mountain fault. More likely, the Fish Creek Mountain fault was a normal fault, similar to the proto-Vallecito fault, that created a wedge-shaped half graben

between the two faults into which the lower basin strata were deposited. Additional mapping in the Fish Creek Mountains and low temperature thermochronology throughout the FCVB and nearby basement rocks are necessary to further test this model of FCVB exhumation. Mapping in the Fish Creek Mountains, particularly near the Split Mountain fault, is beyond the scope of this project and is made difficult by the location of the U.S. Gypsum Company and the Carrizo Impact Area.

Implications for Age of Lower Colorado River

The FCVB is an important sedimentary archive for the history of the northern Gulf of California rift, including the first arrival of Colorado River Delta sediment to the area. The Wind Caves member of the Latrania Formation, which is a mix of local and Colorado River-derived sediment, records the first arrival of Colorado River-derived sediment in the FCVB. Paleomagnetic studies and microfauna analysis date this arrival at about 5.3 Ma (Dorsey et al., 2011). However, recent Ar/Ar dates from detrital sanidine in Wind Caves sand suggest a maximum depositional age of 4.56 ± 0.04 Ma (Crow et al., 2021). Crow et al. (2021) explain this younger age by invoking duplication of approximately ~1000 m of the FCVB section via bedding-parallel fault strands formed as a southward continuation of the Earthquake Valley fault zone, a right-lateral strike-slip fault strand of the Elsinore fault system. These fault strands are only shown on a stratigraphic column and are not currently represented in published mapping. I have translated their position from the stratigraphic column and placed markers on my map in the corresponding locations (Figure 1.20). There is no evidence that the Earthquake Valley fault zone continues south into the basin from the extent mapped in the crystalline basement rocks near Whale Peak. A few sub bedding parallel faults on the map from this study intersect the

cited section at a location similar to that indicated by Crow et al. (2021). However, the small amount of separation mapped across these faults is inconsistent with that required to duplicate the section. Further, if there are large bedding parallel faults that duplicate the stratigraphic section in the center of the basin, it should also follow that there is a ramp, or section of the fault that cuts across the bedding through the section (Dorsey et al., 2021). None of the faults mapped in the Deguynos Formation or elsewhere in the C-suite section have enough separation for this. Faults with larger amounts of separation occur at the bottom of the section in the Elephant Trees Formation, often bringing the lower section and basement rocks to the surface and separating the exhumed basement from other lower strata like the Elephant Trees Formation or the Lycium member. The fault on the western side of Split Mountain Gorge, the Fish Creek fault zone, cuts nearly perpendicular to bedding with up to ~1 km of map-view separation through the Lycium member, the upper megabreccia, the Wind Caves member, the Mud Hills member, and the Yuha member. This fault is not mapped as offsetting the contact between the Yuha and Camels Head members. The Fish Creek Wash fault occurs near the easternmost location of proposed faulting by Crow et al. (2021), but it is not bedding parallel. Additionally, stratigraphic observations from the Deguynos Formation do not support the presence of section-duplicating faults; however, more detailed analysis of the section would be required to rule out duplication from the stratigraphy. My mapping follows the lower FCVB section, from the Elephant Trees Formation to the Camels Head member of the Deguynos Formation along and perpendicular to strike from Fish Creek Wash to the Vallecito fault and range front, pinning these strata to the basin margin and associated proximal facies, also without evidence for duplication of section needed to explain the results of Crow et al. (2021).

CONCLUSIONS

Based on the new and compilation mapping presented in the study, the Fish Creek Vallecito basin deposition and subsidence was partitioned across two normal faults (Model 2) rather than deposited in the hanging wall of a single normal fault (Model 1). Subsidence first occurred in the hanging wall of the proto-Vallecito fault from the deposition of the Elephant Trees Formation until deposition of the Deguynos Formation when the West Salton detachment fault became the dominant structure driving basin subsidence. Early uplift of the basin was likely accomplished through tilting during subsidence, which, when combined with the partitioned subsidence, reduces the amount of exhumation that must have been driven by the reorganization to strike-slip faulting and shortening post-1 Ma. This updated model agrees well with stratigraphic observations like paleocurrent indicators in the lower part of the section, thinning of Elephant Trees to the east, and changes from distal to proximal facies along strike from Fish Creek Wash northwest towards the Vallecito range front.

FIGURES

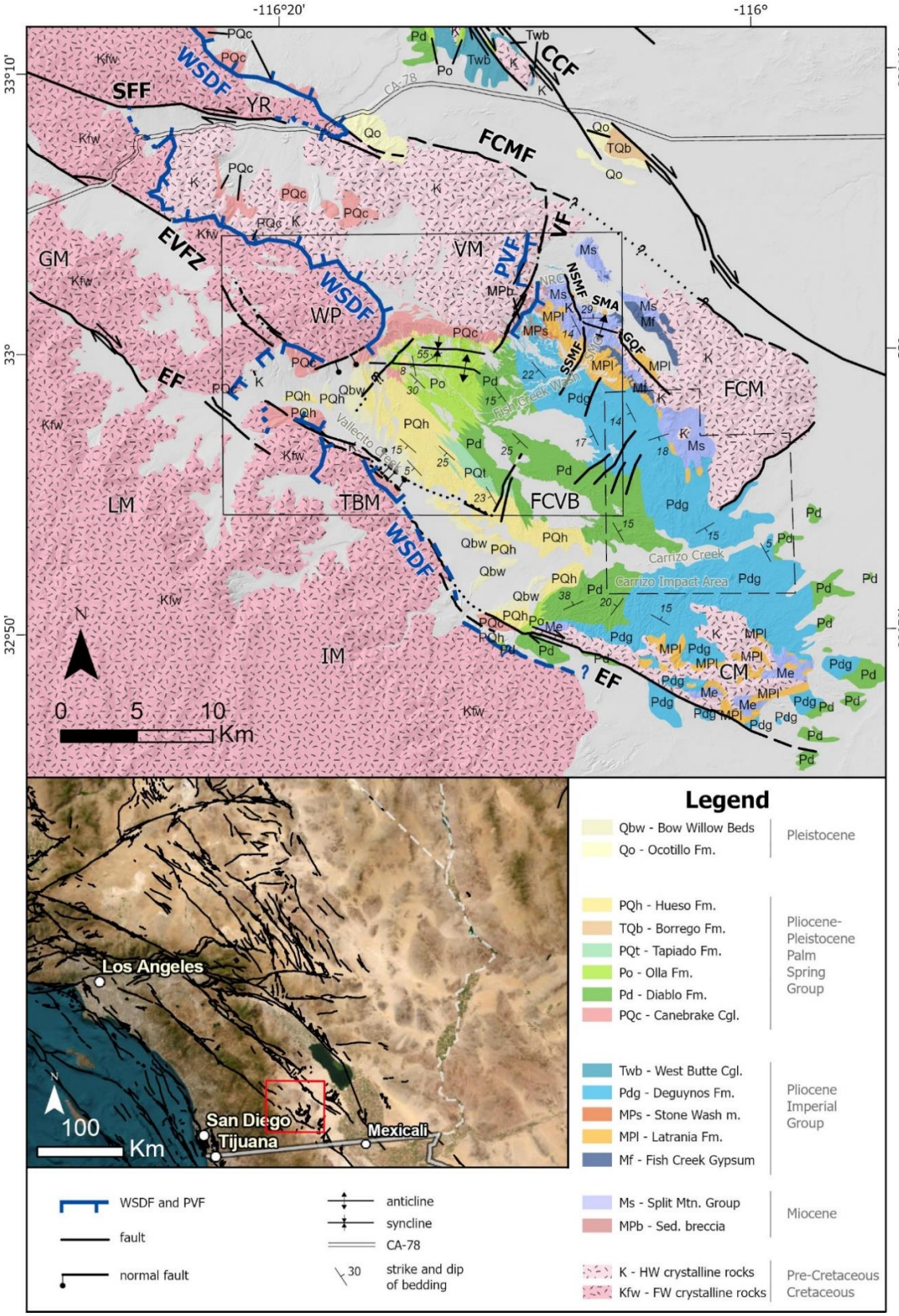

Figure 1.1. Caption on next page.

Caption to Figure 1.1: Regional geologic map of the FCVB and surrounding region with the extent of Plate 1 and the focus of this study indicated by the solid rectangle. Alluvium is not mapped. Units MPb and PQc are time transgressive, spanning the Miocene-Pliocene and the Pliocene-Pleistocene respectively; they are placed in the legend at the time of their first occurrence. Lower map shows the location of the regional map and the FCVB within southern California and the Quaternary fault and fold database (USGS and CGS). See Plate 1 for the position of the map area within the state of California. Compiled from Dorsey et al. (2011), Janecke et al. (2010), and this study.

CCF = Coyote Creek fault strand of the San Jacinto fault zone, CM = Coyote Mountains, EF = Elsinore fault, EVFZ = Earthquake Valley fault zone of the Elsinore fault system, FCM = Fish Creek Mountains, FCMF = Fish Creek Mountain fault, GM = Granite Mountain, GQF = Gypsum Quarry fault, IM = Inkopa Mountains, LM = Laguna Mountains, NRC = No Return Canyon, NSMF = Northern Split Mountain fault, PVF = Proto-Vallecito fault, SFF = San Felipe fault, SMA = Split Mountain anticline, SMG = Split Mountain Gorge, SSMF = Southern Split Mountain fault, TBM = Tierra Blanca Mountains, VF = Vallecito fault, WP = Whale Peak, WSDF = West Salton Detachment fault, VM = Vallecito Mountains, YR = Yaqui Ridge.

Hillshade in regional geologic map from USGS 3DEP, imagery in lower map from ESRI World Imagery (ESRI, 2022).

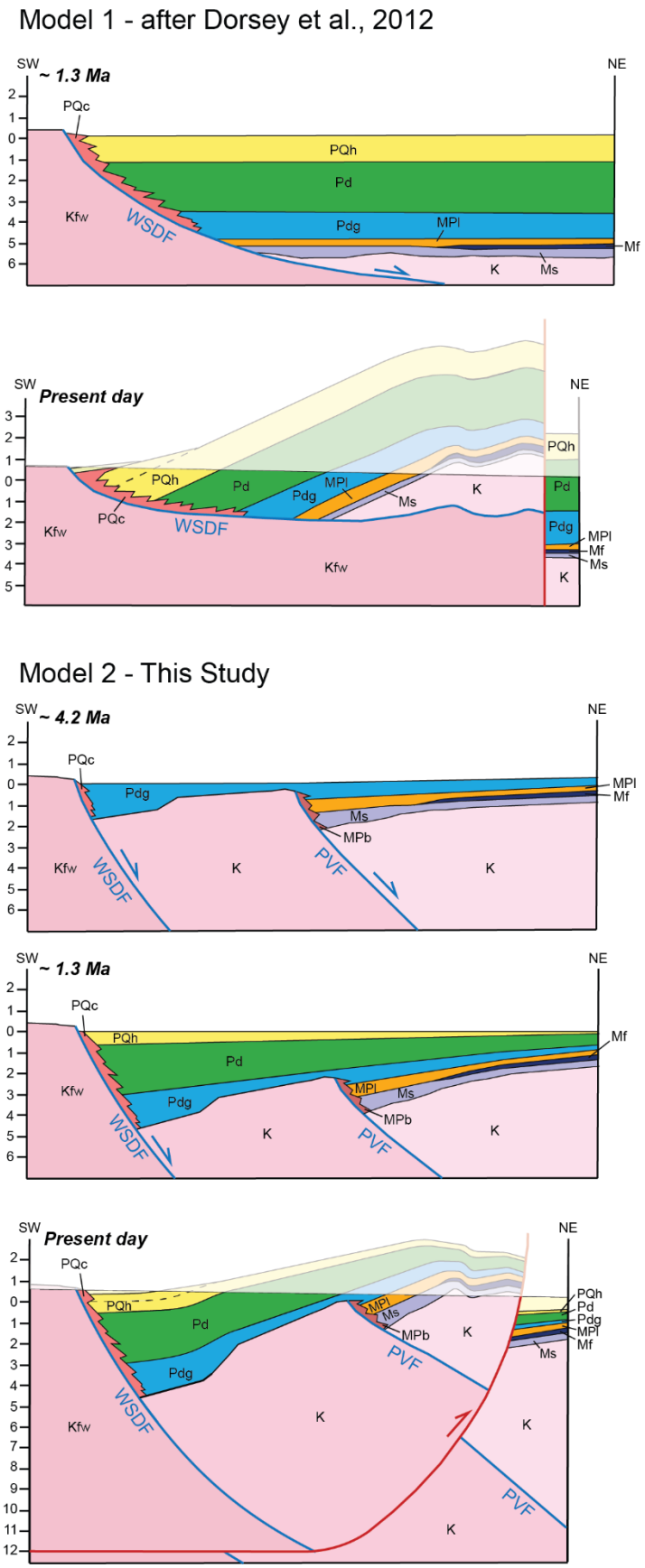

Figure 1.2. Cartoon cross-section of the FCVB approximately parallel to Fish Creek Wash. Upper: Model 1 for FCVB after Dorsey et al. (2012) where subsidence occurs only over the WSDF. Lower, Model 2 shows partitioned subsidence of the FCVB between the PVF and WSDF. WSDF = West Salton Detachment fault, PVF = proto-Vallecito fault.

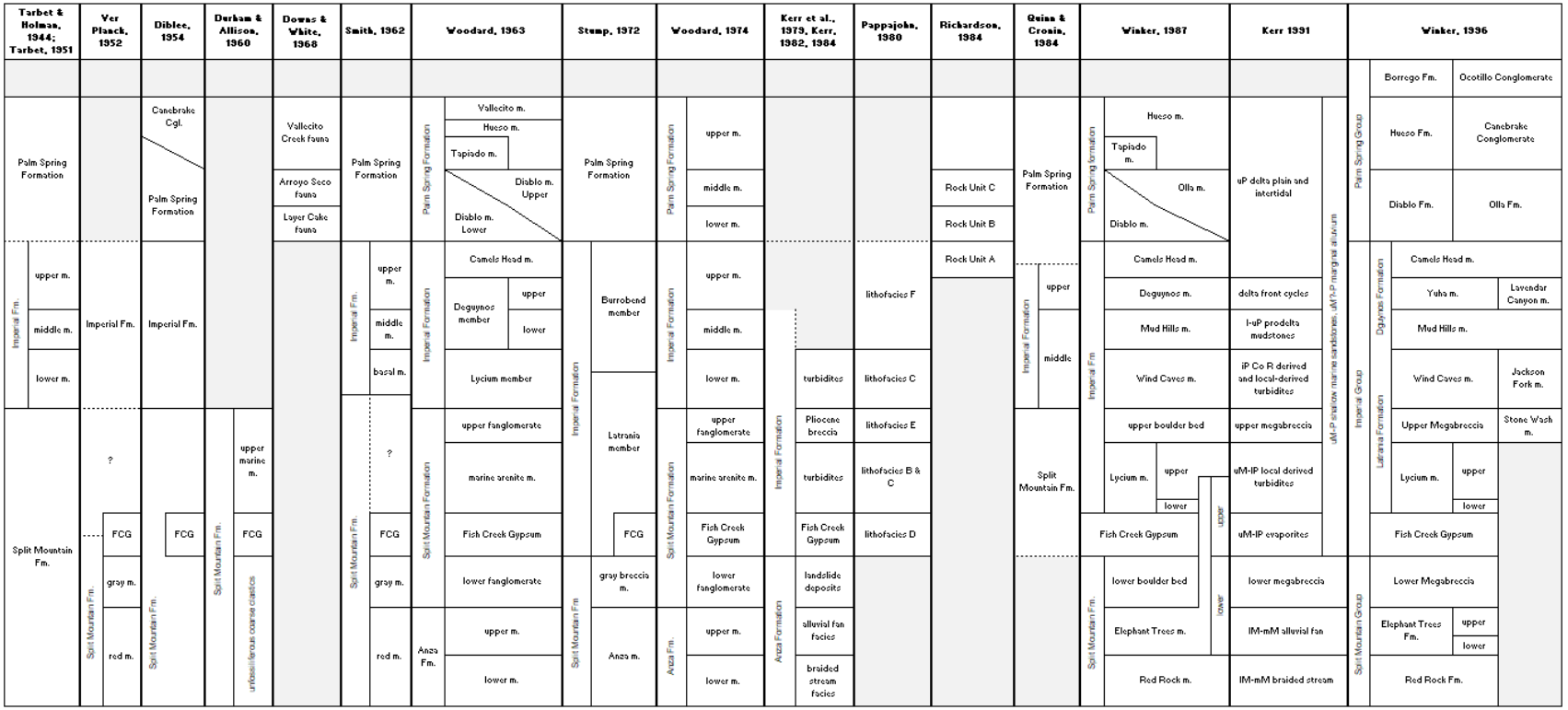

Figure 1.3. Stratigraphic synonymy for the Fish Creek Vallecito Section (Split Mtn Gorge, Split Mtn east of the gorge, and Fish Creek and Vallecito Creek Drainage Basins (Winker, 1987). Dashed lines indicate uncertain boundary placement. Grey shading indicates no unit designated by the author for this stratigraphic position. Diagonal lines separate units with lateral facies changes Modified and expanded from Winker, 1987, Figure 1.9.

cgl = conglomerate, m. = member, Fm. = Formation, FGC = Fish Creek Gypsum, uM = upper Miocene, lP = lower Pliocene, etc.

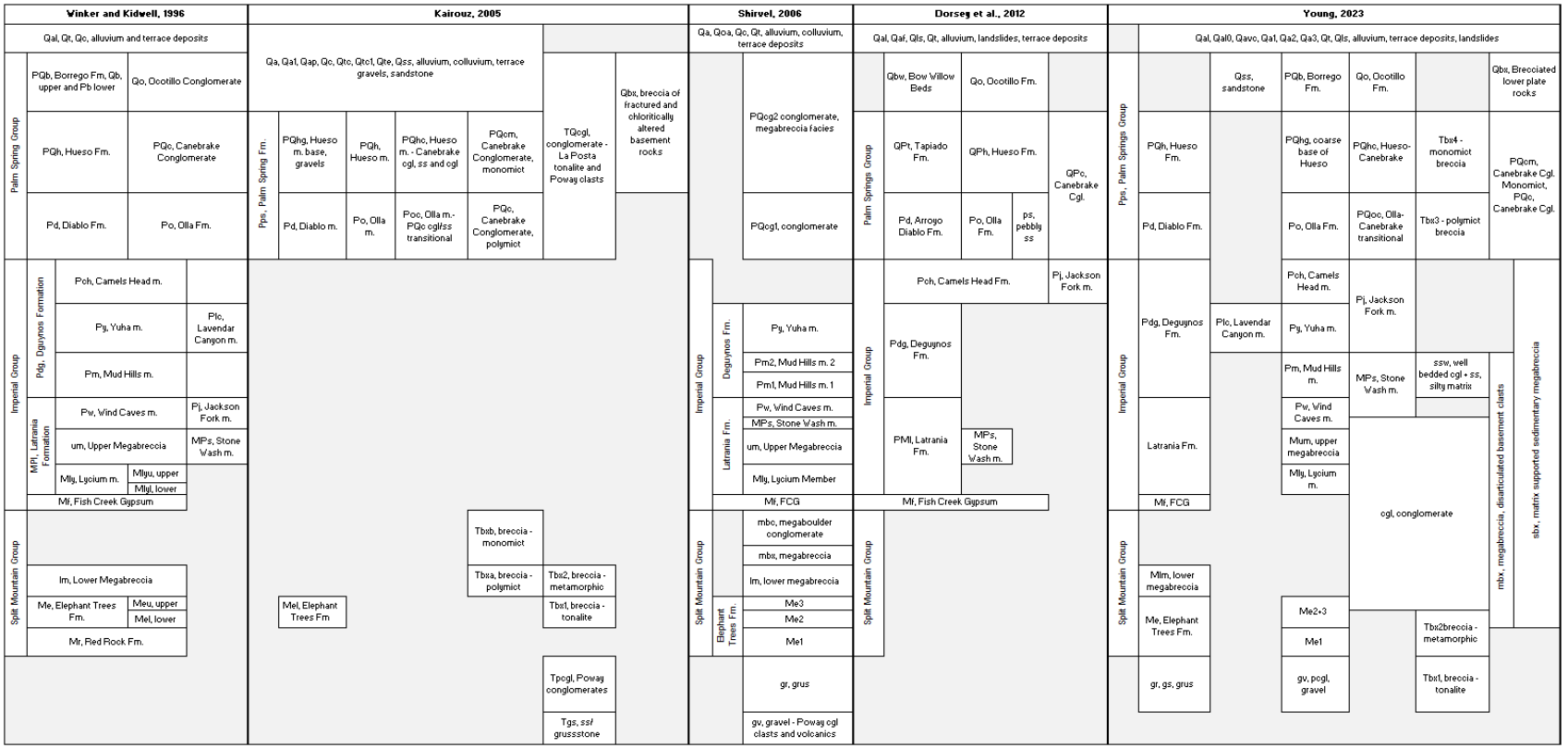

Figure 1.4. This table shows the correlation of units from maps used in the compilation mapping of this study excluding those by Diblee (1996) and Todd (1977) as those studies had simpler stratigraphy and/or less detail on their maps making such correlations unnecessary. Unit abbreviations and names are consistent with the respective authors usage. Unit names and abbreviations for Young (this study) are the same as those on Plate 1. Grey shading indicates no unit designated by the author for this stratigraphic position.

cgl = conglomerate, m. = member, Fm. = Formation, FGC = Fish Creek Gypsum, uM = upper Miocene, lP = lower Pliocene, etc.

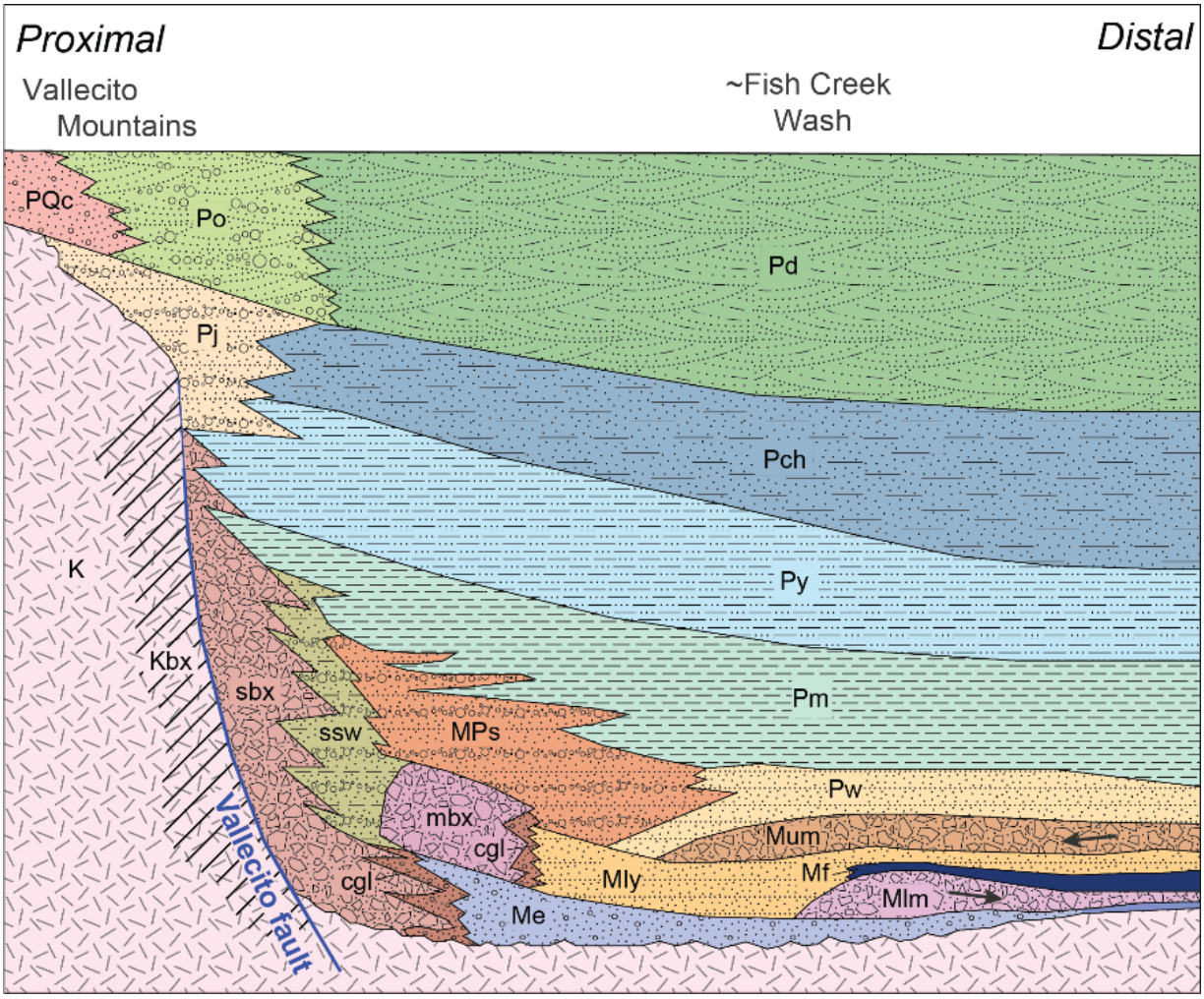

Figure 1.5. Schematic diagram of lower FCVB stratigraphy including the new proximal units defined in this study. Thicknesses and spatial relationships are relative, and the upper FCVB strata, including the true thickness of Po and Pd, are not shown. The upper FCVB stratigraphic facies panel is available in Dorsey et al., 2012. PQc = canebrake conglomerate, Po = Olla formation, Pd = Diablo formation, Pj = Jackson Fork member, Pch = Camels Head member, Py = Yuha member, Pm = Mud Hills member, sbx = sedimentary breccia, ssw = silty Stone Wash, MPs = Stone Wash member, Pw = Wind Caves member, mbx = megabreccia, cgl = conglomerate, Mum = upper megabreccia, Mly = Lycium member, Mf = Fish Creek Gypsum, Mlm = lower megabreccia, Me = Elephant Trees formation, Kbx = tectonically brecciated crystalline basement, K = crystalline basement.

Figure 1.6. Photo of the lower Lycium member with conglomerate layers. Yellow field notebook for scale. View azimuth 300. Photo location is available in the appendix.

Figure 1.7. Outcrop of the tectonically brecciated basement in foot wall of the proto-Vallecito fault (diagonal lines overlay pattern on map). The rock is shattered but not disarticulated. Yellow field notebook for scale. View azimuth 100 in upper image, 135 in lower image. Photo location available in the appendix.

Figure 1.8. Outcrop of the sedimentary breccia (sbx) and silty Stone Wash (ssw) units. View azimuth is 206. Photo location is available in the appendix.

Figure 1.9. Outcrop of sedimentary breccia (sbx) in depositional contact with the Cretaceous crystalline basement rocks (K). Note the paleotopography of the basement. View azimuth is 150. Photo location is available in the appendix.

Figure 1.10. Photo of a poorly sorted megabreccia with tonalite clasts. This outcrop is located northwest along strike of the Lycium member. View azimuth is 078. Photo location is available in the appendix.

Figure 1.11. Outcrop of the stone wash member. Matrix supported conglomerate with tonalite and metamorphic clasts. Clast size is variable between beds. View azimuth is 051. Photo location is available in the appendix.

Figure 1.12. Additional example of the stone wash member. Matrix supported conglomerate beds with tonalite and metamorphic clasts interbedded with pebbly and coarse sandstone layers. Clast size is variable between beds. View azimuth is 350. Photo location is available in the appendix.

Figure 1.13. Outcrop of the Stone Wash member (MPs) proximal to the proto-Vallecito fault near the sedimentary breccia (sbx). In this location, the two units are nearly indistinguishable as MPs has is more clast-supported, has less compositional variation in the clasts (mostly tonalite here), and has fewer sandy intervals. The obvious bedding distinguished MPs from sbx at this location. View azimuth is 065. Photo location is available in the appendix.

Figure 1.14. Photo of outcrops of the silty Stone wash (ssw) member. This unit is well stratified, has a distinct yellow color, and dips away from the proto-Vallecito fault footwall block. View azimuth is 072. Photo location is available in the appendix.

Figure 1.15. Outcrops of the Jackson Fork member newly mapped in this study. Photo is taken across a canyon from the outcrops shown. View azimuth is 300. Photo location is available in the appendix.

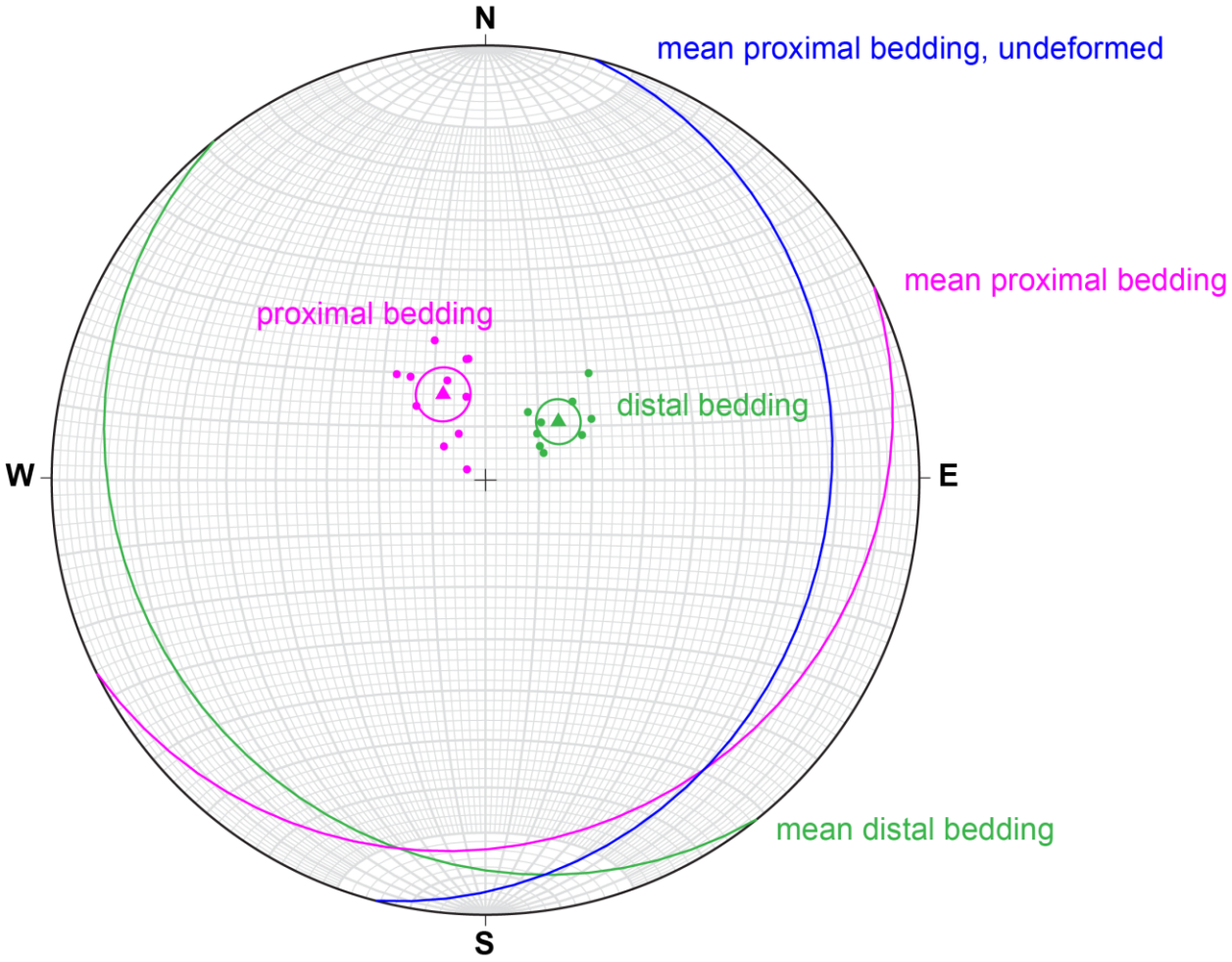

Figure 1.16. Lower hemisphere projection stereogram of the proximal and distal bedding in the northern FCVB. Attitudes used to find the mean are shown as poles, while the means are shown as planes. The mean proximal and mean distal bedding were rotated until the distal bedding was horizontal, and the resulting orientation of the undeformed proximal bedding is shown. The undeformed mean orientation of the proximal bedding is approximately parallel to and dips away from the proto-Vallecito fault, supporting the footwall scarp as the likely source for these units. This figure was produced in Stereonet v. 11.5.1 (Allmendinger et al., 2013; Cardozo and Allmendinger, 2013).

Figure 1.17. Photograph looking northwest where the Deguynos Formation (Mud Hills member, the Yuha member, and Jackson Fork member (tan outcrops below terrace surface in photograph) fill in a paleocatchment within the crystalline basement (mountainous topography) in the footwall of the proto-Vallecito fault. These outcrops are located along strike and to the northwest of the cessation of the proto-Vallecito fault. View azimuth is 330. Photo location is available in the appendix.

Figure 1.18. View of the Jackson Fork member (Pj) and the sedimentary breccia (sbx) where these units fill in a paleocanyon in the footwall of the proto-Vallecito fault. View azimuth is 330. Photo location is available in the appendix.

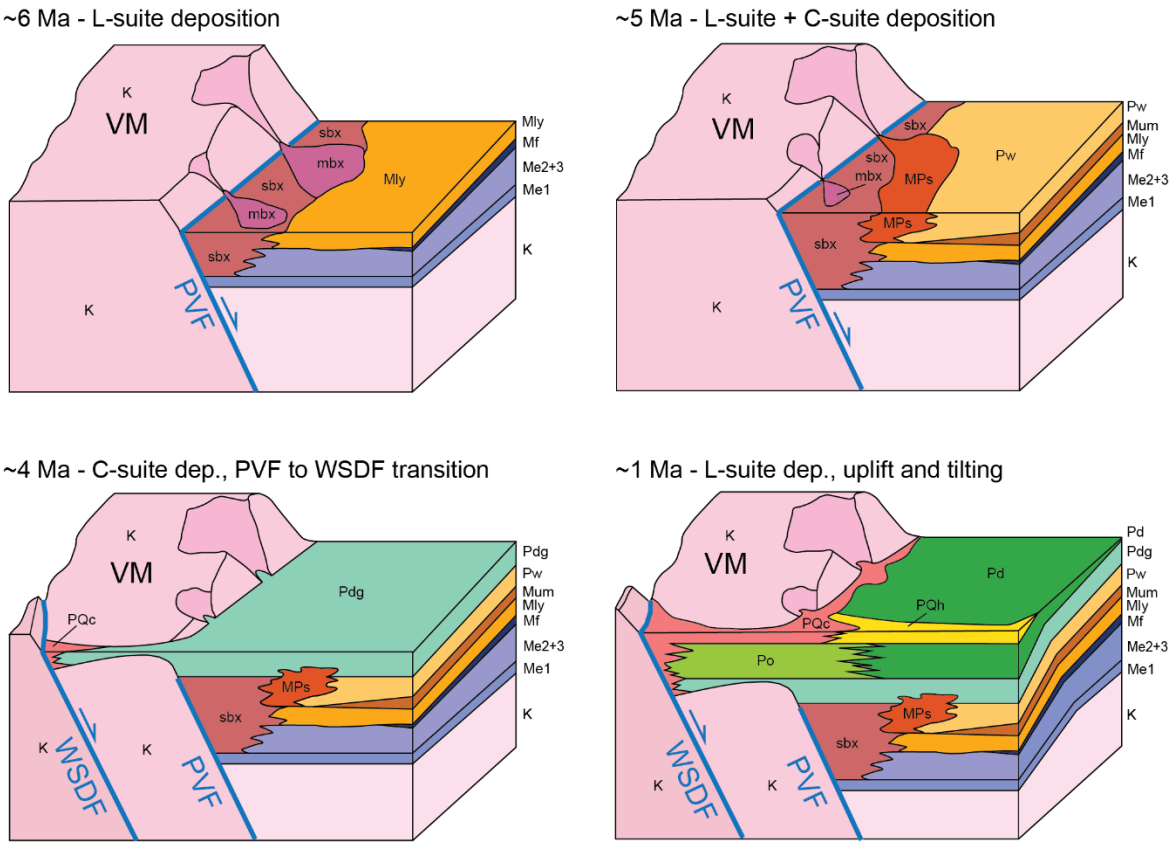

Figure 1.19. Cartoon block diagrams illustrating the tectonic and stratigraphic history of the FCVB. These blocks are intended to show stratigraphic relationships; tectonic events are an approximation since the faults are shown as planar and there is little rotation or tilting. Time 1 shows the deposition of L suite FCVB strata in the hanging wall of the proto-Vallecito fault (~6 Ma). Time 2 shows the first arrival of C-suite sediment (Pw) mixed with L-suite deposition in Pw and MPs (~5 Ma). Time 3 shows the transition from proto-Vallecito fault to West Salton detachment fault-driven subsidence, which coincides with fully C suite deposition, delta progradation, and incursion of the deltaic sequence into the paleovalleys in the Vallecito mountains (~4 Ma). Time 4 shows deposition of the upper FCVB strata prior to onset of uplift and tilting (~1 Ma).

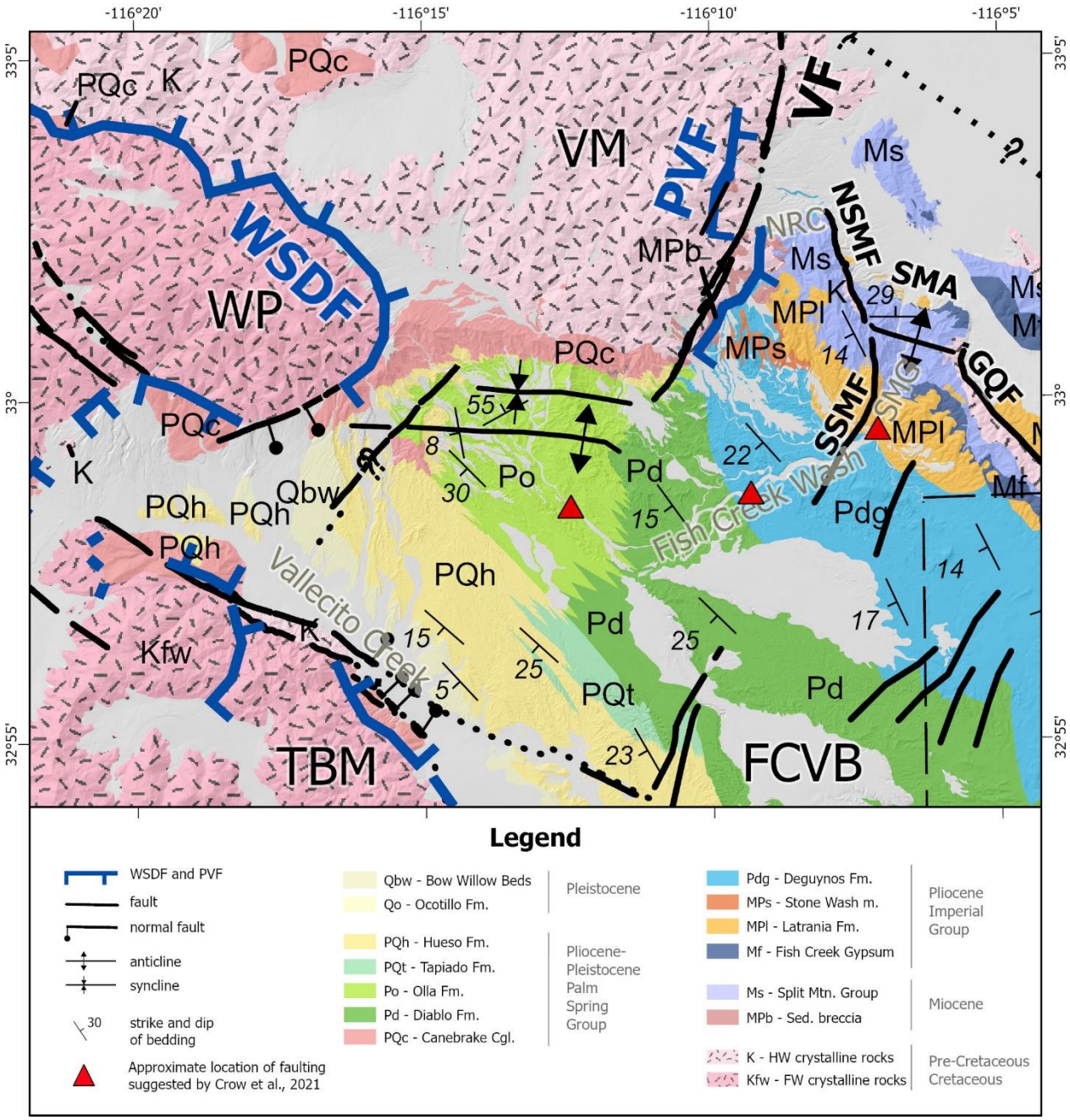

Figure 1.20. Simplified geologic map of approximately the same extent as Plate 1 showing the location of faults invoked by Crow et al. (2021) to explain proposed duplicated stratigraphic section.

REFERENCES

Abbott, P. L., and Smith, T. E., 1978, Trace-element comparison of clasts in Eocene conglomerates, southwestern California and northwestern Mexico: Journal of Geology, v. 86, p. 753-762.

Allmendinger, R. W., Cardozo, N. C., and Fisher, D., 2013, Structural Geology Algorithms: Vectors & Tensors: Cambridge, England, Cambridge University Press, 289 pp.

Axen, G.J., and Fletcher, J.M., 1998, Late Miocene-Pleistocene Extensional Faulting, Northern Gulf of California, Mexico and Salton Trough, California: International Geology Review, v. 40, p. 217–244, doi:10.1080/00206819809465207.

Bennett, S.E.K., and Oskin, M.E., 2014, Oblique rifting ruptures continents: Example from the Gulf of California shear zone: Geology, v. 42, p. 215–218, doi:10.1130/G34904.1.

Cardozo, N., and Allmendinger, R. W., 2013, Spherical projections with OSXStereonet: Computers & Geosciences, v. 51, no. 0. p. 193-205, doi:10.1016/j.cageo.2012.07.021

Crow, R.S., Schwing, J., Karlstrom, K.E., Heizler, M., Pearthree, P.A., House, P.K., Dulin, S., Jänecke, S.U., Stelten, M., and Crossey, L.J., 2021, Redefining the age of the lower Colorado River, southwestern United States: Geology, v. 49, p. 635–640, doi:10.1130/G48080.1.

DeMets, C., 1995, A reappraisal of seafloor spreading lineations in the Gulf of California: Implications for the transfer of Baja California to the Pacific Plate and estimates of

Pacific-North America Motion: Geophysical Research Letters, v. 22, p. 3545–3548, doi:10.1029/95GL03323.

Dibblee, T. W., 1954, Geology of the Imperial Valley region, California, in Jahns, R. H., ed., Geology of California, Chapter 2: Geology of the natural provinces: California Division of Mines, Bulletin 170, p. 21-28.

Dibblee, T.W., 1996, Stratigraphy and Tectonics of the Vallecito-Fish Creek Mountains, Vallecito Badlands, Coyote Mountains, and Yuha Desert, Southwestern Imperial Basin, *in* Sturzstroms and Detachment Faults, Anza Borrego State Park, California, South Coast Geological Society, Annual Field Trip Guidebook 24, p. 59–79.

Dorsey, R.J., Axen, G.J., Peryam, T.C., and Kairouz, M.E., 2012, Initiation of the Southern Elsinore Fault at ~1.2 Ma: Evidence from the Fish Creek-Vallecito Basin, southern California: SOUTHERN ELSINORE FAULT INITIATION: Tectonics, v. 31, p. n/a-n/a, doi:10.1029/2011TC003009.

Dorsey, R.J., Axen, G.J., Grove, M.J., Housen, B.A., Jefferson, G., McDougall, K., Murray, L., Oskin, M.E., Peryam, T., van Wijk, J.W., Young, E.K., 2021. Redefining the age of the loser Colorado River, southwestern United States: COMMENT. Geology, 49, e531, doi.org/10.1130/G49145C.1

Dorsey, R.J., Fluette, A., McDougall, K., Housen, B.A., Janecke, S.U., Axen, G.J., and Shirvell, C.R., 2007, Chronology of Miocene-Pliocene deposits at Split Mountain Gorge, Southern California: A record of regional tectonics and Colorado River evolution: Geology, v. 35, p. 57–60, doi:10.1130/G23139A.1.

Dorsey, R.J., Housen, B.A., Janecke, S.U., Fanning, C.M., and Spears, A.L.F., 2011, Stratigraphic record of basin development within the San Andreas fault system: Late Cenozoic Fish Creek-Vallecito basin, southern California: Geological Society of America Bulletin, v. 123, p. 771–793, doi:10.1130/B30168.1.

Downs, T., and White, J. A., 1968, A vertebrate faunal succession in superposed sediments from late Pliocene to middle Pleistocene in California, in Tertiary/Quaternary boundary: Prague, International Geological Congress 23, v. 10, p. 41-47.

Durham, J. W., and Allison, E. C., 1960, The geologic history California and its marine of Baja faunas: Systematic Zoology, V. 9, no. 2, p. 47-91.

Esri, 2022, "Topographic" [basemap]. 1:6,500,000. "World Topographic Map". https://www.arcgis.com/home/item.html?id=10df2279f9684e4a9f6a7f08febac2a9. (September, 2023)

Fuis, G.S., Mooney, W.D., Healy, J.H., McMechan, G.A., and Lutter, W.J., 1984, A seismic refraction survey of the Imperial Valley Region, California: Journal of Geophysical Research: Solid Earth, v. 89, p. 1165–1189, doi:10.1029/JB089iB02p01165.

Han, L., Hole, J.A., Stock, J.M., Fuis, G.S., Williams, C.F., Delph, J.R., Davenport, K.K., and Livers, A.J., 2016, Seismic imaging of the metamorphism of young sediment into new crystalline crust in the actively rifting Imperial Valley, California: SEISMIC IMAGING OF META-SEDIMENT: Geochemistry, Geophysics, Geosystems, v. 17, p. 4566–4584, doi:10.1002/2016GC006610.

Harris, R.A., 2017, Large earthquakes and creeping faults: Large Earthquakes and Creeping Faults: Reviews of Geophysics, v. 55, p. 169–198, doi:10.1002/2016RG000539.

Janecke, S.U., Dorsey, R.J., Forand, D., Steely, A.N., Kirby, S.M., Lutz, A.T., Housen, B.A., Belgarde, B., Langenheim, V.E., and Rittenour, T.M., 2010, High Geologic Slip Rates since Early Pleistocene Initiation of the San Jacinto and San Felipe Fault Zones in the San Andreas Fault System: Southern California, USA, in Geological Society of America Special Papers, Geological Society of America, v. 475, p. 1–48, doi:10.1130/2010.2475.

Kairouz, M.E., 2005, Geology of the Whale Peak Region of the Vallecito Mountains: Emphasis on the Kinematics and Timing of the West Salton Detachment Fault, Southern California [Masters Thesis]: University of California, Los Angeles.

Kerr, D. R., 1982, Early Neogene continental sedimentation, western Salton Trough, California [M. S. thesis]: San Diego State University, 138 p.

Kerr, D. R., 1984, Early Neogene continental sedimentation in the Vallecito and Fish Creek Mountains, western Salton Trough, California: Sedimentary Geology, v. 38, p. 217-246.

Kerr, D.R., and Abbott, P.L., 1996, Miocene subaerial sturzstrom deposits, Split Mountain, Anza Borrego Desert State Park *in* Sturzstroms and Detachment Faults, Anza Borrego State Park, California, South Coast Geological Society, Annual Field Trip Guidebook 24, p. 149 - 163

Kerr, D. R., and Kidwell, S. M., 1991, Late Cenozoic sedimentation and tectonics, western Salton Trough, California, *in* Walawender, M. J., and Hanan, B.B., eds., Geological Excursions in

Southern California and Mexico, Geological Society of America Annual Meeting, Guidebook it's been a day., p. 397-416.

Kerr, D. R., Pappajohn, S., and Peterson, G. L., 1979, Neogene stratigraphic section at Split Mountain, eastern San Diego County, California, in Crowell, J. C., and Sylvester, A. G., eds., Tectonics of the juncture between the San Andreas fault system and the Salton Trough, southeastern California: Geological Society of America, Annual Meeting, Guidebook, p. 111-124.

Kies, R. P., and Abbott, P. A., 1983, Rhyolite clast populations and tectonics in the California continental borderland: Journal of Sedimentary Petrology, v. 53, no. 2, p. 461- 475.

Larson, R.L., Menard, H.W., and Smith, S.M., 1968, Gulf of California: A Result of Ocean-Floor Spreading and Transform Faulting: American Association for the Advancement of Science, v. 161, p. 781–784.

Martin-Barajas, A., 2013, Thick deltaic sedimentation and detachment faulting delay the onset of continental rupture in the Northern Gulf of California: Analysis of seismic reflection profiles: Tectonics, v. 32.

Oskin, M., and Stock, J., 2003, Pacific-North America plate motion and opening of the Upper Delfin basin, northern Gulf of California, Mexico: GSA Bulletin, v. 115, p. 1173–1190.

Oskin, M., Stock, J., and Martin-Barajas, A., 2001, Rapid localization of Pacific-North America plate motion in the Gulf of California: Geology, v. 29, p. 459–462.

Pappajohn, S., 1980, Description of Neogene marine section at Split Mountain, easternmost San Diego County, California [M. S. thesis]: San Diego State University, 77 p.

Quinn, H. A., and Cronin, T. M., 1984, Micropaleontology and depositional environments of the Imperial and Palm Spring Formations, Imperial Valley, California, in Rigsby, C. A., ed., The Imperial Basin - tectonics, sedimentation, and thermal aspects: Pacific Section, Society of Economic Paleontologists and Mineralogists, v. 40, p. 71-85.

Richardson, S. R., 1984, Stratigraphy and depositional environments of a marine-nonmarine Plio-Pleistocene sequence, western Salton Trough, California [M. S. thesis]: San Diego State University, 112 p.

Rightmer D.A., and Abbot, P.L., The Pliocene Fish Creek sturstrom, Anza Borrego Desert State Park, southern California *in* Sturzstroms and Detachment Faults, Anza Borrego State Park, California, South Coast Geological Society, Annual Field Trip Guidebook 24, p. 165-184.

Ross, Z.E. et al., 2019, Hierarchical interlocked orthogonal faulting in the 2019 Ridgecrest earthquake sequence: Science, v. 366, p. 346–351, doi:10.1126/science.aaz0109.

Shirvell, C.R., 2006, Pliocene Exhumation along the West Salton Detachment System and Tectonic Evolution of the Fish Creek-Vallecito Supradetachment Basin, Salton Trough, Southern California [Masters Thesis]: University of California, Los Angeles, 135 p.

Shirvell, C.R., Stockli, D.F., Axen, G.J., and Grove, M., 2009, Miocene-Pliocene exhumation along the west Salton detachment fault, southern California, from (U-Th)/He

thermochronometry of apatite and zircon: Tectonics, v. 28, p. 14, doi:10.1029/2007TC002172.

Smith, D. D., 1962, Geology of the northeast quarter of the Carrizo Mountain quadrangle, Imperial County, California [M. A. thesis]: University of Southern California, 89 p.

Stump, T. E., 1972, Stratigraphy and paleontology of the Formation in the western Colorado Imperial Desert [M. S. thesis]: San Diego, California State University, 132 P.

Tarbet, L. A., and Holman, W. H., 1944, Stratigraphy and micropaleontology of the west side of Imperial Valley (abstract): American Association of Petroleum Geologists Bulletin, v. 28, p. 1781-1782.

Tarbet, L. A., 1951, Imperial Valley: American Association of Petroleum Geologists Bulletin, v. 35, p. 260-263.

Todd, V. (2004). Preliminary Geological Map of the El Cajon 30’ x 60’ Quadrangle, Southern California. USGS Open File Report 2004-1361.

Todd, V. (1977). Geologic map of the Agua Caliente Springs quadrangle, San Diego County, California. USGS Open File Report 077-742.

U.S. Geological Survey, 20220815, USGS Lidar Point Cloud CA_Eastern_San_Diego_Co_Lidar_2016_B16: U.S. Geological Survey. Distributed by OpenTopography. Accessed: December 2019.

U.S. Geological Survey and California Geological Survey (2004). Quaternary fault and fold database for the United States, from USGS website available at

https://www.usgs.gov/naturalhazards/ earthquake-hazards/faults (last accessed February 2021).

Umhoefer, P.J., Darin, M.H., Bennett, S.E.K., Skinner, L.A., Dorsey, R.J., and Oskin, M.E., 2018, Breaching of strike-slip faults and successive flooding of pull-apart basins to form the Gulf of California seaway from ca. 8–6 Ma: Geology, v. 46, p. 695–698, doi:10.1130/G40242.1.

Ver Planck, W. E., 1952, Gypsum in California: California Division of Mines, Bulletin 163, 63 p.

van Wijk, J.W., Heyman, S.P., Axen, G.J., and Persaud, P., 2019, Nature of the crust in the northern Gulf of California and Salton Trough: Geosphere, v. 15, p. 1598–1616, doi:10.1130/GES02082.1.

Winker, C.D., 1987, Neogene stratigraphy of the Fish Creek-Vallecito section, Southern California: implications for early history of the northern Gulf of California and Colorado Delta [Ph.D.]: The University of Arizona, 528 p.

Winker, C.D., and Kidwell, S.M., 1986, Paleocurrent evidence for lateral displacement of the Pliocene Colorado River delta by the San Andreas fault system, southeastern California: Geology, v. 14, p. 788, doi:10.1130/0091-7613(1986)14<788:PEFLDO>2.0.CO;2.

Winker, C., D., and Kidwell, S., M., 1996, Stratigraphy of a Marine Rift Basin: Neogene of the Western Salton Trough, California, *in* Field Guide Conference 1996, Pacific Section A.A.P.G., Pacific Section SEPM GM73, v. Book 80, p. 295–336.

Woodard, G. D., 1963, The Cenozoic succession of the west Colorado Desert, San Diego and Imperial Counties, southern California [Ph. D. dissertation]: Berkeley, University of California, 173 p.

Woodard, G. D., 1974, Redefinition of Cenozoic stratigraphic column in Split Mountain Gorge, Imperial Valley, California: American Association of Petroleum Geologists Bulletin, v. 58, p. 521-539.

A1 - APPENDIX TO CHAPTER 1

The appendix to Chapter 1 includes two figures and one table listed and described below.

Figure A1.1 – Photograph of field relationships showing marine basin strata and proximal facies / breccias on the crystalline basement rocks with the approximate location of the proto-Vallecito fault indicated.

Figure A1.2 – Map of photograph locations

Table A1.1 – Table of photograph locations, elevations, and view azimuth

Figure A1.1. Photograph of the Vallecito range front (left) with basement rocks (K) at the peaks, sedimentary breccia, the Stone Wash member, and the Jackson Fork member are overlying the basement in the middle (breccias), interfingering with the Mud Hills member (marine basin strata) on the right. The proto-Vallecito fault (PVF) is interpreted and observed through the breccias. View azimuth is 030. Photo location is shown on Figure A1.2.

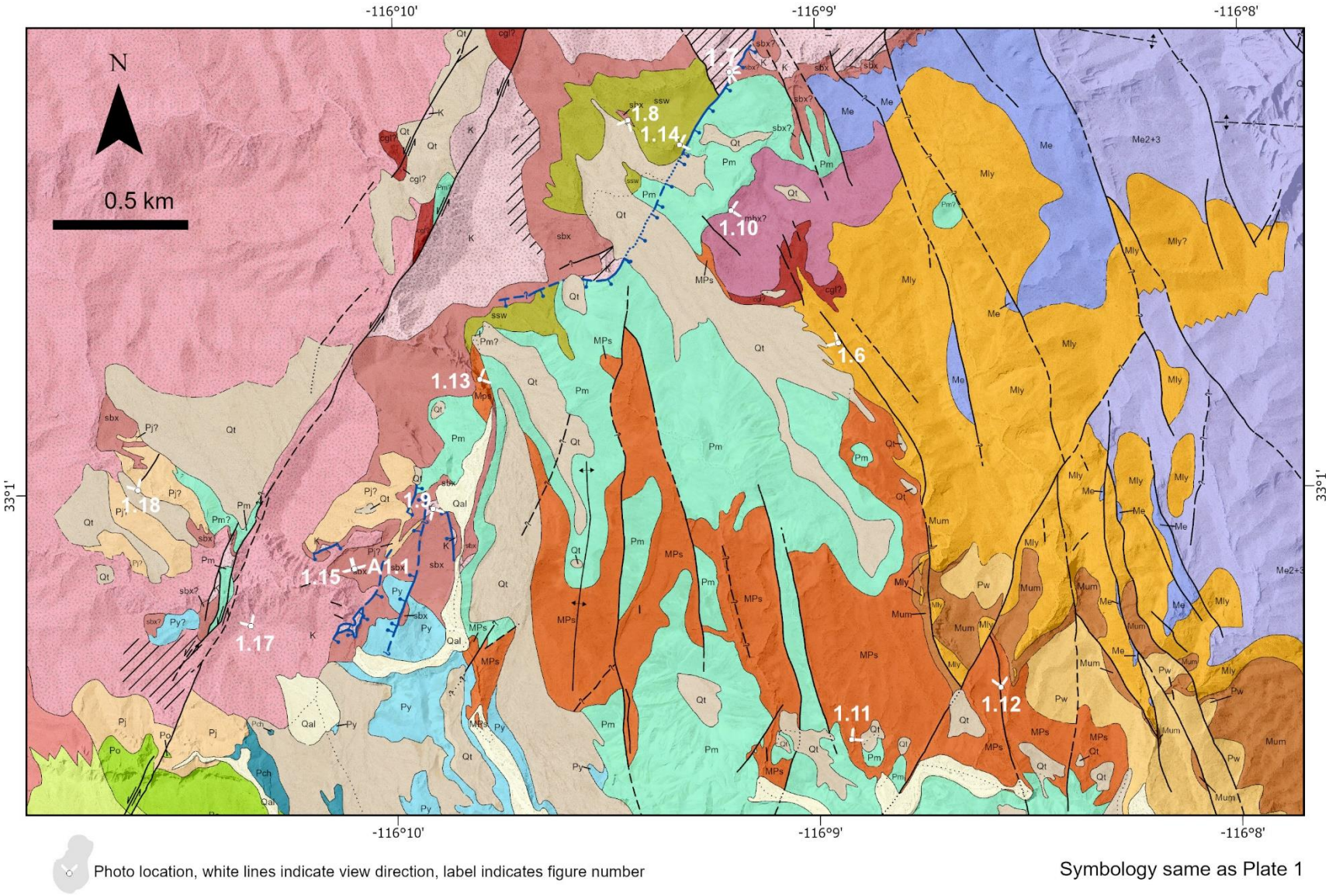

Figure A1.2. Map of photo locations used in Chapter 1

Table A1.1. Locations for photographs in Chapter 1

Figure	Latitude	Longitude	Elevation (m)	Vertical Error (m)	View bearing (°)
1.6	33.02154	-116.14915	365	5	300
1.7	33.03058	-116.15338	373	10	100
1.7	33.03058	-116.15338	373	10	135
1.8	33.02901	-116.15739	428	5	206
1.9	33.01614	-116.16521	350	-	150
1.10	33.025975	-116.153355	395	5	078
1.11	33.00835	-116.148756	233	5	051
1.12	33.01006	-116.142839	264	10	350
1.13	33.0204247	-116.1633173	469	20	065
1.14	33.02818	-116.15536	427	10	072
1.15	33.01414	-116.16834	441	10	300
1.17	33.01228	-116.17242	496	10	330
1.18	33.01683	-116.17685	486	10	330
A1.1	33.01415	-116.16832	440	10	030

CHAPTER 2

Apatite (U-Th)/He constraints on subsidence, uplift, and thermal conditions of the Fish Creek Vallecito Basin within the northern Gulf of California rift

ABSTRACT

The Salton Trough is a seismically active region in the northern Gulf of California rift. This late Cenozoic right-lateral transtensional system is characterized by low-angle normal faults and strike-slip faults, overprinted in part by transpressional strike-slip and reverse faults since the mid-Quaternary. The Fish Creek Vallecito basin (FCVB), a subbasin of the Salton trough, preserves a record of syn-rift deposition from 8-1 Ma, including the arrival of Colorado River detritus ca. 5.3 Ma. The FCVB contains a complete ~6 km thick sedimentary section. However, compaction of strata in the FCVB appears inconsistent with ~6 km burial, requiring an alternative structural and depositional model and/or anomalously high pore-pressure conditions. New mapping from Young 2023 (Chapter 1) suggests that the proto-Vallecito fault, an early breakaway of the West Salton detachment fault, partitioned FCVB subsidence into two subbasins, allowing for reduced burial of the lower FCVB section. This Chapter tests this scenario using low-temperature thermochronology, specifically apatite (U-Th)/He (AHe) data. These data show only partial or no resetting of AHe ages, as indicated by preservation of detrital age signatures and sparse AHe ages younger than the depositional ages. This implies that temperature at the base of the FCVB section may not have exceeded the AHe partial retention zone (<~55-80°C). To extract additional information from the AHe data, I use a combination of forward and inverse modeling to constrain post-depositional thermal histories while considering the effects of radiation damage and detrital inheritance. From the dates and

modeling, I determine that the maximum burial temperature of the FCVB was about 80-90°C, and the burial depth of the exhumed section was likely ≤4 km. The data supports a geothermal gradient of ~20°C/km, which is much lower than in the modern Salton Trough, suggesting that while the FCVB stratigraphy is analogous to the modern Salton Trough, the thermal conditions are different. Best-fit thermal histories from inverse modeling suggest uplift occurred since 4-1 Ma, which is consistent with uplift and tilting occurring during deposition of the upper section after 4 Ma, and onset of transpression at 1.2 Ma.

INTRODUCTION

The Gulf of California is one of the few localities actively transitioning from continental rupture to seafloor spreading and provides a rare insight into what early continental margins look like before they are deeply buried by passive margin depositional processes (Axen and Fletcher, 1998). The Salton Trough, which is the northern portion of the Gulf of California, is unique within this setting because rapid deposition by the Colorado River Delta initiated almost immediately after rifting began (Dorsey et al., 2011). As a result, the new crust formed here is transitional and composed of mostly sediment with some magmatic crust from rifting (Fuis et al., 1984; Dorsey et al., 2007; Han et al., 2016).

The Fish Creek-Vallecito basin (FCVB), a subbasin located on the western margin of the Salton Trough (Figure 2.1), exposes a key record of the formation of the Salton Trough and northern Gulf Extensional Provence, the integration of the lower Colorado River, and the birth of strike-slip faults through the Peninsular Ranges (Dorsey et al., 2011, 2012). This basin has

been tilted and exposes approximately 6 km of section in the hanging wall of the West Salton detachment fault. Recent work by Young 2023 (Chapter 1) suggests that subsidence and deposition of the FCVB was partitioned by an early breakaway of the West Salton detachment fault, the proto-Vallecito fault. The proto-Vallecito fault created the accommodation space for the deposition of the lower FCVB, shutting off around 4.4 Ma as slip-rate increased on the West Salton detachment fault. The proto-Vallecito fault was then buried along with the rest of the detachment hanging wall and subsequently exhumed with the transition to shortening after 1 Ma. The FCVB strata are analogous to those at depth along the Southern San Andreas fault system in the Salton Trough today, where many faults exhibit both creep and seismogenic surface rupture. The exhumed FCVB and proto-Vallecito fault may thus provide exposures of rocks and a fault zone, respectively, from seismogenic depths analogous to present conditions along the Southern San Andreas fault system.

The currently published structural model the Fish Creek Vallecito basin has all deposition and subsidence occurring in the hanging wall of the West Salton detachment fault (Model1, Figure 2.2, Dorsey et al., 2012), although many studies have noted the importance of subsidence adjacent to the Vallecito fault during deposition of the lower FCVB (e.g., Kerr 1982; Shirvell 2006; Shirvell et al., 2009; Alasad et al., 2023). In Chapter 1, I proposed an alternative structural model supported by updated geologic mapping (Model2, Figure 2.2). Here I test between these two models by constructing a cross-section through the basin and by applying apatite U-Th/He thermochronology (closure temperature of ~70°C). Model one predicts fully reset cooling ages in the lower 2 to 4 km of the FCVB section, which would have been buried to a depth of 4 km or greater. Model two predicts fully reset cooling ages only in the lowest 500 m

of section, if at all. Model two also predicts younging of cooling ages towards the proto-Vallecito fault in the foot wall basement rocks. To test between these two models, I obtained apatite (U-Th)/He cooling ages from samples along Fish Creek wash through the lower FCVB and from samples of crystalline basement rocks in the hanging wall and foot wall of the proto-Vallecito fault. I then use forward and inverse thermal modeling to estimate the timing of exhumation based on the samples and to further assess the thermal conditions and maximum burial temperatures of the lower FCVB.

BACKGROUND

Stratigraphy

The Vallecito Mountains, Fish Creek Mountains, and the FCVB basement are all Paleozoic to early Mesozoic meta-sedimentary and early Cretaceous meta-volcanic rocks intruded by the eastern Cretaceous Peninsular Ranges batholith, which I will refer to collectively as the basement. The lower plate rocks in the foot wall of the West Salton detachment fault and the Vallecito fault are mostly Late Cretaceous La Posta pluton (Todd, 1977). This mostly tonalite pluton intruded the Granite Mountain pluton and Paleozoic to Jurassic metasedimentary rocks that occur as relatively spatially limited outcrops of schist and gneiss. Overlying the basement rocks, strata of the FCVB are a 5.5-6 km thick succession of southwest-dipping late Miocene (~8 Ma) to Pleistocene (<0.8 Ma) (Dorsey et al., 2011, 2012) rocks divided into three Groups: the Split Mountain Group, the Imperial Group, and the Palm Spring Group (Plate 1). A brief overview of this stratigraphy is provided in this section. Readers

are directed to Young (2023, Chapter 1 *and references therein*) for an in-depth discussion of the FCVB stratigraphy. Overall, sediments in the FCVB have two sources. The first is the surrounding higher topography of the Peninsular Ranges (local or L-suite), and the second is the Colorado River (C-suite). L-suite sediments are plagioclase-rich and typically contain small pebbles and coarse sand of crystalline rocks, mostly tonalite, from the Peninsular Ranges batholith and associated metamorphic framework rocks, as well as fragments of volcanic rocks and reworked nonmarine sediments capping the range (Winker and Kidwell, 1996). Colorado River sediments first appeared in the FCVB at 5.3 Ma (Dorsey et al., 2007; 2011). Crow et al. (2021) propose a later arrival of Colorado River sediment at 4.80-4.63 Ma; however, this younger date requires stratigraphic duplication by faults cutting the FCVB that is not yet documented. Significant deposition of Colorado River-derived sediments into the FCVB continued until about ~2.8 Ma (Dorsey et al., 2011). Inter-fingering of Colorado River-derived and local sediments occurred during the early and late phases of Colorado River deposition in the FCVB (Winker and Kidwell, 1986; Dorsey et al., 2007, 2011). As Colorado River deposition progressed, the depositional setting transitioned from marine to fluvial deltaic with progradation of the Colorado River delta and tectonic translation past the river mouth, which is fixed to the North America plate at Yuma, Arizona (Winker and Kidwell, 1986; Dorsey et al., 2007, 2011). This transition in depositional setting accompanied a transitional return to locally sourced units. The FCVB strata are also characterized based on facies – proximal facies, which I interpret as foot wall scarp derived, and distal facies. Most distal facies are C-suite, and all proximal facies are L-suite, but L-suite units range from proximal to distal. Overall, facies and provenance are useful for describing and classifying the units mapped in the FCVB.

The Split Mountain Group (Miocene) at Fish Creek Wash is composed of nonmarine L-suite clastic sedimentary rocks and is divided into the Elephant Trees Formation and the lower megabreccia. The late Miocene Elephant Trees Formation is an alluvial fan conglomerate with sandstone derived from proximal alluvial fans plus distal alluvial fans and stream deposits. In the Split Mountain area, the Elephant Trees Formation is about 500 m thick, thinning to the east (Dorsey et al., 2011). The late Miocene lower megabreccia is a long runout nonmarine landslide-derived megabreccia sourced from the Vallecito Mountains deposited on top of the Elephant Trees Formation. The thickness of the lower megabreccia varies along strike but is ~50 m thick in Split Mountain Gorge.

The Imperial Group (late Miocene-early Pliocene) is composed of both L-suite and C-suite marine fossiliferous clastics, limestone, and evaporite. From oldest to youngest, it is divided into the Fish Creek Gypsum, the Latrania Formation, and the Deguynos Formation. The Fish Creek Gypsum is a thin layer of marine gypsum and anhydrite separating the lower megabreccia in the Split Mountain Group from the Latrania Formation in the Imperial Group. The late Miocene to early Pliocene Latrania Formation is a ~350 m thick exposure of L-suite marine clastics and has five members exposed in the FCVB: the Lycium Member, the upper megabreccia, the Wind Caves Member, and the Stone Wash Member (Winker and Kidwell, 1996). The Lycium Member is ~100 m thick and composed of L-suite marine turbidite-like sandstone with conglomerates. The upper megabreccia is a marine subaqueous landslide megabreccia sourced from the Fish Creek Mountains and is <50 m thick, and its thickness varies along strike. The Wind Caves Member is ~150 m thick and composed of interbedded C-suite and L-suite turbidite sandstones, with a greater proportion of L-suite derived sediments

towards the base of the member. This represents the oldest recognized input from the Colorado River into the FCVB. The early Pliocene Deguynos Formation is a ~1050 m-thick deltaic succession of C-suite marine clastics. The Deguynos Formation is traditionally divided into the Mud Hills Member, the Yuha Member, and the Camels Head Member, based on facies changes consistent with Colorado River delta progradation: The Mud Hills Member is the prodelta offshore marine facies, the Yuha Member is the marine delta platform, and the Camels Head Member is the marginal marine delta front. The Stone Wash Member is a time-transgressive unit consisting of conglomerate with L-suite sandstone that is laterally continuous with the Lycium Member, the Wind Caves Member, and the Mud Hills Member. Proximal facies of the Stone Wash Member are fossiliferous, while distal facies tend to be fossil-poor sediment gravity flows. The Jackson Fork Member is a marginal marine L-suite sandstone and conglomerate mapped by Winker (1987) as laterally continuous with the Camels Head Member and the base of the Palm Spring Group.

The Palm Spring Group (mid Pliocene-early Pleistocene) is composed of nonmarine clastics with the transition from C-suite to L-suite sediments occurring near the base of the group. It is divided into the Diablo Formation, the Olla Formation, the Tapiado Formation, the Hueso Formation, the Borrego Formation/Bow Willow Beds, and the Canebrake Conglomerate. Samples in this study come from the Diablo Formation (also referred to as the Arroyo-Diablo), which is ~1000 m thick C-suite fluvial sandstone, siltstone, and claystone deposited as part of the nonmarine Colorado River deltaic succession. The rest of the Palm Spring Group is not sampled or discussed in this study but is described in Young (2023, Chapter 1, and *references therein*).

Young (2023, Chapter 1) defined new units along the Vallecito fault toward the base of the FCVB section. These units are a zone of tectonically brecciated crystalline basement, sedimentary breccia (sbx), a megabreccia (mbx), and a unit of interbedded silt and conglomerate, named the silty Stone Wash Member (ssw). See Plate 1 for location and extent. I also expanded the definitions for the Stone Wash and Jackson Fork Members. All of these units are time-transgressive, locally sourced, range-front mantling and foot wall scarp-derived deposits that generally strike parallel to the range front, broadly defining the northeast boundary of the basin and dip to the southeast. They interfinger with the canonical stratigraphy defined along the basin axis. Collectively, these units are considered analogous to the Canebrake Conglomerate in the upper FCVB.

Prior thermochronometric studies

Low-temperature thermochronology datasets from prior studies in the region provide excellent context for the data and interpretations presented here and were essential in selecting an appropriate analytical approach to test between Models 1 and 2. One study from Fish Creek Wash focused on the provenance of the FCVB strata with respect to Colorado Plateau source areas and used detrital zircon (U-Th)/He (ZHe) cooling ages and U-Pb crystallization ages (Cloos, 2014). All of the ZHe cooling ages from that study are older than the paleomagnetic and micro-fossil depositional ages of the FCVB strata. This suggests that the sampled units were buried to temperatures less than ~170° C, which is the closure temperature for the zircon (U-Th)/He system. Apatite (U-Th)/He has a closure temperature of ~70° C and is an excellent choice for assessing relatively shallow tectonic events, such as those expected for the FCVB. Assuming a geothermal gradient of 20 -50° C/km, reset appetite helium cooling ages

(cooling ages younger than the depositional age) can be expected at depths below 1.4-3.5 km, which are the depths required to test the structural models for the FCVB.

Prior work by Shirvell (2006) and Shirvell et al. (2009) used AHe to assess the timing of West Salton Detachment fault (WSDF) activity (locations of these samples are in Figure 2.3). Their sample transect from Whale Peak, located in the foot wall of the WSDF adjacent to the FCVB, provides important context for the timing of PVF and WSDF activity. This dataset generally shows evidence for slow WSDF activity (exhumation rate of ~100 m/Myr) from ~8 Ma, with acceleration after 5 Ma required to exhume these reset rocks to the surface (Figure 2.4). The authors of that study favor a model in which the Vallecito fault was an early structure responsible for lower FCVB subsidence and deposition from 8-5 Ma. This occurred either prior to the onset of WSDF slip, simultaneously with WSDF slip as an upper-plate fault, or as an early WSDF breakaway that was later transferred to the upper plate (similar to Model 2, Figure 2.2). Their work infers subsidence adjacent to the modern trace of the VF and does not reconcile how the VF and WSDF would interact at depth or how the VF would affect the burial depth and, thus, the exhumation magnitude of the lower FCVB. Their data, while consistent with Model 2, do not eliminate other possible models, such as WSDF being fully responsible for FCVB deposition since 8 Ma (Model 1, Figure 2.2).

Overview of Apatite (U-Th)/He Dating

Thermochronology ages indicate when a mineral crystal cools through an effective closure temperature, such that the daughter product of radioactive decay is retained. Thermochronology thus provides a cooling age rather than a crystallization age. Above the

effective closure temperature, the daughter product diffuses out of the crystal, and the cooling age is zero or nonexistent (open system). Below the effective closure temperature, almost all the daughter product is retained, resulting in an age that records the time since reaching this temperature (closed system). Just below the effective closure temperature is a temperature range known as the partial retention zone, where the diffusivity of the daughter product is still high enough that it is only partially retained in the crystal (Reiners and Brandon, 2006). For detrital crystals that enter the partial retention zone during burial, some of the existing ^{4}He is retained, and some is lost. If that crystal is never buried to temperatures above the closure temperature, then it is considered partially reset. For samples that are heated above the closure temperature during burial, time spent in the partial retention zone will change ^{4}He diffusion based on hold time and cooling rate. Because there is a relatively consistent relationship between temperature and depth within the earth, cooling ages are used in conjunction with a geothermal gradient to estimate the time since a sample was at a particular depth. Exhumation rates can be estimated when samples are collected in a vertical transect or if multiple thermochronometers that sample different temperatures and, therefore, different depths can be applied to the same sample.

The U-Th/He method uses the accumulation of ^{4}He derived from alpha decay of ^{238}U, ^{235}U, ^{232}Th, and ^{147}Sm to determine a cooling age. Important for this study, we avoid using a fixed effective closure temperature because this is an oversimplification of the change in ^{4}He diffusivity with temperature. In reality, effective closure temperature depends on several factors: cooling rate, hold time, crystal size, and crystal damage. The effective closure temperature generally increases with cooling rate (Reiners and Brandon, 2006). Similarly, the

amount of time the crystal spends at a temperature, also called the hold time, changes the amount of heating required to lose the daughter product, ^{4}He, through diffusion. In the apatite helium system, the partial retention zone occurs at 30-65°C for 1 Ma hold times but occurs at 0-23°C for 1 Ga hold times. This means that very rapid burial and exhumation requires hotter temperatures to see complete resetting of grains, while very slow events require lower temperatures. For this study, which occurs over <8 Myr, placing the temperature of the PRZ at about 20-65°C is a reasonable assumption.

The size of the crystal determines the amount of daughter product lost due to ejection of alpha particles during decay. Alpha ejection causes the alpha particle to travel 30 µm and is predictable enough that a correction can be applied to the data that usually accounts for its effect on the date. However, this correction is best applied to crystals greater than or equal to 60 µm, and there is more potential for error when applied to crystals smaller than 60 µm. The minimum datable crystal width is 40 µm. Fracturing of the crystal also increases the effects of alpha ejection, making this correction insufficient or inaccurate if the crystal is highly fractured or broken. Broken crystals also under sample the diffusive profile of ^{4}He within a crystal. Radiation damage, which disrupts the crystal lattice, will change the ^{4}He diffusivity at specific temperatures in different crystals, making each crystal sensitive to slightly different temperatures (e.g. Fox et al., 2019 *and references therein)*. As a result, dates from different crystals in the same sample will record different cooling ages. This process also can form ^{4}He traps within the crystal, which can make crystals appear older. The effective U content (eU) and pre-depositional cooling history both play an important role in determining the amount of radiation damage present (e.g., Guenthner et al., 2015; Fox et al., 2019). In these cases,

modeling of the ages using radiation damage-specific calibrations may be required to accurately assess the thermal history.

Detrital vs. Bedrock Thermochronology

To further test the structural model proposed in Young (2023, Chapter 1) and to assess whether the Fish Creek Vallecito basin exposes rocks and fault zones from seismogenic depths, I expand the structural analysis from Chapter 1 using low-temperature thermochronology. I use a combination of bedrock (crystalline basement) and detrital (basin strata) thermochronology. The bedrock samples from basement rocks provide a point of comparison between the local source material and the material preserved in basin strata. Cooling ages from the foot wall basement rocks test for exhumation of the foot wall and demarcate the distribution of cooling ages to be expected in the local basin source material prior to any thermal reheating effects. Cooling ages from the basement rocks in the hanging wall test exhumation of the bottom of the FCVB section and show how the same material as the foot wall responded to the tectonic events experienced by the hanging wall. The detrital samples test for both burial depth and timing of exhumation of the FCVB section using the closure temperature and an assumed geothermal gradient and the cooling ages respectively.

In bedrock thermochronology, younger ages generally occur at lower structural depths or at locations of rapid exhumation, since as the rock moves up through the crust and the closure temperature, the first rocks to cool will be the ones on top, and the younger ones that cool later will be on the bottom. In detrital thermochronology, where the sampled material has been eroded and transported, we expect the opposite. The grains with older cooling ages are

the first to be eroded from the mountains and deposited in the basin. As basin deposition continues, grains with progressively younger cooling ages are eroded and deposited. This means that the grains will have a crystallization age that is very old, a cooling age that is younger than that, and a depositional age that is still younger. This trend continues until the grains are buried to the depth of the partial retention zone. Once at or below the partial retention zone, grains begin the process of resetting (Figure 2.5). During exhumation following this burial, these grains will once again pass through and above the closure temperature, locking in a new cooling age. This new cooling age is now younger than the depositional age, and one can again expect that the older reset ages will be higher in the section than the younger reset ages. This means that in an exhumed sedimentary section with reset ages in the lower part of the section, I expect to see from top to bottom: cooling ages older than the depositional age (not reset) that get older with depth, and then cooling ages younger than the depositional age (reset) that get younger with depth. Partial resetting is also possible. Partial resetting occurs when grains are buried within the partial retention zone, when grains spend a brief time at resetting temperatures, or when grains spend a very long time at cooler temperatures (see explanation of hold time above). Because each individual grain begins with its own budget of ^{4}He and diffusion characteristics, a partially reset detrital sample will exhibit a spread of cooling ages, with some grains being older and others younger than the depositional age (Figure 2.5).

METHODS

Apatite (U-Th)/He

I analyzed 14 detrital samples and one basement sample from the Vallecito fault hanging wall and eight samples from the proto-Vallecito fault foot wall (Figures 2.3 and 2.6; Table 2.1; Plate 1). Samples were selected based on stratigraphic location and position relative to the Vallecito fault. Eleven of the 14 detrital samples were originally collected by Cloos (2014) for detrital zircon analysis using U-Pb and (U-Th)/He double dating. Existing apatite separates from these samples were used in my study. Additional samples were collected to fill gaps and supplement the Cloos (2014) samples. Because this region has extreme summer temperatures that can heat rocks at the surface to temperatures equivalent to those in a partial retention zone, care was taken to sample north-facing and fresh outcrop whenever possible. If the Fish Creek Vallecito basin were deposited as a continuous section in the hanging wall of the WSDF, without partitioning as predicted in previous structural models, and assuming a geothermal gradient between 20 to 50°C per kilometer, we would expect to see fully reset appetite (U-Th)/He cooling ages below about 1.5- 3.5 km depth in the section (Figure 2.2). The analyzed samples are thus from the lower half of the Fish Creek Vallecito basin where this resetting signal should be present. Mineral separations and sample analysis were conducted at the UTChron (U-Th)/He laboratory at the Jackson School of Geosciences at the University of Texas at Austin following the analytical procedures of the lab (https://www.jsg.utexas.edu/utchron-lab/u-th-he-lab/). An average of 4-7 grains were analyzed for each sample, with more grains analyzed for samples with small or broken crystals. I measured the length and width of each crystal to estimate a spherical radius and applied an alpha ejection correction accordingly. To

capture a more complete thermal history for the FCVB, we used the HeFTy software (Ketcham, 2005) to create forward and inverse models of select samples.

Cross-section construction

To provide context to the U-Th/He results, I constructed a geologic cross-section (Plate 2) of the FCVB through proximal foot wall-derived strata at line A-A' (Figure 2.1 and Plate 1). The position of the cross-section was selected to best show the relationship between strata in the hanging wall of the PVF and the hanging wall of the WSDF. Some stratigraphic relationships are simplified and are represented by a single unit. For example, the Hueso Formation contains two sub-units of coarse transitional units, and the Olla Formation also contains a coarse transitional subunit. The crystalline basement is lithologically undifferentiated in the cross-section and is colored based on tectonic position relative to the WSDF and PVF. Similarly, faults with small amounts of separation are excluded to improve the legibility of the large-scale structure of the FCVB. The cross-section was drafted at a smaller scale than the map, at about 1:48,000.

RESULTS

Of the samples collected for this study, one sample, Y21-041, did not yield datable material, and the rest were analyzed. Samples collected from the crystalline basement rocks and from single tonalite clasts in the megabreccias were relatively poor in apatite. The apatites of sufficient size for analysis in these samples were often broken, and the crystals that were pristine were close to or below the minimum dateable size of 40 μm. Apatite grains in the

detrital samples collected by Cloos (2014) were above 60 µm. Detailed analytical results and raw data are available in Appendix 2.

Hanging Wall Dates

Dates from the hanging wall are presented in stratigraphic order using stratigraphic position rather than depth (Figure 2.7; Table 2.2) since it is likely that the two are not equivalent given the updated structural model from Young (2023; Chapter 1). In Figure 2.7, the date from each grain in a sample is plotted with error bars showing the analytical error. The spread in dates within each sample is reduced with depth, indicating reheating of the samples. Based on the relationship between the cooling ages and depositional ages, none of the hanging wall samples are fully reset, indicating that the lower section was in the partial retention zone. Even the basement sample Y21-044 retains grains with dates over 10 Ma. The sample below ~4200 m (sample 13MCSMG21) shows partial resetting, and samples above 4200 m have no reset grains (Figure 2.7). This suggests that the lower FCVB section remained at or below ~60° C during subsidence and burial.

Foot Wall Dates

Dates from the foot wall are presented based on sample proximity to the trace of the proto-Vallecito fault (Figure 2.8; Table 2.3). Sample 27-141-1 from Shirvell (2006; Shivell et al., 2009) is plotted with the new dates from this study. As with the hanging wall samples, the data for each grain in the sample is plotted with bars showing the analytical error. The ages in the foot wall generally cluster tighter and younger with proximity to the PVF. Sample Y21-035 is older than the samples on either side of it. This sample was collected very close to a fault strand

interpreted as part of the proto-Vallecito fault (Plate 1) and may be from a downdropped, cooler sliver of rock within the fault zone. None of the foot wall samples have grains younger than 7 Ma, indicating minimal erosion and exhumation of the foot wall.

Cross-section

Active strike-slip faults cut the cross-section adjacent to earlier formed normal faults. These strike-slip faults are drawn as simple near-vertical faults, although both the Elsinore and Vallecito faults have more complex traces at the surface. The basin strata are partitioned across the hanging walls of the proto-Vallecito fault and the West Salton detachment fault. Deposition of Split Mountain Group, the Fish Creek Gypsum, and the Latrania Formation occurred completely within the hanging wall of the proto-Vallecito fault. These units interfinger with breccia facies shed from the foot wall of the Vallecito fault. The proto-Vallecito fault intersects antithetic normal faults in the line of section; the main trace responsible for basin subsidence does not fully reach the surface. Marking the end of its slip history, the proto-Vallecito fault is buried by the sedimentary breccia and by the Jackson Fork Member of the Deguynos Formation. Near the antithetic faults, the hanging wall is folded, likely due to downwarping of the hanging wall during proto-Vallecito fault slip. The Deguynos formation (Mud Hills, Yuha, and Camels head members) is not found extensively east of Split Mountain in this map area. Therefore, in cross-section the Deguynos formation pinches out around the Split Mountain anticline and Split Mountain fault. This pinch-out is reasonable and consistent with basin filling due to delta progradation and down dropping as the lower FCVB and adjacent foot wall rocks began subsiding in the hanging wall of the West Salton detachment fault.

The base of the section in the hanging wall of the West Salton detachment fault is occupied by the canebrake conglomerate, a coarse, locally sourced time transgressive unit that occurs everywhere above the crystalline basement rocks and depositionally inter-fingers with the basin strata. The Deguynos, Olla, and Hueso formations are shown thickening with depth towards the West Salton detachment fault, reflecting deposition in an evolving supradetachment basin. The hanging wall of the WSDF is folded into a set of anticline-syncline pairs near Sand Canyon and Whale Peak that are not associated with a fault at depth. A fanning-dip section is present within the upper Hueso formation that records tilting of the FCVB after ~1 Ma. I model this narrow zone of fanning dips as formed during slip above a curviplanar reverse-fault bend. This model reflects the hypothesis shown in Model 2, where approximately half of the tilting of the FCVB strata occurred during extension and rotation in the hanging wall of the West Salton Detachment fault, rather than as a result of later shortening. This allows for less burial of the lower FCVB than inferred from Model 1. In the cross-section, the base of the Split Mountain Group was likely exhumed from a depth of ~3 km, even though this lies at approximately 5.5 km stratigraphic depth.

DISCUSSION

Cooling ages from the hanging wall of the proto-Vallecito fault are partially reset in the lower part of the transect and not reset in the upper part of the sample transect. This suggests lower amounts of burial in the lower FCVB than originally hypothesized by previous work (e.g., Dorsey et al., 2012). However, the maximum temperature implied by these samples is still

surprisingly low for samples buried to about 3 km, as indicated by the cross-section (Plate 2, Model 2 in Figure 2.2). In the foot wall, cooling ages are all older than the base of the FCVB and are interpreted as coming from the partial retention zone. These ages generally become younger and cluster closer together towards the proto-Vallecito fault, which is indicative of modest foot wall uplift and exhumation. The results from both the hanging wall and the foot wall apatite helium cooling ages support the structural model of partitioned basin subsidence and, thus, reduced exhumation presented in Young (2023: Chapter 1). Because none of the hanging wall samples are fully reset, they cannot have been buried as deeply as Model 1 predicts (Figure 2.2. Even with a relatively low geothermal gradient of 15°C/km, full resetting would still be expected below 4 km. A depressed geothermal gradient is reasonable for this area due to the rapid sedimentation from the Colorado River Delta, keeping the section cooler than expected (e.g., Allen and Allen, 2013; Kolawole and Evenick, 2023). However, it is still unlikely that the bottom of the section would have stayed below 60°C in either model.

Deposition of the FCVB began at 8 Ma, and burial of the lower FCVB to resetting temperatures likely occurred after ~4 Ma (Figure 2.2). This means the hold time was <4 Ma for most of the lower FCVB. This short hold time combined with relatively shallow burial likely contributes to the lack of fully reset samples in the FCVB. Still, it does not explain the surprisingly low maximum temperature implied by the dates. To better understand these results, I use forward and inverse thermal models to 1) assess the effects of radiation damage on the observed ages, 2) determine a more complete thermal history for the samples, and 3) evaluate how the distribution of ages in the local sediment source may be inherited in the detrital dates. These models focus on the lower and locally sourced part of the section,

particularly the samples from the megabreccias that were obtained from single clasts (Figure 2.9, samples Y21-048 and Y21-047). Because a single clast was sampled, all analyzed grains experienced the same detrital history and sampled the same part of the source rocks. This contrasts with a sandstone sample, where each apatite grain will have its own detrital history and will sample a different point in the source landscape. Sampling a single clast thus removes detrital history and source variation as potential contributions to the distribution of dates observed.

Of the megabreccia samples, Y21-048 has the clearest positive relationship between the date and the effective uranium concentration (eU), making it the best candidate for thermal modeling with radiation damage. For sample Y21-048, an average of two grains was input into the model to produce a more linear date-eU trend (Figure 2.10). These values with a 20% error were used to create an inverse model and obtain possible time-temperature paths (histories) for the sample. This model applies the RDAAM correction by Flowers (2009) to account for radiation damage to the crystals. In the model set up (Figure 2.11), the first parameter for the history is a 30 Myr hold at 200-180° C to allow for the accumulation of radiation damage. The second parameter is for time at the surface based on the depositional age of the sample. The third and final parameter is relatively unconstrained and allows for paths between the maximum depositional age and present-day and between 120°C and the surface (~20 to 40° C), which allows the model to freely explore a wide variety of burial and exhumation histories. The model finds several good and acceptable paths through these parameters (Figure 2.11). Most notably, the peak temperature predicted by the good paths is 80-90°C, and the timing of exhumation is between ~4-1 Ma. Importantly, this result suggests that a short hold time

increased the effective closure temperature slightly, allowing partial retention of He up to these temperatures. These results are more consistent with the maximum temperatures expected for burial to ~4 km and suggest that radiation damage and a short hold time are a reasonable explanation for the partially reset Ahe dates in the lower FCVB. To further test the validity of this model, we take the good paths from the inverse model and run them in a forward model predicting the date-eU relationship. The date-eU forward model is a good match to the date-eU relationships observed in the data (Figure 2.12).

For samples Y21-037 and Y21-047, the date-eU relationship is more scattered and flatter, making these samples less suitable for thermal modeling on their own. The same inverse model set up as sample Y21-048 did not produce any acceptable paths when applied to these samples individually. However, when the date-eU values for all three megabreccia samples are plotted, they produce a positive date-eU trend covering a larger and younger time span than sample Y21-048 alone (Figure 2.13). By averaging the values for these three samples, they can be entered into the model together and produce good time-temperature paths (Figure 2.13). When those paths are put into date-eU forward models, they produce results similar to the measured values. I note that such a combination of samples may be invalid because each clast comes from a different part of the source area. Nonetheless, this does suggest that radiation damaged apatites in the lower FCVB experienced insufficient hold time to fully reset, explaining the anomalously low maximum temperatures implied by the data in the absence of thermal modeling.

While the inverse models above provide context for the partially reset nature of the lower section, the spread in the measured dates at each stratigraphic level is not fully explained

by radiation damage alone. To explore this problem further, I test whether a distribution of cooling ages in the local sediment source would affect the spread of detrital dates. Using a good time-temperature pathway and the spread of ages in my basement samples (Figure 2.14), I estimate maximum and minimum potential inherited date-eU curves. The dates from the basement source area provide a wide range of dates to be expected in the detrital samples. If these detrital samples are partially reset, I should expect this range to shrink as helium is lost from the samples in proportion to the initial concentration and radiation damage present in each crystal. I find that the detrital samples from the Elephant Trees Formation (Samples 12MCSMG03 and 12MCSMG01) plot within the maximum and minimum model curves (Figure 2.14). This suggests that inherited cooling ages from the basement source rocks do influence the range of partially reset dates observed in the lower FCVB detrital samples.

Structural Context

The reduced burial depth of the lower FCVB from my updated structural model combined with the cooling ages allows me to estimate a geothermal gradient for the FCVB during the last ~8 Myr. The Lower FCVB was likely buried to ~4 km depth. The AHe ages from the lowest part of the section are partially reset and indicate maximum temperatures of 60 – 90°C based on the data alone and thermal modeling respectively. This suggests a geothermal gradient of 20-30 deg C / km, which is lower than the modern Salton Trough. Presently the Salton Trough exhibits a geothermal gradient as high as ~40°C/km, linked to magmatic underplating, placing the 60°C isotherm at <1.5 km depth and the 80°C isotherm at 2 km depth (Lachenbruch et al., 1985). The data presented here for the FCVB require a significantly lower heat flow at ~8-4 Ma, which may be due to spatial variations (off rift axis) and/or very rapid

deposition in the FCVB, depressing the geothermal gradient and keeping the section cool. Overall, these new AHe data demonstrate that the FCVB was structurally segmented, subsided <6 km where exposed along Fish Creek Wash, and was characterized by a depressed syn-extensional geothermal gradient.

Implications for the Tectonic History of the FCVB and WSDF

Ahe cooling ages from the WSDF foot wall support the structural model presented here (Model 2) and lend insight into the relative timing of the WSDF and PVF activity. Whale Peak, in the foot wall of the WSDF, shows WSDF activity since ~8.2 Ma (Shirvell, 2006). Because these dates are all younger than the spread of dates observed in the hanging wall bedrock and they are tightly grouped within each sample, we can assume they are all fully reset. The two samples closest to the WSDF at Whale Peak are also the youngest samples, with cooling ages <5 Ma (Figure 2.4). The rest of the Whale Peak samples are relatively tightly grouped around ~8-5 Ma over a ~600 m span of elevation, suggesting steady and modest exhumation of 200 m/Myr during this time. Shirvell et al. (2009) consider sample 110-4 an anomaly due to crystal zonation. Ignoring that sample, they interpret acceleration of WSDF activity at 5-6 Ma based on the inflection in the age-elevation plot. Alternatively, I interpret rapid exhumation on the WSDF beginning at ~4-5 Ma. The youngest and lowest elevation samples were at temperatures of ~65-70 degrees at 4-3 Ma. Assuming a geothermal gradient of ~25°C/km, these samples were exhumed ~3-4 km to their current elevation in that time, requiring an increase in exhumation rate from 200 m/Myr to ~1000 m/Myr. This is consistent with the cessation of PVF activity around ~4.5 Ma observed by Young (2023; Chapter 1) and the acceleration of subsidence in the hanging wall of the WSDF. Other areas, like Pinyon Ridge, may have seen an increase in

exhumation of the WSDF foot wall slightly earlier than the Whale peak area, based on the subtle inflection in that dataset (Figure 2.4). However, based on the observations presented here, the AHe dates that would clearly show a rapid increase in WSDF activity are not yet fully exhumed in the foot wall. The stratigraphic evidence supporting this timing of early WSDF activity from 8 to 5 Ma is subtle and likely confined to the lower Canebrake Conglomerate; other pre-5 Ma units may lie hidden at depth.

CONCLUSIONS

Apatite (U-Th)/He cooling ages support that deposition of the FCVB was partitioned across the proto-Vallecito fault and the West Salton Detachment fault, with ages at the bottom of the FCVB section only partially reset. Thermal modeling suggests radiation damage and inheritance both affect the spread of dates from the detrital samples. The maximum burial temperatures were about 80-90°C, according to the good thermal histories from the inverse models. This implies reduced amounts of burial and exhumation compared to previous structural models and may suggest rapid sedimentation depressed the geothermal gradient. The cessation of proto-Vallecito fault activity around 4.5 Ma predicted from stratigraphic relationships (Chapter 1) is consistent with the timing of acceleration on the WSDF system based on existing AHe dates. Cross-section analysis of the FCVB suggests less than 3-4 km of exhumation for the lower FCVB. Combined with the maximum temperatures from thermal modeling, this implies a geothermal gradient of about 20-30°C / km, which is lower than the

modern Salton Trough and indicative of a lack of magmatic underplating in this marginal rift setting.

FIGURES

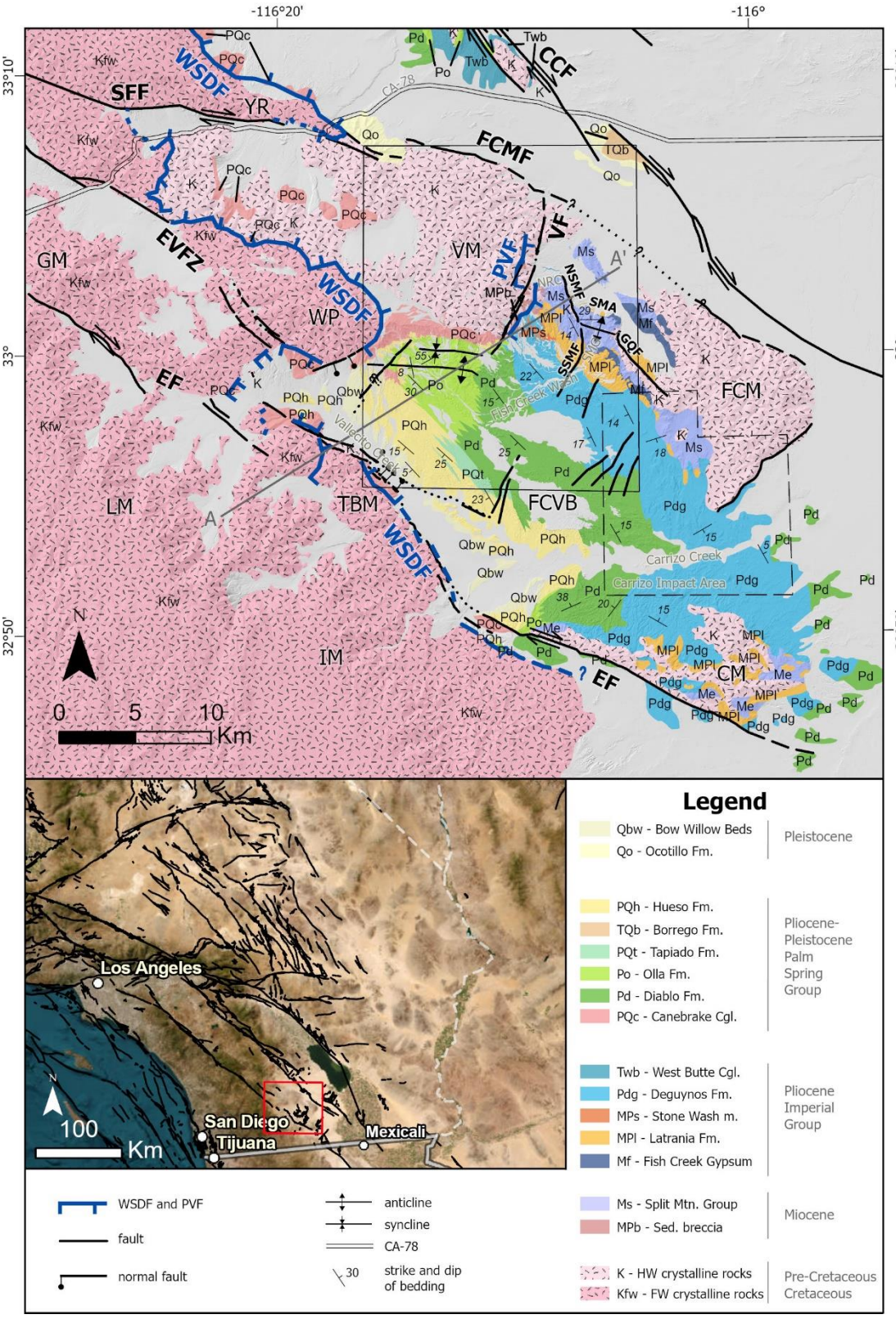

Figure 2.1. Caption on next page.

Caption to Figure 2.1: Geologic map of the FCVB and surrounding region with the extent of Figure 2.6 indicated by the solid rectangle. Cross-section line A-A' is shown here, and on Plate 1, the geologic cross-section is on Plate 2. Alluvium is not mapped. Units MPb and PQc are time transgressive spanning the Miocene-Pliocene and the Pliocene-Pleistocene respectively; they are placed in the legend at the time of their first occurrence. Lower map shows the location of the regional map and the FCVB within southern California. Compiled from Young (2023, Chapter 1), Janecke et al., 2010, and Dorsey et al., 2011.

CCF = Coyote Creek fault strand of the San Jacinto fault zone, CM = Coyote Mountains, EF = Elsinore fault, EVFZ = Earthquake Valley fault zone of the Elsinore fault system, FCM = Fish Creek Mountains, FCMF = Fish Creek Mountain fault, FCWF = Fish Creek Wash fault, GM = Granite Mountain, IM = Inkopa Mountains, LM = Laguna Mountains, NRC = No Return Canyon, NSMF = Northern Split Mountain fault, PVF = proto-Vallecito fault, SFF = San Felipe fault, SMA = Split Mountain anticline, SMG = Split Mountain Gorge, SSMF = Southern Split Mountain fault, TBM = Tierra Blanca Mountains, VF = Vallecito fault, WP = Whale Peak, WSDF = West Salton Detachment fault, VM = Vallecito Mountains, YR = Yaqui Ridge.

Hillshade in regional geologic map from USGS 3DEP, imagery in lower map from ESRI World Imagery (ESRI, 2022).

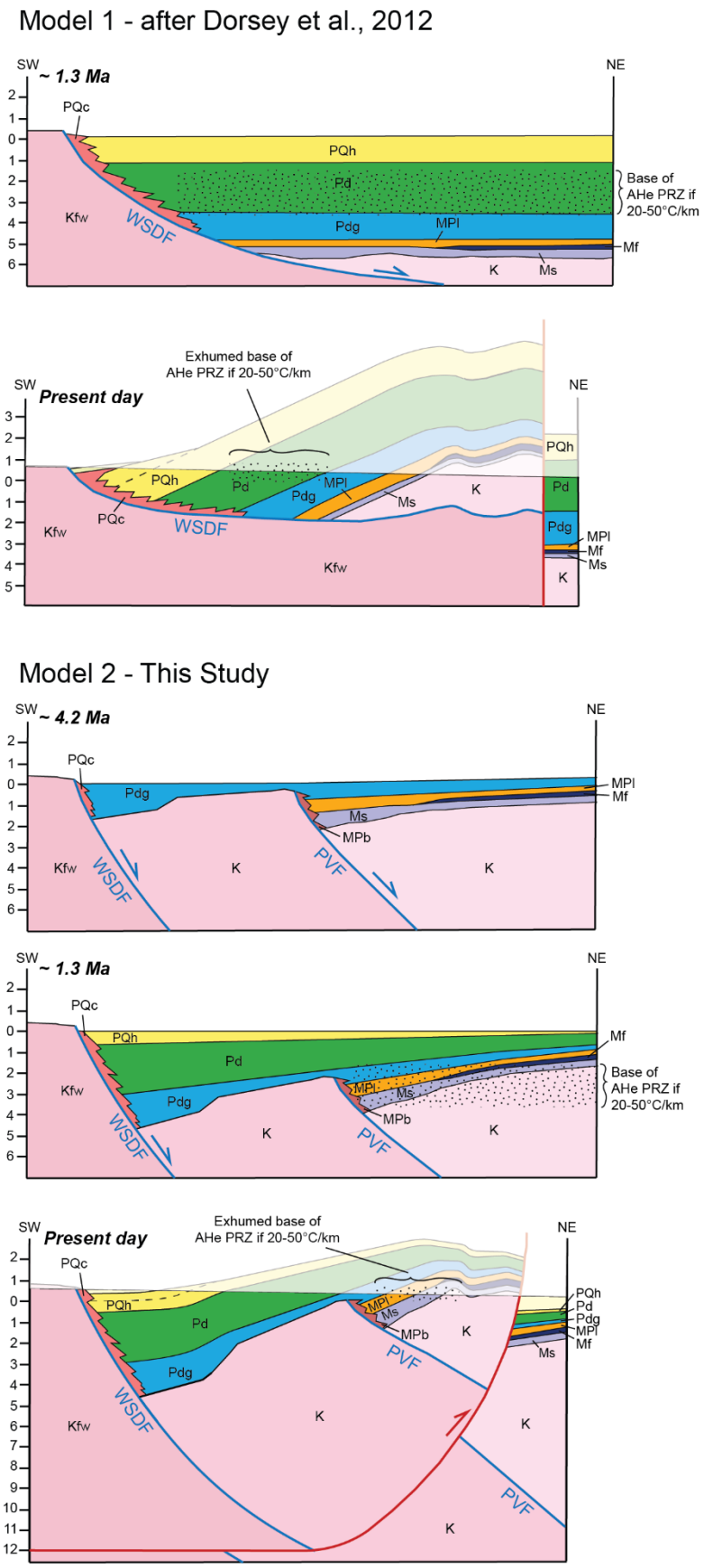

Figure 2.2. Cartoon cross-section of the FCVB approximately parallel to Fish Creek Wash. Upper: Model 1 for FCVB after Dorsey et al. (2012) where subsidence occurs only over the WSDF. Lower, Model 2 after Young, 2023 (Chapter 1) shows partitioned subsidence of the FCVB between the PVF and WSDF. Stippling shows the range of depths for the base (high end of the temperature range ~65°C) of the apatite (U-Th)/He partial retention zone prior to exhumation at ~1.3 Ma and shows the exhumed position of that PRZ at the surface in the present day. Samples collected from stratigraphically below the PRZ are expected to be completely reset, samples collected from within the PRZ are expected to be partially reset, and samples above the PRZ would not be reset. Unit abbreviations as in Figure 2.1. PRZ = partial retention zone, PVF = proto-Vallecito fault, WSDF = West Salton detachment fault.

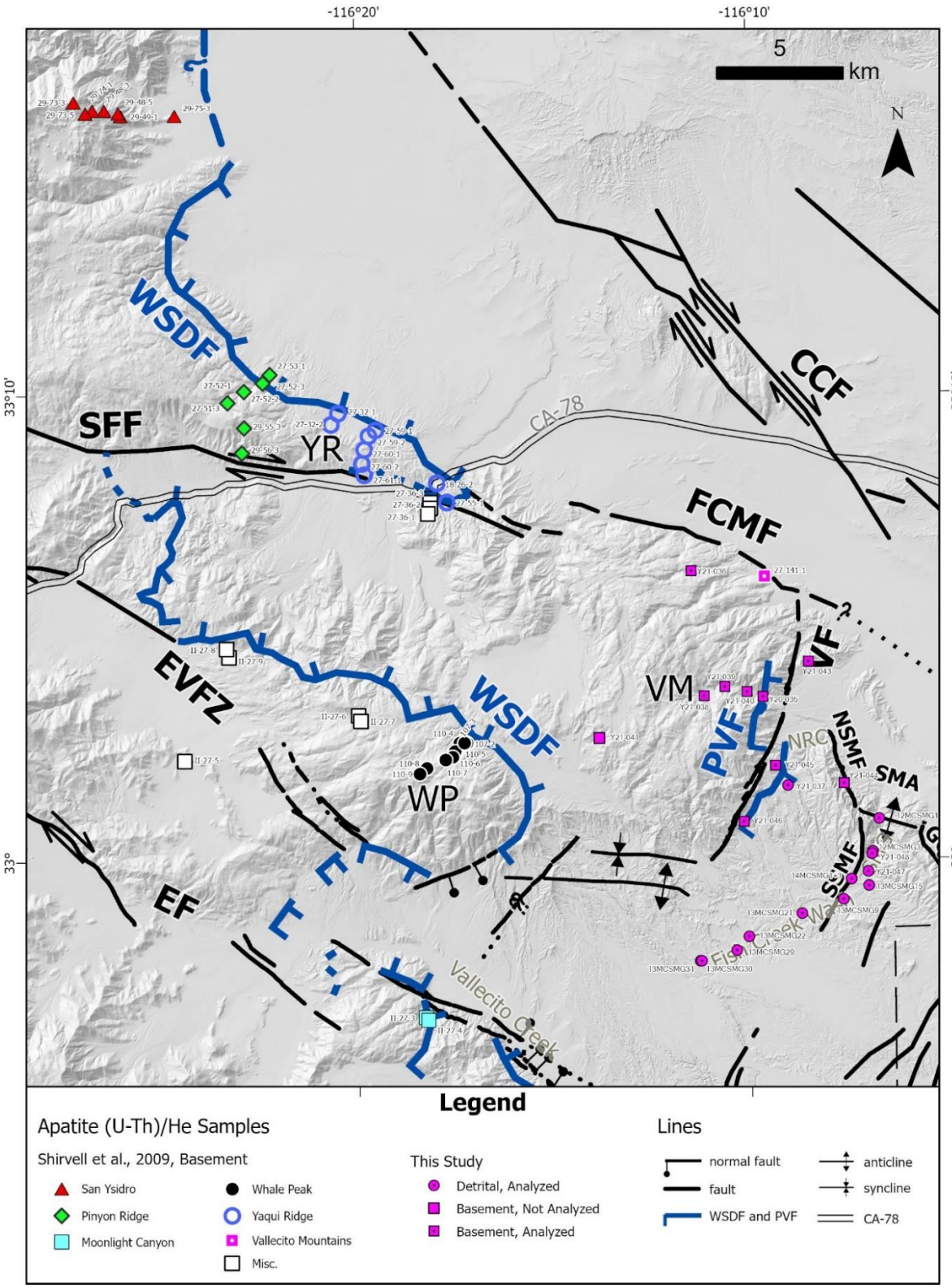

Figure 2.3: Map with locations of analyzed apatite (U-Th)/He samples from Shirvell (2006), Shirvell et al. (2009), and this study. Sample Y21-041 did not produce dateable material. Hillshade from USGS 3DEP.

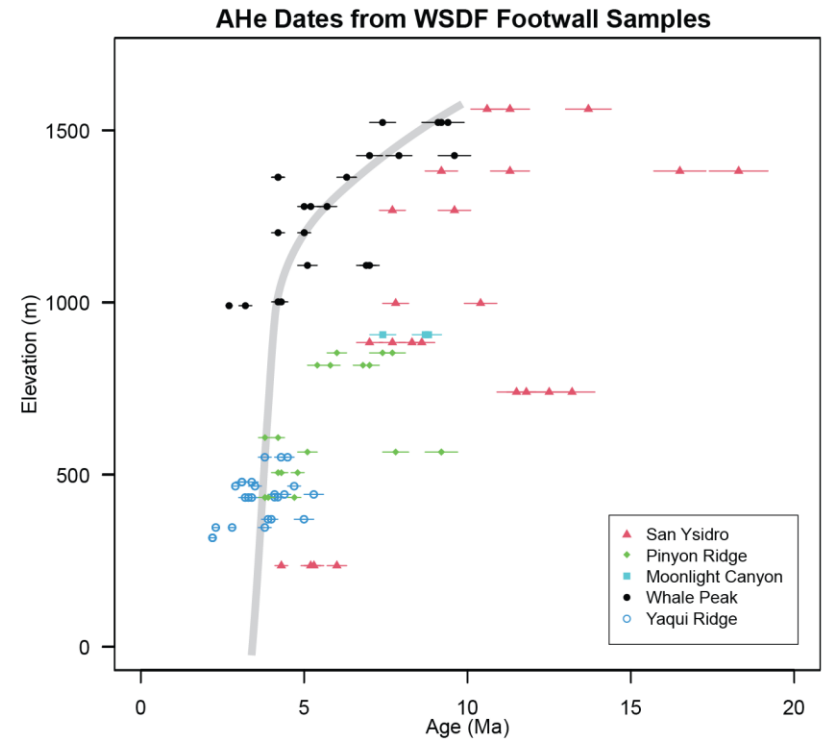

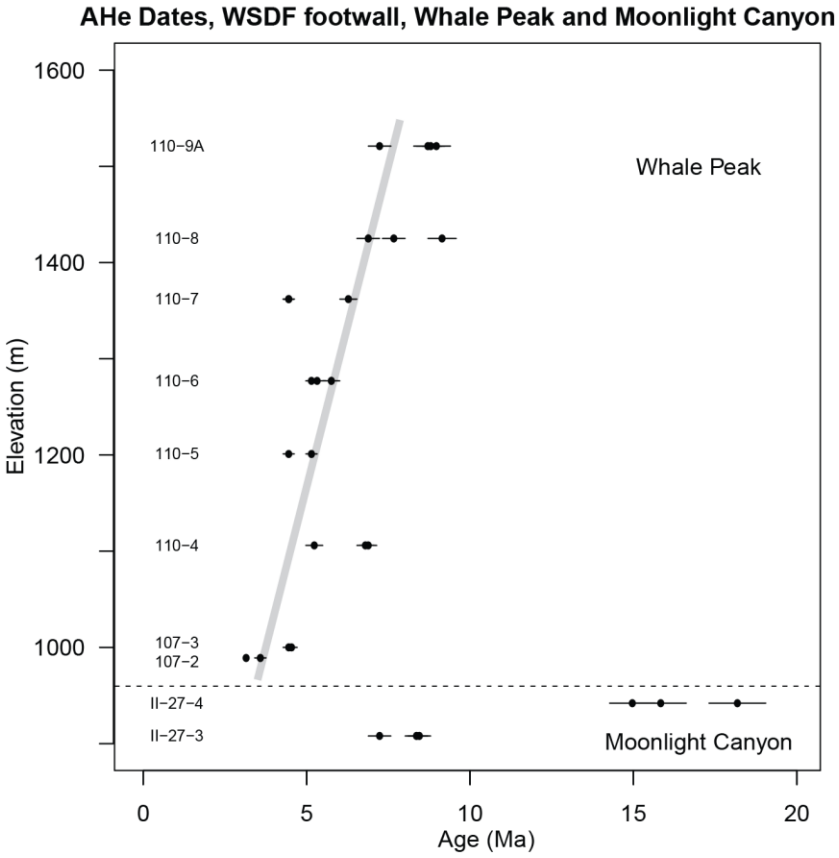

Figure 2.4.

(upper) AHe dates with elevation from five WSDF footwall locations (from Shirvell et al., 2009). The Pinyon Ridge and Whale Peak data may signal an increase in WSDF activity around 5Ma, indicated by steepening of the gray line drawn through data. This acceleration likely documents the exhumation of Whale Peak during onset of or increase in activity of the WSDF at this time.

(lower) Plot of the AHe dates with elevation from Shirvell (2006; et al. 2009) at Whale Peak and Moonlight Canyon in the footwall of the WSDF fault near the FCVB and Whale Peak with samples labeled.

On both plots, each sample is shown by multiple points representing each analyzed grain within that sample. The elevation of the samples increases away from the WSDF, so the lowest samples from each location are the closest to the fault. Grey line indicates the trend of the dates with elevation.

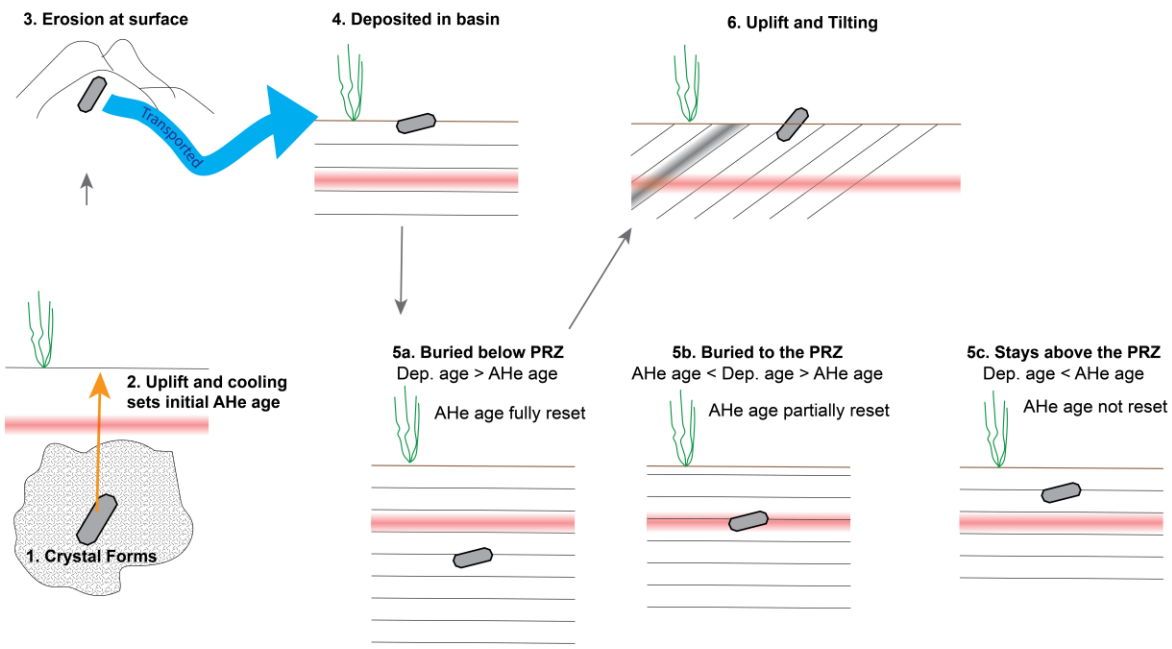

Figure 2.5. Cartoon illustrating detrital thermochronology and how reset, partially reset, and not reset ages are determined. Most of the samples from the proto-Vallecito fault hanging wall are represented by step 5b or 5c.

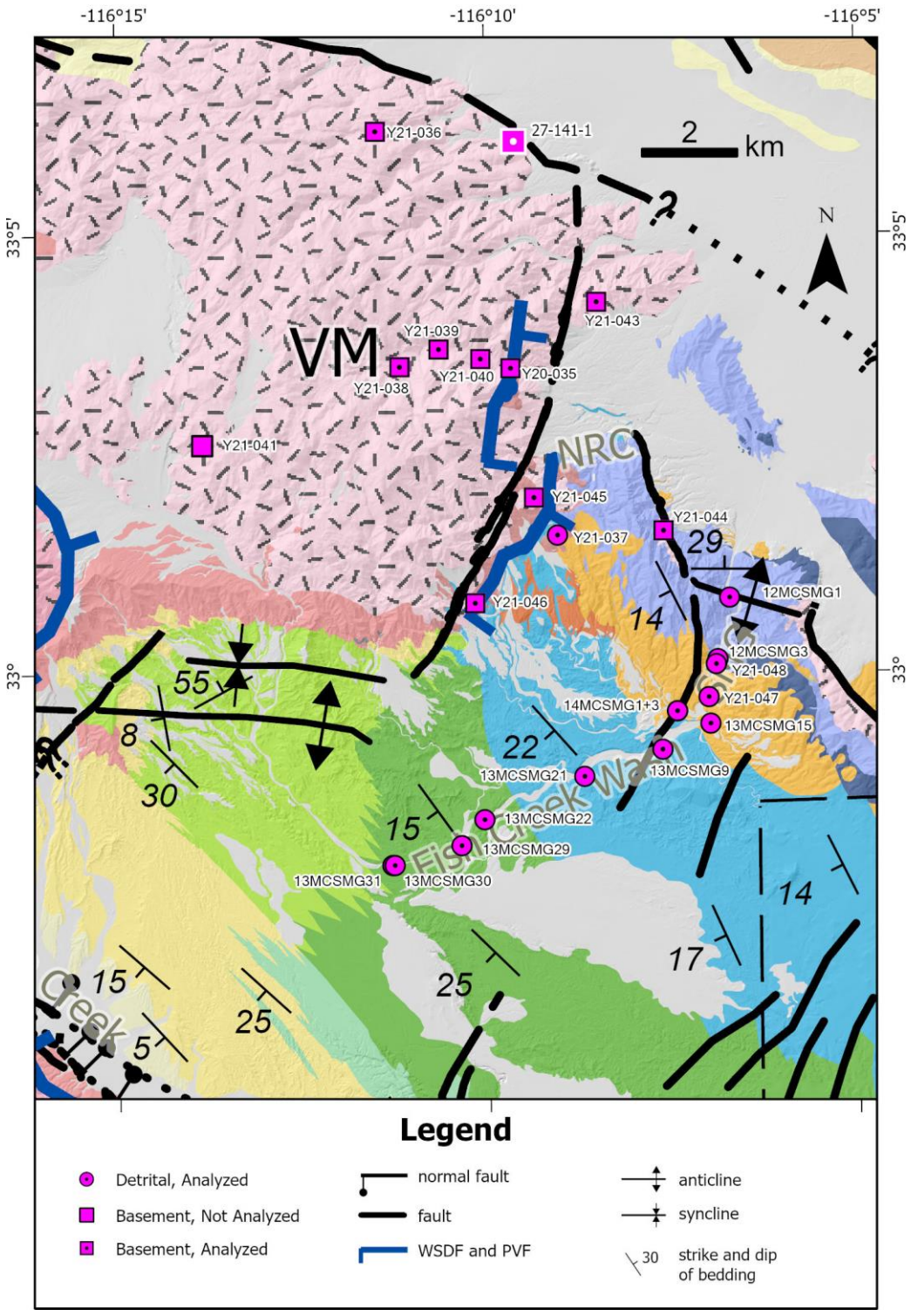

Figure 2.6. Locations of FCVB AHe samples analyzed in this study. Circles indicate detrital samples, squares indicate crystalline rock samples, and a black dot in the center indicates an analyzed sample. White dot in sample 27-141-1 indicates data from Shirvell et al., 2009. Sample Y21-041 did not yield datable material. See Figure 2.1 for unit labels and full map legend.

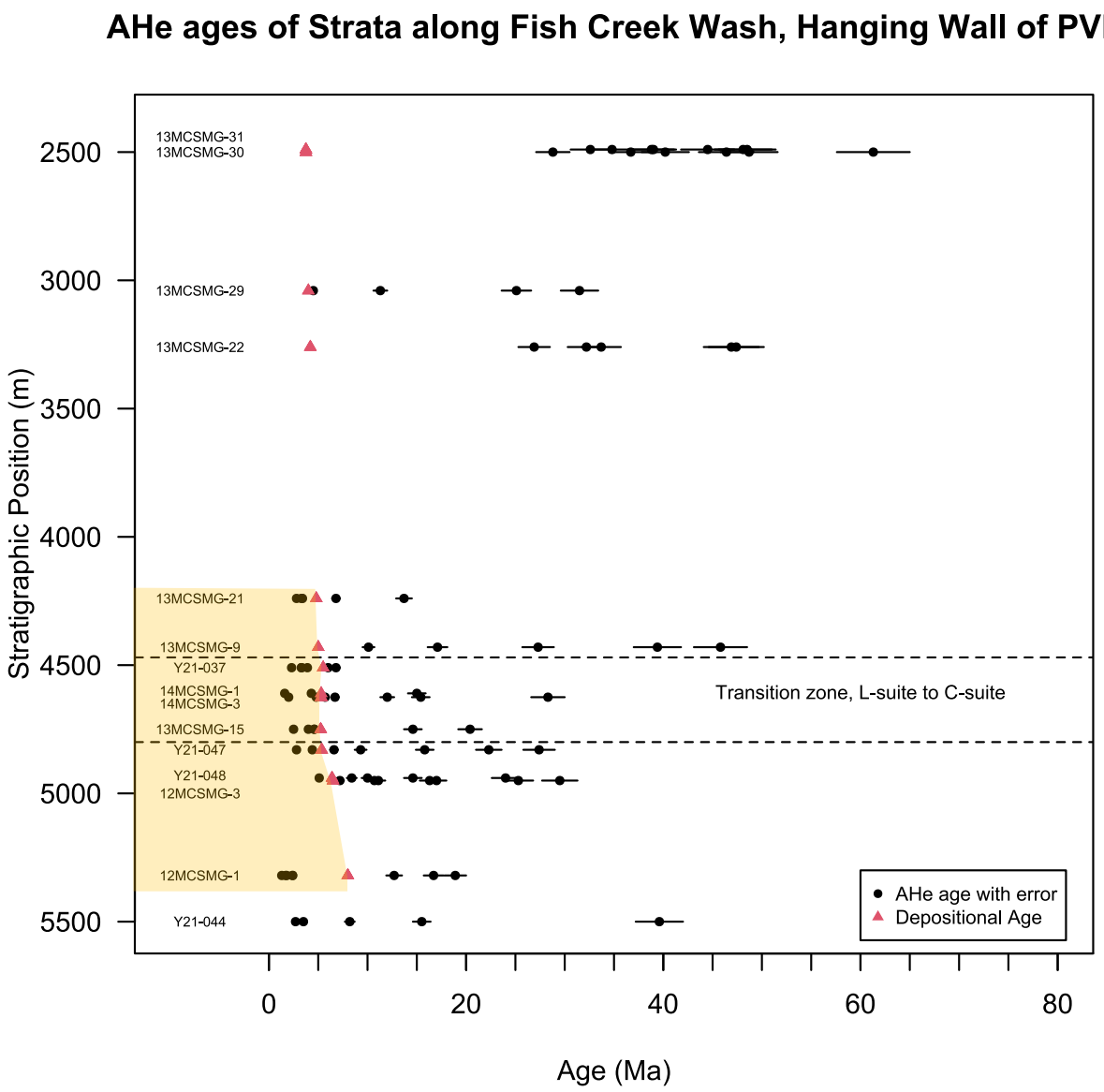

Figure 2.7. Plot of apatite helium dates from the hanging wall of the proto-Vallecito fault. Samples are plotted relative to stratigraphic position and with the depositional age. Locally sourced samples are below the transition zone and Colorado River-derived samples are above it. Sample 13MCSMG30 is L-suite. Sample Y21-044 is crystalline basement.

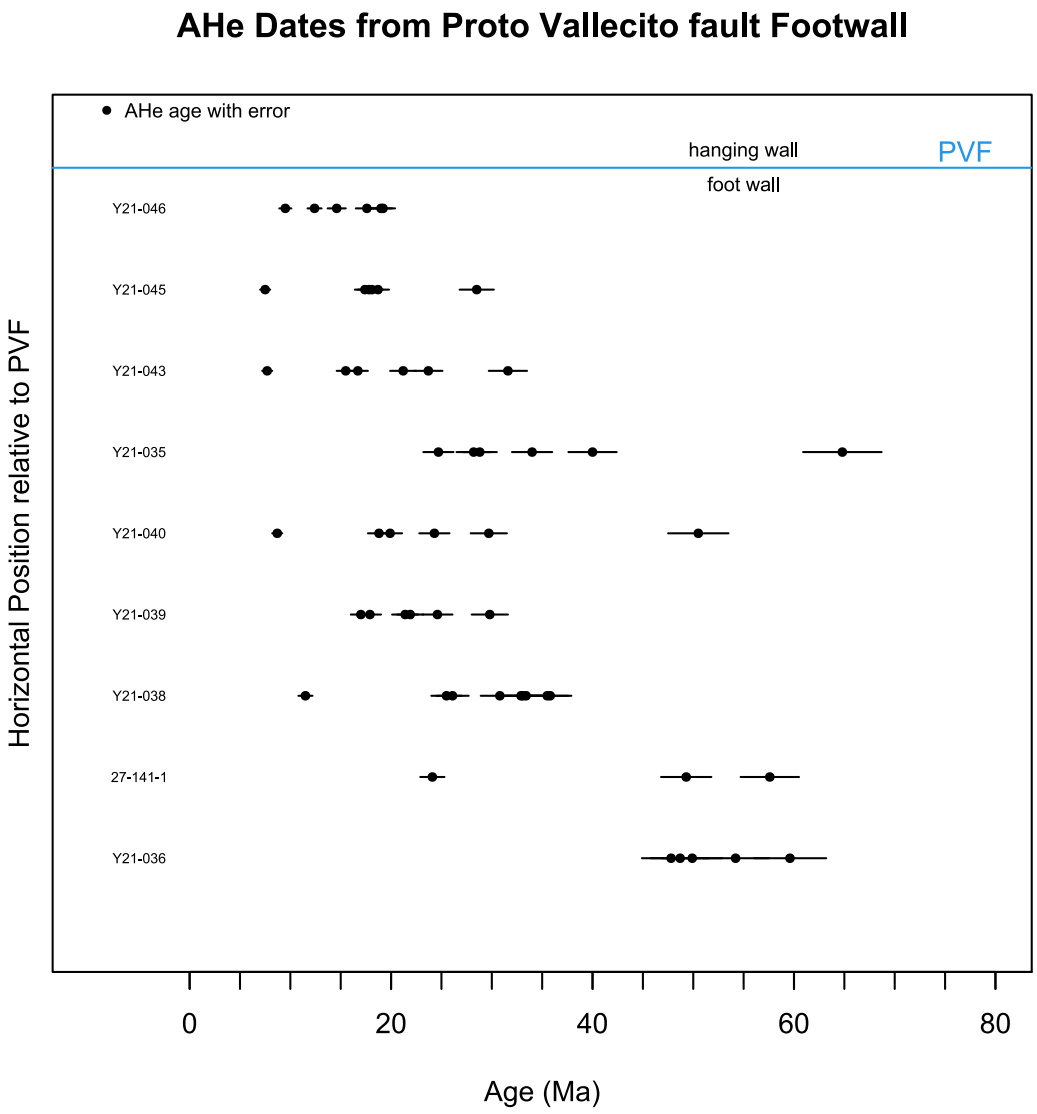

Figure 2.8. Plot of apatite helium dates from the foot wall of the proto-Vallecito fault. Samples are plotted with respect to proximity to the Vallecito fault in map view.

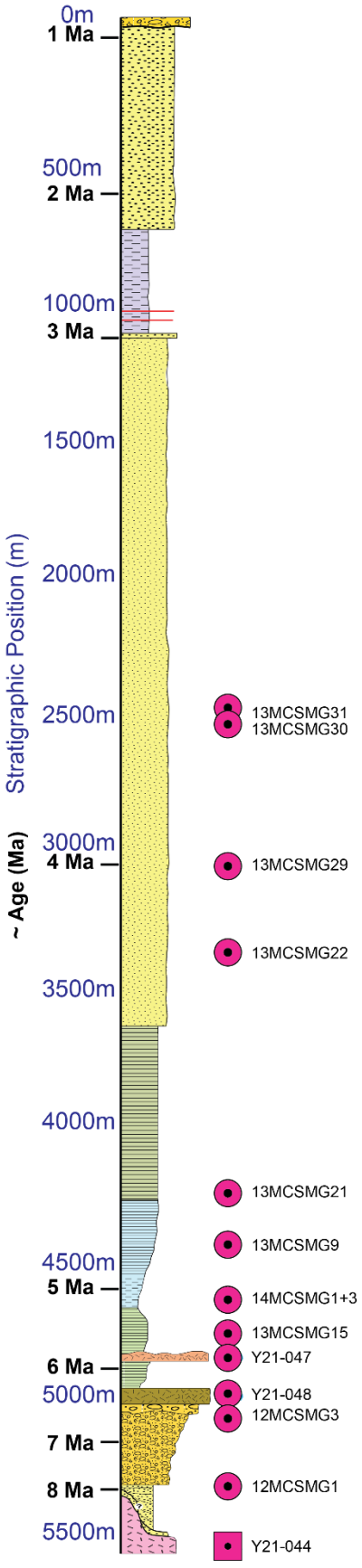

Figure 2.9. Stratigraphic column of the Fish Creek Vallecito basin with the locations of apatite samples used in this study. Samples collected by Cloos (2014) in green and samples collected for this study in blue.

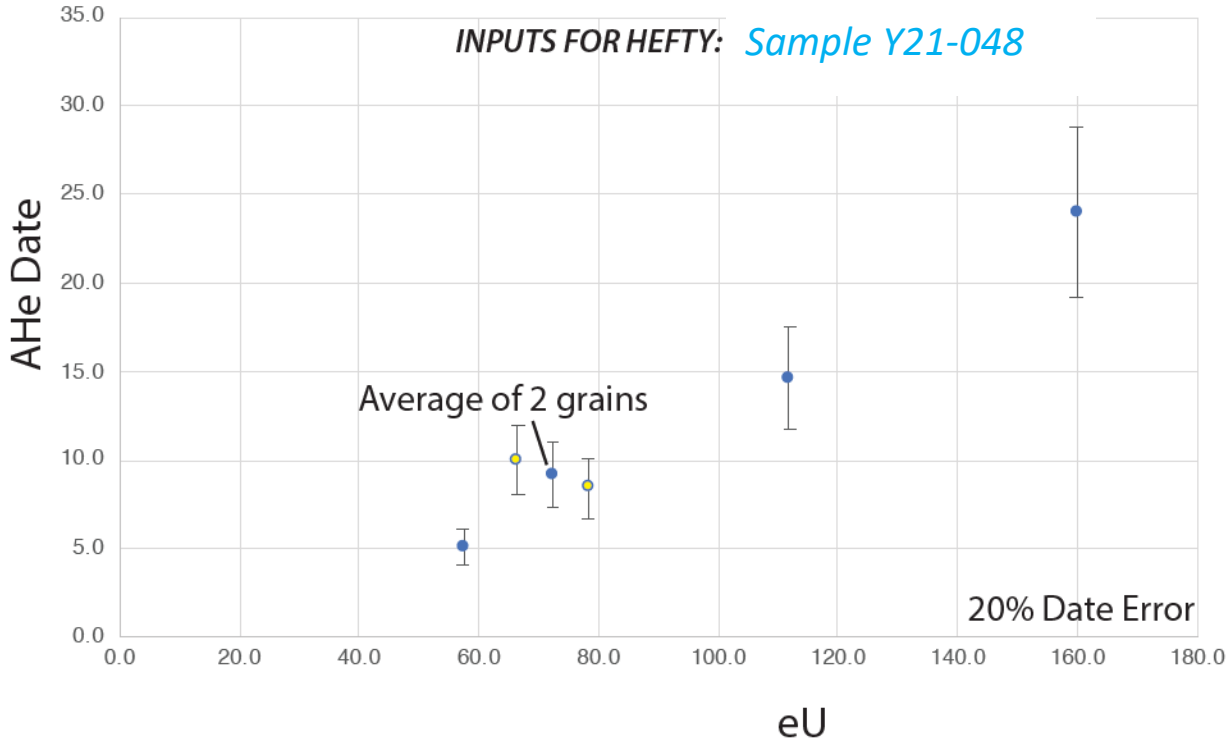

Figure 2.10. Plot of AHe date versus effective uranium concentration for sample Y21-048. 20% date error was used, and two grains were averaged to produce an input that will be more successful in the inverse model.

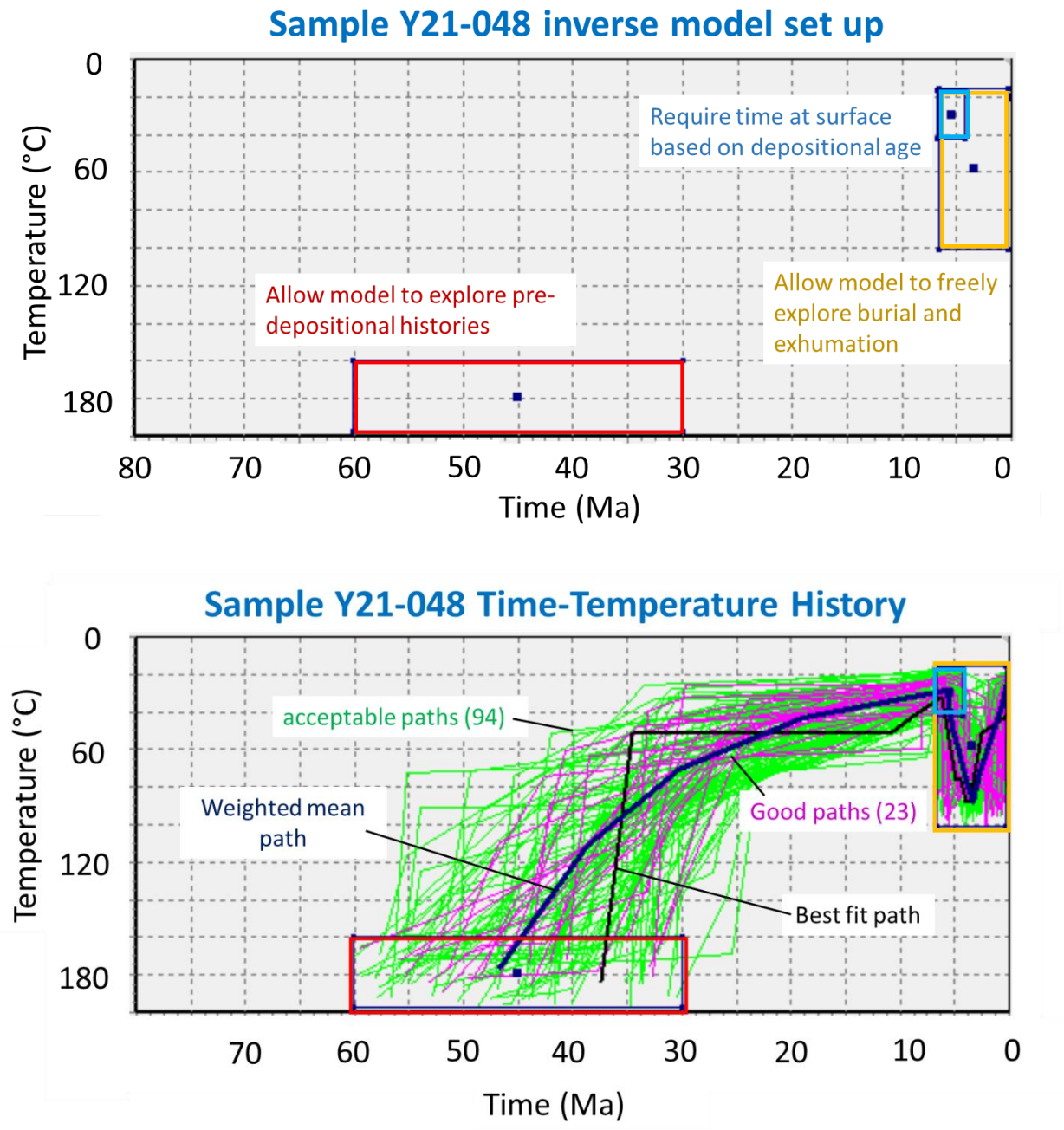

Figure 2.11. Inverse model set up for sample Y21-048. Boxes drawn on the upper plot indicate the constraints the time-temperature paths must fall into. Lower plot shows the results of this model, with good time-temperature paths in pink and acceptable paths in green.

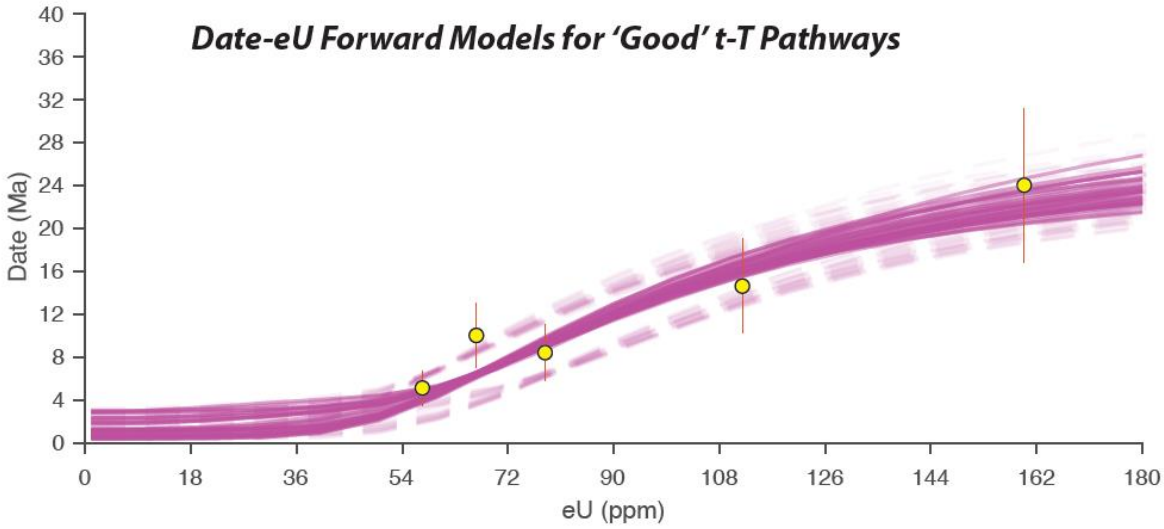

Figure 2.12. Good paths from the inverse model were used in a forward model to create this date versus effective uranium plot. When the forward model results are compared to the sample data, the date-eU relationship is similar.

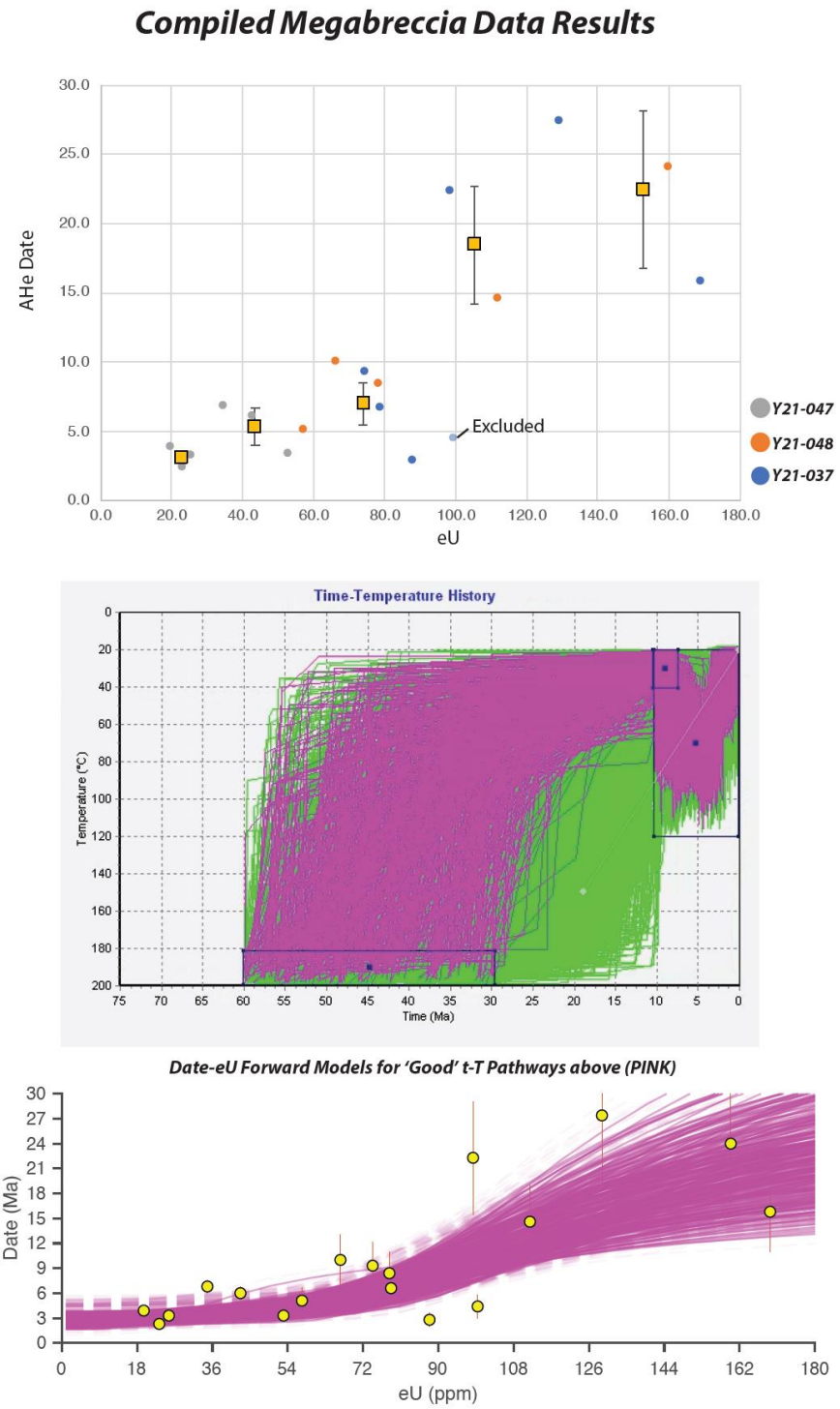

Figure 2.13. (upper) Model inputs for all megabreccia samples averaged together. Yellow squares indicate model inputs averaged from data. (middle) Inverse model results showing good, pink, and acceptable, green, time-temperature paths. (lower) A forward model using the good paths produces date-eU curves that are consistent with the date-eU points from the data (yellow points).

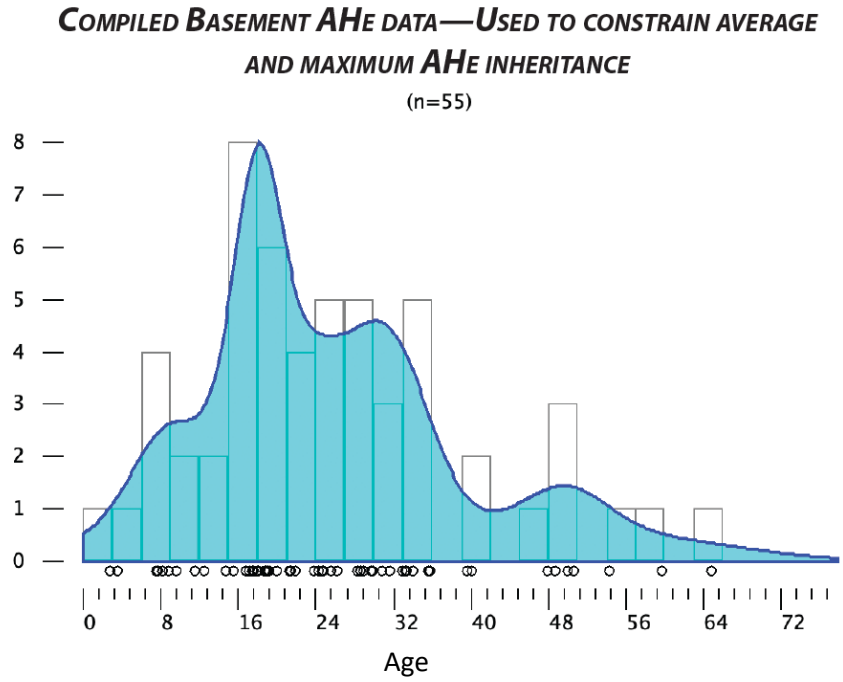

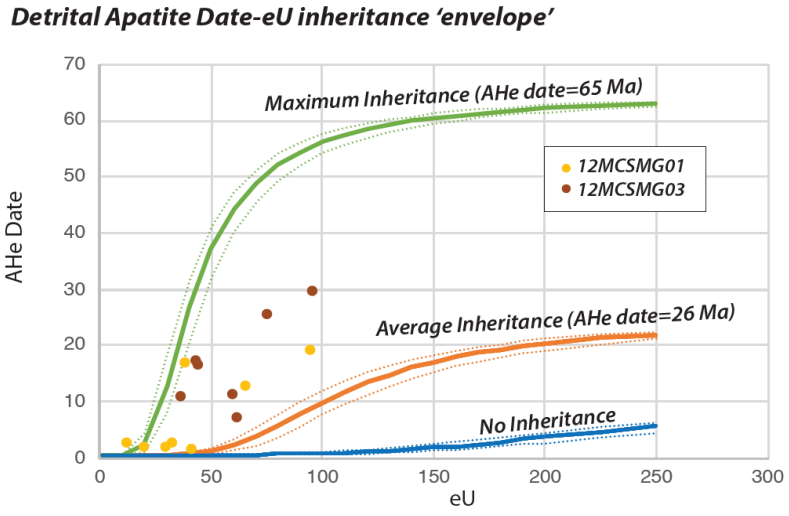

Figure 2.14. (Upper) Histogram of dates from the bedrock samples in the PVF footwall. (Lower) Plot of predicted Apatite U-Th/He date versus uranium content envelopes for hypothetical samples based on the inheritance and of samples from the Elephant Trees formation derived from erosion of the foot wall of the proto-Vallecito fault. Initial ages from zero to 65 Ma. The spread of observed ages of locally-derived sediment after burial and exhumation within the FCVB falls within the maximum and minimum envelope of inherited, partially reset ages predicted from forward model.

Table 2.1. Summary of samples used for Apatite (U-Th)/He dating

Location	HW/ FW	Sample	Formation/ Unit	Member	Depositional Age	Strat Type	Latitude[1]	Longitude[1]	Collection Source[2]
Fish Creek Wash	HW	13MCSMG31	Arroyo Diablo	-	~4.0-3.5 Ma	C-Suite	32.963591	-116.18833	Cloos, 2014
Fish Creek Wash	HW	13MCSMG30	Olla	-	~4.0-3.5 Ma	L-Suite	32.963579	-116.187827	Cloos, 2014
Fish Creek Wash	HW	13MCSMG29	Arroyo Diablo	-	~4.0 Ma	C-Suite	32.967286	-116.172791	Cloos, 2014
Fish Creek Wash	HW	13MCSMG22	Arroyo Diablo	-	~4.2 Ma	C Suite	32.972186	-116.167556	Cloos, 2014
Fish Creek Wash	HW	13MCSMG21	Deguynos	Yuha	~4.8 Ma	C-Suite	32.980295	-116.144973	Cloos, 2014
Fish Creek Wash	HW	13MCSMG9	Deguynos	Mud Hills[3]	~5.0 Ma	C-Suite	32.985333	-116.12733	Cloos, 2014
N of Lycium Wash	HW	Y21-037	mbx[4]	-	~5.5 Ma	L-suite	33.02615	-116.15067	This Study
Fish Creek Wash	HW	13MCSMG15	Latrania	Wind Caves	5.3-5.2 Ma	C-Suite	32.990199	-116.116472	Cloos, 2014
Fish Creek Wash	HW	14MCSMG1	Latrania	Wind Caves	~5.3 Ma	C-Suite	32.99257	-116.123962	Cloos, 2014
Fish Creek Wash	HW	14MCSMG3	Latrania	Wind Caves	~5.3 Ma	L-Suite	32.99257	-116.123962	Cloos, 2014
Fish Creek Wash	HW	Y21-047	Latrania	upper mbx[4]	~5.4Ma	L-Suite	32.99524	-116.11681	This Study
Fish Creek Wash	HW	Y21-048	lower mbx[4]	-	~5.5	L-suite	33.00244	-116.11477	This Study
Fish Creek Wash	HW	12MCSMG3	Elephant Trees	-	~6.5 Ma	L-Suite	33.00151	-116.115128	Cloos, 2014
Fish Creek Wash	HW	12MCSMG1	Elephant Trees	-	~8.0 Ma	L-Suite	33.014097	-116.112005	Cloos, 2014
W of SMG	HW	Y21-044	Basement	-	-	Source	33.02689	-116.12683	This Study
VM, Alma Wash	FW?	Y20-035	Basement	-	-	Source	33.05789	-116.16106	This Study
VM, Alma Wash	FW	Y21-038	Basement	-	-	Source	33.05826	-116.18604	This Study
VM, Alma Wash	FW	Y21-039	Basement	-	-	Source	33.06154	-116.17724	This Study
VM, Alma Wash	FW	Y21-040	Basement	-	-	Source	33.05968	-116.16784	This Study
VM, NE Hapaha Flt	FW	Y21-041[5]	Basement	-	-	Source	33.04351	-116.23071	This Study
VM, N of Eleph. T.	FW?	Y21-043	Basement	-	-	Source	33.07037	-116.14162	This Study
VM, S of NRC	FW	Y21-045	Basement	-	-	Source	33.0333	-116.15595	This Study
VM, S end PVF	FW	Y21-046	Basement	-	-	Source	33.01324	-116.1692	This Study
VM, NE margin VM	FW	Y21-036	Basement	-	-	Source	33.103	-116.1912	This Study
VM, NE margin VM	FW	27-141-1	Basement	-	-	Source	33.101	-116.16	Shirvell, 06; 09

1. Lat. long. errors for samples from this study are 3 m except samples Y21-046 (9m) and Y21-048 (4m). Other studies not reported.
2. Sample collection by Cloos, 2014, This Study, or Shirvell 2006. Sample 27-141-1 analysis reported in Shirvell 2006 and Shirvell et al., 2009
3. Rhythmites
4. Sampled single clast within the megabreccia
5. No apatites found in sample during mineral seperation process

Eleph. T = Elephant Trees, Flt = flat, FW = foot wall of PVF, HW = hanging wall of PVF, mbx = megabreccia, NRC = No Return Canyon, PVF = proto-Vallecito fault, SMG = Split Mountain Gorge, VM = Vallecito Mountains

Table 2.2. Apatite (U-Th)/He cooling ages from the hanging wall of the proto-Vallecito fault

Sample	Grain	AHe age (Ma)	Error (Ma)	Depositional Age (Ma)	Elevation (m)	Stratigraphic depth (m)
13MCSMG-31	1	44.5	2.7	3.75	296	2490
13MCSMG-31	2	39	2.3	3.75	296	2490
13MCSMG-31	3	48.1	2.9	3.75	296	2490
13MCSMG-31	4	32.6	2	3.75	296	2490
13MCSMG-31	5	38.8	2.3	3.75	296	2490
13MCSMG-31	6	48.5	2.9	3.75	296	2490
13MCSMG-31	7	34.8	2.1	3.75	296	2490
13MCSMG-30	1	28.8	1.7	3.75	297	2500
13MCSMG-30	3	48.7	2.9	3.75	297	2500
13MCSMG-30	4	61.3	3.7	3.75	297	2500
13MCSMG-30	5	40.2	2.4	3.75	297	2500
13MCSMG-30	6	36.7	2.2	3.75	297	2500
13MCSMG-30	7	46.4	2.8	3.75	297	2500
13MCSMG-29	1	4.5	0.3	4	250	3040
13MCSMG-29	3	11.3	0.7	4	250	3040
13MCSMG-29	4	31.5	1.9	4	250	3040
13MCSMG-29	5	25.1	1.5	4	250	3040
13MCSMG-22	1	46.9	2.8	4.2	235	3260
13MCSMG-22	2	32.2	1.9	4.2	235	3260
13MCSMG-22	3	26.9	1.6	4.2	235	3260
13MCSMG-22	4	33.7	2	4.2	235	3260
13MCSMG-22	6	47.4	2.8	4.2	235	3260
13MCSMG-21	1	3.4	0.2	4.8	190	4240
13MCSMG-21	2	6.8	0.4	4.8	190	4240
13MCSMG-21	3	3.3	0.2	4.8	190	4240
13MCSMG-21	5	2.8	0.2	4.8	190	4240
13MCSMG-21	6	13.7	0.8	4.8	190	4240
13MCSMG-9	1	10.1	0.6	5	164	4430
13MCSMG-9	2	27.3	1.6	5	164	4430
13MCSMG-9	3	17.1	1	5	164	4430
13MCSMG-9	4	39.4	2.4	5	164	4430
13MCSMG-9	7	45.8	2.7	5	164	4430
Y21-037	1	2.3	0.1	5.5	416	4510
Y21-037	2	6.8	0.4	5.5	416	4510
Y21-037	3	3.9	0.2	5.5	416	4510
Y21-037	4	3.3	0.2	5.5	416	4510
Y21-037	5	6	0.4	5.5	416	4510
Y21-037	6	3.3	0.2	5.5	416	4510
14MCSMG-1	1	15	0.9	5.3	152	4625
14MCSMG-1	2	1.6	0.1	5.3	152	4625
14MCSMG-1	6	4.3	0.3	5.3	152	4625
14MCSMG-3	1	2	0.1	5.3	152	4625
14MCSMG-3	2	5.7	0.3	5.3	152	4625
14MCSMG-3	3	12	0.7	5.3	152	4625
14MCSMG-3	4	15.4	0.9	5.3	152	4625
14MCSMG-3	5	6.7	0.4	5.3	152	4625
14MCSMG-3	6	4.8	0.3	5.3	152	4625
14MCSMG-3	7	28.3	1.7	5.3	152	4625

Table 2.2. Apatite (U-Th)/He cooling ages from the hanging wall of the proto-Vallecito fault, continued

Sample	Grain	AHe age (Ma)	Error (Ma)	Depositional Age (Ma)	Elevation (m)	Stratigraphic depth (m)
13MCSMG-15	1	2.5	0.2	5.25	166	4750
13MCSMG-15	2	4	0.2	5.25	166	4750
13MCSMG-15	3	20.4	1.2	5.25	166	4750
13MCSMG-15	4	4.6	0.3	5.25	166	4750
13MCSMG-15	5	4.6	0.3	5.25	166	4750
13MCSMG-15	7	14.6	0.9	5.25	166	4750
Y21-047	1	2.8	0.2	5.35	142	4830
Y21-047	2	6.6	0.4	5.35	142	4830
Y21-047	3	9.3	0.6	5.35	142	4830
Y21-047	4	27.4	1.6	5.35	142	4830
Y21-047	5	4.4	0.3	5.35	142	4830
Y21-047	6	15.8	0.9	5.35	142	4830
Y21-047	7	22.3	1.3	5.35	142	4830
Y21-048	1	8.4	0.5	6.4	120	4940
Y21-048	2	24	1.4	6.4	120	4940
Y21-048	3	5.1	0.3	6.4	120	4940
Y21-048	4	14.6	0.9	6.4	120	4940
Y21-048	5	10	0.6	6.4	120	4940
12MCSMG-3	1	11.1	0.7	6.5	125	4950
12MCSMG-3	2	10.7	0.6	6.5	125	4950
12MCSMG-3	3	25.3	1.5	6.5	125	4950
12MCSMG-3	4	7.2	0.4	6.5	125	4950
12MCSMG-3	5	17	1	6.5	125	4950
12MCSMG-3	6	29.5	1.8	6.5	125	4950
12MCSMG-3	7	16.3	1	6.5	125	4950
12MCSMG-1	1	2.4	0.1	8	104	5320
12MCSMG-1	2	16.7	1	8	104	5320
12MCSMG-1	3	2.4	0.1	8	104	5320
12MCSMG-1	4	1.3	0.1	8	104	5320
12MCSMG-1	5	18.9	1.1	8	104	5320
12MCSMG-1	6	1.8	0.1	8	104	5320
12MCSMG-1	7	1.7	0.1	8	104	5320
12MCSMG-1	8	12.7	0.8	8	104	5320
Y21-044	1	2.7	0.2	-	252	5500
Y21-044	2	39.6	2.4	-	252	5500
Y21-044	3	3.5	0.2	-	252	5500
Y21-044	4	15.5	0.9	-	252	5500
Y21-044	5	8.2	0.5	-	252	5500

Samples beingnning with Y were collected for this study, other samples collected by Cloos, 2014. All apatite mineral seperates were analysed for this study.

Table 2.3. Apatite (U-Th)/He cooling ages from the foot wall of the proto-Vallecito fault

Sample	Grain	AHe Age (Ma)	Error (Ma)	Elevation (m)	Map Unit	Position
Y21-043	1	7.7	0.5	244	Basement	7
Y21-043	2	21.2	1.3	244	Basement	7
Y21-043	3	16.7	1	244	Basement	7
Y21-043	4	23.7	1.4	244	Basement	7
Y21-043	5	15.5	0.9	244	Basement	7
Y21-043	6	31.6	1.9	244	Basement	7
Y21-035	1	64.8	3.9	342	Basement	6
Y21-035	3	34	2	342	Basement	6
Y21-035	4	28.2	1.7	342	Basement	6
Y21-035	5	24.7	1.5	342	Basement	6
Y21-035	6	40	2.4	342	Basement	6
Y21-035	7	28.8	1.7	342	Basement	6
Y21-046	1	9.5	0.6	355	Basement	9
Y21-046	2	19.2	1.2	355	Basement	9
Y21-046	3	17.6	1.1	355	Basement	9
Y21-046	4	14.6	0.9	355	Basement	9
Y21-046	5	12.4	0.7	355	Basement	9
Y21-046	6	19	1.1	355	Basement	9
Y21-036	1	59.6	3.6	409	Basement	1
Y21-036	2	49.9	3	409	Basement	1
Y21-036	3	48.7	2.9	409	Basement	1
Y21-036	4	47.8	2.9	409	Basement	1
Y21-036	5	54.2	3.3	409	Basement	1
Y21-040	1	50.5	3	418	Basement	5
Y21-040	2	8.7	0.5	418	Basement	5
Y21-040	3	24.3	1.5	418	Basement	5
Y21-040	4	29.7	1.8	418	Basement	5
Y21-040	5	19.9	1.2	418	Basement	5
Y21-040	7	18.8	1.1	418	Basement	5
Y21-045	1	17.4	1	431	Basement	8
Y21-045	2	18.7	1.1	431	Basement	8
Y21-045	3	28.5	1.7	431	Basement	8
Y21-045	4	17.8	1.1	431	Basement	8
Y21-045	5	7.5	0.5	431	Basement	8
Y21-045	6	18.1	1.1	431	Basement	8
Y21-039	1	29.8	1.8	484	Basement	4
Y21-039	2	17	1	484	Basement	4
Y21-039	3	17.9	1.1	484	Basement	4
Y21-039	4	21.9	1.3	484	Basement	4
Y21-039	7	21.4	1.3	484	Basement	4
Y21-039	6	24.6	1.5	484	Basement	4

Table 2.3. Apatite (U-Th)/He cooling ages from the foot wall of the proto-Vallecito fault, continued

Sample	Grain	AHe Age (Ma)	Error (Ma)	Elevation (m)	Map Unit	Position
Y21-038	1	33.1	2	569	Basement	3
Y21-038	2	33.4	2	569	Basement	3
Y21-038	3	26.1	1.6	569	Basement	3
Y21-038	4	32.9	2	569	Basement	3
Y21-038	5	35.5	2.1	569	Basement	3
Y21-038	6	11.5	0.7	569	Basement	3
Y21-038	7	25.5	1.5	569	Basement	3
Y21-038	8	35.8	2.1	569	Basement	3
Y21-038	9	30.8	1.9	569	Basement	3
27-141-1	1	24.1	1.2	200	Basement	2
27-141-1	2	57.6	2.9	200	Basement	2
27-141-1	3	49.3	2.5	200	Basement	2

All samples from this study except sample 27-141-1, which was collected by Shirvell, 2006 and analyzed by Shirvell, 2006 and Shirvell et al., 2009

REFERENCES

Allen, P.A., and Allen, J.R., 2013. Basin analysis: Principles and application to petroleum play assessment. John Wiley & Sons.

Alasad, R., Olariu, C., and Steel, R.J., 2023, Alluvial fan and fan delta facies architecture recording initial marine flooding in the MIO-PLIOCENE syn-rift sequence of the Fish CREEK-VALLECITO Basin, southern California: Basin Research, v. 35, p. 1619–1649, doi:10.1111/bre.12767.

Axen, G.J., and Fletcher, J.M., 1998, Late Miocene-Pleistocene Extensional Faulting, Northern Gulf of California, Mexico and Salton Trough, California: International Geology Review, v. 40, p. 217–244, doi:10.1080/00206819809465207.

Cloos, M., 2014, Detrital Zircon U-Pb and (U-Th)/He Geo-Thermochronometry and Submarine Turbidite Fan Development in the Mio-Pliocene Gulf of California, Fish Creek-Vallecito Basin, Southern California [Masters]: University of Texas at Austin, 216 p.

Crow, R.S., Schwing, J., Karlstrom, K.E., Heizler, M., Pearthree, P.A., House, P.K., Dulin, S., Jänecke, S.U., Stelten, M., and Crossey, L.J., 2021, Redefining the age of the lower Colorado River, southwestern United States: Geology, v. 49, p. 635–640, doi:10.1130/G48080.1.

Dorsey, R.J., Axen, G.J., Peryam, T.C., and Kairouz, M.E., 2012, Initiation of the Southern Elsinore Fault at ~1.2 Ma: Evidence from the Fish Creek-Vallecito Basin, southern California:

SOUTHERN ELSINORE FAULT INITIATION: Tectonics, v. 31, p. n/a-n/a, doi:10.1029/2011TC003009.

Dorsey, R.J., Fluette, A., McDougall, K., Housen, B.A., Janecke, S.U., Axen, G.J., and Shirvell, C.R., 2007, Chronology of Miocene–Pliocene deposits at Split Mountain Gorge, Southern California: A record of regional tectonics and Colorado River evolution: Geology, v. 35, p. 57, doi:10.1130/G23139A.1.

Dorsey, R.J., Housen, B.A., Janecke, S.U., Fanning, C.M., and Spears, A.L.F., 2011, Stratigraphic record of basin development within the San Andreas fault system: Late Cenozoic Fish Creek-Vallecito basin, southern California: Geological Society of America Bulletin, v. 123, p. 771–793, doi:10.1130/B30168.1.

Esri, 2022, "Topographic" [basemap]. 1:6,500,000. "World Topographic Map". https://www.arcgis.com/home/item.html?id=10df2279f9684e4a9f6a7f08febac2a9. (September, 2023)

Flowers, R.M., Ketcham, R.A., Shuster, D.L., and Farley, K.A., 2009, Apatite (U–Th)/He thermochronometry using a radiation damage accumulation and annealing model: Geochimica et Cosmochimica Acta, v. 73, p. 2347–2365, doi:10.1016/j.gca.2009.01.015.

Fox, M., Dai, J., and Carter, A., 2019, Badly Behaved Detrital (U-Th)/He Ages: Problems With He Diffusion Models or Geological Models? Geochemistry, Geophysics, Geosystems, v. 20, p. 2418–2432, doi:10.1029/2018GC008102.

Fuis, G.S., Mooney, W.D., Healy, J.H., McMechan, G.A., and Lutter, W.J., 1984, A seismic refraction survey of the Imperial Valley Region, California: Journal of Geophysical Research: Solid Earth, v. 89, p. 1165–1189, doi:10.1029/JB089iB02p01165.

Guenthner, W.R., Reiners, P.W., DeCelles, P.G., and Kendall, J., 2015, Sevier belt exhumation in central Utah constrained from complex zircon (U-Th)/He data sets: Radiation damage and He inheritance effects on partially reset detrital zircons: Geological Society of America Bulletin, v. 127, p. 323–348, doi:10.1130/B31032.1.

Han, L. et al., 2016, Continental rupture and the creation of new crust in the Salton Trough rift, Southern California and northern Mexico: Results from the Salton Seismic Imaging Project: Continental Rupture in the Salton Trough: Journal of Geophysical Research: Solid Earth, v. 121, p. 7469–7489, doi:10.1002/2016JB013139.

He, J., Thomson, S.N., Reiners, P.W., Hemming, S.R., and Licht, K.J., 2021, Rapid erosion of the central Transantarctic Mountains at the Eocene-Oligocene transition: Evidence from skewed (U-Th)/He date distributions near Beardmore Glacier: Earth and Planetary Science Letters, v. 567, p. 117009, doi:10.1016/j.epsl.2021.117009.

Janecke, S.U., Dorsey, R.J., Forand, D., Steely, A.N., Kirby, S.M., Lutz, A.T., Housen, B.A., Belgarde, B., Langenheim, V.E., and Rittenour, T.M., 2010, High Geologic Slip Rates since Early Pleistocene Initiation of the San Jacinto and San Felipe Fault Zones in the San Andreas Fault System: Southern California, USA, in Geological Society of America Special Papers, Geological Society of America, v. 475, p. 1–48, doi:10.1130/2010.2475.

Kerr, D. R., 1982, Early Neogene continental sedimentation, western Salton Trough, California [M. S. thesis]: San Diego State University, 138 p.

Ketcham, R.A., 2005, Forward and Inverse Modeling of Low-Temperature Thermochronometry Data: Reviews in Mineralogy and Geochemistry, v. 58, p. 275–314, doi:10.2138/rmg.2005.58.11.

Kolawole, F., and Evenick, J.C., 2023, Global distribution of geothermal gradients in sedimentary basins: Geoscience Frontiers, v. 14, p. 101685, doi:10.1016/j.gsf.2023.101685.

Lachenbruch, A.H., Sass, J.H., and Galanis, S.P., 1985, Heat flow in southernmost California and the origin of the Salton Trough: Journal of Geophysical Research, v. 90, p. 6709, doi:10.1029/JB090iB08p06709.

Reiners, P.W., and Brandon, M.T., 2006, Using thermochronology to understand orogenic erosion: Annual Review of Earth and Planetary Sciences, v. 34, p. 419–466, doi:10.1146/annurev.earth.34.031405.125202.

Shirvell, C.R., 2006, Pliocene Exhumation along the West Salton Detachment System and Tectonic Evolution of the Fish Creek-Vallecito Supradetachment Basin, Salton Trough, Southern California [Masters Thesis]: University of California, Los Angeles.

Shirvell, C.R., Stockli, D.F., Axen, G.J., and Grove, M., 2009, Miocene-Pliocene exhumation along the west Salton detachment fault, southern California, from (U-Th)/He thermochronometry of apatite and zircon: Tectonics, v. 28, p. 14, doi:10.1029/2007TC002172.

Todd, V. (1977). Geologic map of the Agua Caliente Springs quadrangle, San Diego County, California. USGS Open File Report 077-742.

U.S. Geological Survey, 20220815, USGS Lidar Point Cloud CA_Eastern_San_Diego_Co_Lidar_2016_B16: U.S. Geological Survey. Distributed by OpenTopography. Accessed: December 2019.

U.S. Geological Survey and California Geological Survey (2004). Quaternary fault and fold database for the United States, from USGS website available at https://www.usgs.gov/naturalhazards/ earthquake-hazards/faults (last accessed February 2021).

U.S. Geological Survey 3DEP, 20180313, USGS 13 arc-second n33w117 1 x 1 degree: U.S. Geological Survey. https://apps.nationalmap.gov/downloader/. Accessed: October, 2022.

U.S. Geological Survey 3DEP, 20190924, USGS 13 arc-second n34w117 1 x 1 degree: U.S. Geological Survey. https://apps.nationalmap.gov/downloader/. Accessed: October, 2022.

Winker, C.D., 1987, Neogene stratigraphy of the Fish Creek-Vallecito section, Southern California: implications for early history of the northern Gulf of California and Colorado Delta [Ph.D.]: The University of Arizona, 528 p.

Winker, C.D., and Kidwell, S.M., 1986, Paleocurrent evidence for lateral displacement of the Pliocene Colorado River delta by the San Andreas fault system, southeastern California: Geology, v. 14, p. 788, doi:10.1130/0091-7613(1986)14<788:PEFLDO>2.0.CO;2.

Winker, C.D., and Kidwell, S.M., 1996, Stratigraphy of a Marine Rift Basin: Neogene of the Western Salton Trough, California, in Abbott, P.L. and Cooper, J.D. eds., Field Conference Guide 1996, Pacific Section SEPM, Pacific Section AAPG GB73, v. Book 80, p. 295–336.

A2 - APPENDIX TO CHAPTER 2

The appendix to Chapter 2 includes three tables listed and described below.

Table A2.1. Summary of Analyzed and Unanalyzed Apatite (U-Th)/He Samples from the Northern Fish Creek Vallecito Basin

Summarized all samples collected by Cloos, 2014 and Young, 2023 (this study) for AHe analysis, including samples that were not analyzed.

Table A2.2: Reduced Apatite (U-Th[Sm])/He Data

Reduced (U-Th[Sm])/He data from this study, used to make plots and to implement thermal models.

Table A2.3: Raw Apatite (U-Th[Sm])/He Data

Raw (U-Th[Sm])/He data from this study, used to implement thermal models.

Table A2.1. Summary of Analyzed and Unanalyzed Apatite (U-Th)/He Samples from the Northern Fish Creek Vallecito Basin

Location	HW/FW	Sample	Formation/ Unit	Member	Depositional Age	Strat Type	Latitude[1]	Longitude[1]	Source
Fish Creek Wash	HW	13MCSMG31	Arroyo Diablo	-	~4.0-3.5 Ma	C-Suite	32.96359	-116.18833	Cloos, 2014
Fish Creek Wash	HW	13MCSMG30	Olla	-	~4.0-3.5 Ma	L-Suite	32.96358	-116.18783	Cloos, 2014
Fish Creek Wash	HW	13MCSMG29	Arroyo Diablo	-	~4.0 Ma	C-Suite	32.96729	-116.17279	Cloos, 2014
Fish Creek Wash	HW	13MCSMG22	Arroyo Diablo	-	~4.2 Ma	C Suite	32.97219	-116.16756	Cloos, 2014
Fish Creek Wash	HW	13MCSMG21	Deguynos	Yuha	~4.8 Ma	C-Suite	32.9803	-116.14497	Cloos, 2014
Fish Creek Wash	HW	13MCSMG9	Deguynos	Mud Hills[2]	~5.0 Ma	C-Suite	32.98533	-116.12733	Cloos, 2014
Fish Creek Wash	HW	13MCSMG8	Deguynos	Mud Hills[2]	~5.0 Ma	C-Suite	32.98661	-116.12688	Cloos, 2014
Fish Creek Wash	HW	13MCSMG6	Deguynos	Mud Hills	~5.1 Ma	L-Suite	32.99285	-116.13249	Cloos, 2014
Fish Creek Wash	HW	13MCSMG12	Latrania	Wind Caves	5.3-5.2 Ma	C-Suite	32.99259	-116.12993	Cloos, 2014
Fish Creek Wash	HW	13MCSMG13	Latrania	Wind Caves	5.3-5.2 Ma	C-Suite	32.99239	-116.1274	Cloos, 2014
Fish Creek Wash	HW	13MCSMG15	Latrania	Wind Caves	5.3-5.2 Ma	C-Suite	32.9902	-116.11647	Cloos, 2014
Fish Creek Wash	HW	14MCSMG1	Latrania	Wind Caves	~5.3 Ma	C-Suite	32.99257	-116.12396	Cloos, 2014
Fish Creek Wash	HW	14MCSMG3	Latrania	Wind Caves	~5.3 Ma	L-Suite	32.99257	-116.12396	Cloos, 2014
Fish Creek Wash	HW	Y21-047	Latrania	upper mbx[3]	-	L-Suite	32.99524	-116.11681	This Study
Fish Creek Wash	HW	13MCSMG25	Latrania	Lycium	~5.4 Ma	L-Suite	32.99535	-116.11616	Cloos, 2014
Fish Creek Wash	HW	12MCSMG4	Latrania	Lycium	~6.2 Ma	L-Suite	33.00076	-116.11523	Cloos, 2014
Fish Creek Wash	HW	Y21-048	lower mbx[3]	-	~5.5	L-suite	33.00244	-116.11477	This Study
Fish Creek Wash	HW	12MCSMG3	Eleph. T.	-	~6.5 Ma	L-Suite	33.00151	-116.11513	Cloos, 2014
Fish Creek Wash	HW	12MCSMG1	Eleph. T.	-	~8.0 Ma	L-Suite	33.0141	-116.11201	Cloos, 2014
HW west of SMG	HW	Y21-044	Basement	-	-	Source	33.02689	-116.12683	This Study
N of Lycium Wash	HW	Y21-037	mbx[3]	-	~5.5 Ma	L-suite	33.02615	-116.15067	This Study
VM, Alma Wash	FW?	Y20-035	Basement	-	-	Source	33.05789	-116.16106	This Study
VM, Alma Wash	FW	Y21-038	Basement	-	-	Source	33.05826	-116.18604	This Study
VM, Alma Wash	FW	Y21-039	Basement	-	-	Source	33.06154	-116.17724	This Study
VM, Alma Wash	FW	Y21-040	Basement	-	-	Source	33.05968	-116.16784	This Study
VM, NE of Hapaha Flt	FW	Y21-041[4]	Basement	-	-	Source	33.04351	-116.23071	This Study
VM, N. of Eleph. T.	FW?	Y21-043	Basement	-	-	Source	33.07037	-116.14162	This Study
VM, S of NRC	FW	Y21-045	Basement	-	-	Source	33.0333	-116.15595	This Study
VM, S end PVF	FW	Y21-046	Basement	-	-	Source	33.01324	-116.1692	This Study
VM, NE margin VM	FW	Y21-036	Basement	-	-	Source	33.103	-116.1912	This Study
VM, NE margin VM	FW	27-141-1	Basement	-	-	Source	33.101	-116.16	Shirvell, 06; 09

Caption on following page

Caption to Table A2.1

1. Lat. long. errors for samples from this study are 3 m except samples Y21-046 (9m) and Y21-048 (4m). Other studies not reported.
2. Sample collection by Cloos, 2014, This Study, or Shirvell 2006. Sample 27-141-1 analysis reported in Shirvell 2006 and Shirvell et al., 2009
3. Rhythmites
4. Sampled single clast within the megabreccia
5. No apatites found in sample during mineral seperation process

Eleph. T = Elephant Trees, Flt = flat, FW = foot wall of PVF, HW = hanging wall of PVF, mbx = megabreccia, NRC = No Return Canyon, PVF = proto-Vallecito fault, SMG = Split Mountain Gorge, VM = Vallecito Mountains

Table A2.2: Reduced Apatite (U-Th[Sm])/He Data

Sample	Age, Ma	err., Ma	U (ppm)	Th (ppm)	147Sm (ppm)	[U]e	Th/U	He (nmol/g)	mass (ug)	Ft	ESR
12MCSMG-1-1	2.4	0.1	10.1	13.9	15.4	13.4	1.37	0.1	2.23	0.67	45.4
12MCSMG-1-2	16.7	1.0	35.2	14.9	94.9	39.1	0.42	2.5	2.84	0.69	47.7
12MCSMG-1-3	2.4	0.1	31.1	10.1	67.6	33.8	0.32	0.3	1.61	0.64	39.5
12MCSMG-1-4	1.3	0.1	30.9	48.1	45.2	42.2	1.56	0.2	2.91	0.67	46.5
12MCSMG-1-5	18.9	1.1	85.6	43.0	90.2	96.0	0.50	6.4	1.71	0.65	40.9
12MCSMG-1-6	1.8	0.1	24.2	29.1	25.4	31.0	1.21	0.2	1.35	0.60	37.0
12MCSMG-1-7	1.7	0.1	19.3	7.9	47.7	21.4	0.41	0.1	4.33	0.73	55.8
12MCSMG-1-8	12.7	0.8	57.5	36.5	137.2	66.6	0.64	3.2	2.93	0.70	49.2
12MCSMG-3-1	11.1	0.7	57.2	14.9	53.9	60.9	0.26	2.8	5.11	0.75	59.1
12MCSMG-3-2	10.7	0.6	35.8	7.1	30.8	37.6	0.20	1.6	3.71	0.73	54.7
12MCSMG-3-3	25.3	1.5	65.8	44.5	139.1	76.7	0.68	7.9	5.49	0.75	59.9
12MCSMG-3-4	7.2	0.4	58.9	15.3	57.5	62.7	0.26	1.5	1.49	0.63	38.3
12MCSMG-3-5	17.0	1.0	35.5	33.0	149.0	43.8	0.93	2.8	2.82	0.69	48.3
12MCSMG-3-6	29.5	1.8	90.5	23.3	145.3	96.6	0.26	10.5	2.41	0.68	45.4
12MCSMG-3-7	16.3	1.0	41.4	15.4	42.3	45.1	0.37	3.0	4.88	0.75	59.2
13MCSMG-9-1	10.1	0.6	5.4	11.4	98.7	8.5	2.13	0.3	0.87	0.55	33.0
13MCSMG-9-2	27.3	1.6	6.7	30.8	251.2	15.0	4.62	1.2	0.62	0.49	28.6
13MCSMG-9-3	17.1	1.0	3.8	10.1	85.6	6.6	2.65	0.4	0.93	0.55	33.0
13MCSMG-9-4	39.4	2.4	1.9	5.8	51.7	3.5	3.07	0.5	1.44	0.59	36.7
13MCSMG-9-7	45.8	2.7	1.2	5.3	143.6	3.2	4.28	0.5	0.88	0.54	32.3
13MCSMG-15-1	2.5	0.2	47.8	41.7	231.0	58.6	0.87	0.5	1.84	0.66	43.1
13MCSMG-15-2	4.0	0.2	11.3	54.0	90.8	24.2	4.77	0.3	1.77	0.64	42.5
13MCSMG-15-3	20.4	1.2	4.5	7.2	37.7	6.4	1.60	0.5	3.64	0.70	52.1
13MCSMG-15-4	4.6	0.3	4.0	17.1	203.8	8.9	4.32	0.2	2.14	0.66	45.8
13MCSMG-15-5	4.6	0.3	5.0	15.0	133.4	9.1	3.02	0.2	6.12	0.74	60.9
13MCSMG-15-7	14.6	0.9	50.2	50.7	123.1	62.5	1.01	3.7	5.30	0.74	59.8
13MCSMG-21-1	3.4	0.2	8.6	43.4	60.2	18.9	5.03	0.2	2.47	0.67	47.4
13MCSMG-21-2	6.8	0.4	7.1	29.4	211.9	14.9	4.12	0.4	2.61	0.67	47.5
13MCSMG-21-3	3.3	0.2	4.3	11.3	99.2	7.4	2.65	0.1	3.71	0.71	54.4
13MCSMG-21-5	2.8	0.2	3.4	5.8	62.7	5.1	1.68	0.1	3.02	0.70	50.8
13MCSMG-21-6	13.7	0.8	3.3	5.9	71.6	5.0	1.81	0.3	1.92	0.65	44.1

Table A2.2: Reduced Apatite (U-Th[Sm])/He Data Continued

Sample	Age, Ma	err., Ma	U (ppm)	Th (ppm)	147Sm (ppm)	[U]e	Th/U	He (nmol/g)	mass (ug)	Ft	ESR
13MCSMG-22-1	46.9	2.8	44.2	27.9	98.1	51.1	0.63	9.7	4.69	0.74	57.6
13MCSMG-22-2	32.2	1.9	3.2	14.9	121.3	7.3	4.62	1.1	12.84	0.80	81.7
13MCSMG-22-3	26.9	1.6	3.3	16.1	170.5	7.8	4.94	1.0	9.28	0.78	74.2
13MCSMG-22-4	33.7	2.0	1.4	1.9	126.7	2.4	1.39	0.4	8.95	0.77	67.5
13MCSMG-22-6	47.4	2.8	29.9	6.2	81.5	31.7	0.21	6.6	10.73	0.81	76.9
13MCSMG-29-1	4.5	0.3	3.0	7.1	183.6	5.5	2.40	0.1	3.87	0.72	56.1
13MCSMG-29-3	11.3	0.7	3.0	8.1	185.3	5.8	2.70	0.3	5.96	0.75	64.0
13MCSMG-29-4	31.5	1.9	4.9	15.6	151.5	9.2	3.18	1.2	4.88	0.73	59.0
13MCSMG-29-5	25.1	1.5	5.8	18.7	237.2	11.3	3.22	1.1	3.00	0.69	50.0
13MCSMG-30-1	28.8	1.7	37.3	1.5	67.1	38.0	0.04	5.0	15.94	0.84	89.9
13MCSMG-30-3	48.7	2.9	169.0	43.3	94.3	179.4	0.26	34.2	3.72	0.72	52.5
13MCSMG-30-4	61.3	3.7	25.9	12.7	70.4	29.2	0.49	8.2	20.94	0.84	98.0
13MCSMG-30-5	40.2	2.4	50.1	2.5	160.3	51.5	0.05	8.6	6.01	0.77	61.8
13MCSMG-30-6	36.7	2.2	6.6	1.2	54.5	7.2	0.18	1.1	3.68	0.73	54.7
13MCSMG-30-7	46.4	2.8	16.2	3.4	158.4	17.8	0.21	3.6	8.32	0.79	71.2
13MCSMG-31-1	44.5	2.7	25.3	7.8	27.2	27.2	0.31	4.9	5.26	0.75	58.9
13MCSMG-31-2	39.0	2.3	6.2	15.2	55.4	9.9	2.46	1.6	6.74	0.76	65.2
13MCSMG-31-3	48.1	2.9	27.2	12.8	62.4	30.5	0.47	5.9	5.06	0.74	58.5
13MCSMG-31-4	32.6	2.0	1.6	8.0	71.7	3.8	4.95	0.5	7.39	0.74	61.0
13MCSMG-31-5	38.8	2.3	8.1	12.6	130.7	11.7	1.56	1.9	5.44	0.75	62.3
13MCSMG-31-6	48.5	2.9	6.8	24.0	124.7	13.0	3.52	2.5	3.83	0.71	54.3
13MCSMG-31-7	34.8	2.1	42.8	5.2	148.6	44.8	0.12	6.5	5.73	0.76	61.3
14MCSMG-1-1	15.0	0.9	3.1	6.8	119.3	5.3	2.17	0.3	2.36	0.66	45.6
14MCSMG-1-2	1.6	0.1	4.7	32.6	219.4	13.3	6.97	0.1	1.47	0.59	37.2
14MCSMG-1-6	4.3	0.3	10.8	35.2	99.6	19.4	3.26	0.4	11.09	0.79	78.8
14MCSMG-3-1	2.0	0.1	11.0	4.1	40.8	12.2	0.37	0.1	20.86	0.84	93.8
14MCSMG-3-2	5.7	0.3	27.3	9.7	63.2	29.8	0.36	0.7	5.00	0.75	59.1
14MCSMG-3-3	12.0	0.7	27.6	11.0	95.7	30.6	0.40	1.4	2.70	0.68	45.7
14MCSMG-3-4	15.4	0.9	28.5	7.1	69.5	30.5	0.25	1.9	5.46	0.76	60.9
14MCSMG-3-5	6.7	0.4	35.8	11.4	48.4	38.7	0.32	1.0	3.31	0.71	49.9
14MCSMG-3-6	4.8	0.3	25.6	14.9	20.5	29.2	0.58	0.5	2.23	0.68	45.4
14MCSMG-3-7	28.3	1.7	66.7	41.7	95.6	76.7	0.63	8.8	5.30	0.75	60.8

Table A2.2: Reduced Apatite (U-Th[Sm])/He Data Continued

Sample	Age, Ma	err., Ma	U (ppm)	Th (ppm)	147Sm (ppm)	[U]e	Th/U	He (nmol/g)	mass (ug)	Ft	ESR
Y21-037-1	2.3	0.1	20.8	10.4	21.8	23.3	0.50	0.2	2.1	0.67	44.8
Y21-037-2	6.8	0.4	31.0	15.5	37.2	34.8	0.50	0.8	1.2	0.62	37.5
Y21-037-3	3.9	0.2	16.7	11.6	35.5	19.6	0.69	0.3	1.8	0.64	41.2
Y21-037-4	3.3	0.2	22.5	12.6	39.9	25.6	0.56	0.3	1.3	0.63	38.9
Y21-037-5	6.0	0.4	37.5	21.5	41.8	42.7	0.57	0.8	0.8	0.57	32.5
Y21-037-6	3.3	0.2	46.5	26.9	58.3	53.0	0.58	0.4	0.5	0.47	25.4
Y21-047-1	2.8	0.2	82.2	22.6	93.4	87.9	0.28	1.0	3.93	0.73	54.2
Y21-047-2	6.6	0.4	71.6	29.2	70.6	78.7	0.41	2.0	2.79	0.69	47.7
Y21-047-3	9.3	0.6	70.2	16.6	63.0	74.3	0.24	2.3	1.07	0.61	35.6
Y21-047-4	27.4	1.6	122.5	26.8	97.7	129.1	0.22	11.0	0.92	0.58	32.6
Y21-047-5	4.4	0.3	95.1	17.2	70.2	99.4	0.18	1.2	0.64	0.51	27.1
Y21-047-6	15.8	0.9	162.6	26.9	100.2	169.3	0.17	6.2	0.28	0.43	22.5
Y21-047-7	22.3	1.3	90.7	30.7	103.4	98.3	0.34	8.3	3.11	0.69	47.5
Y21-048-1	8.4	0.5	71.9	25.5	113.8	78.3	0.35	2.5	3.1	0.71	51.5
Y21-048-2	24.0	1.4	146.6	54.1	166.0	159.9	0.37	14.9	4.2	0.72	52.0
Y21-048-3	5.1	0.3	51.9	21.7	108.0	57.4	0.42	1.2	3.9	0.73	54.5
Y21-048-4	14.6	0.9	104.4	30.6	105.7	111.9	0.29	5.7	1.7	0.65	40.5
Y21-048-5	10.0	0.6	61.6	19.8	92.3	66.6	0.32	2.1	1.1	0.58	33.2
Y21-043-1	7.7	0.5	16.7	30.7	28.8	23.9	1.84	0.4	0.4	0.42	23.6
Y21-043-2	21.2	1.3	13.2	13.9	20.9	16.5	1.06	0.9	0.5	0.47	26.0
Y21-043-3	16.7	1.0	19.0	16.6	111.7	23.3	0.87	0.9	0.4	0.43	23.7
Y21-043-4	23.7	1.4	11.0	9.4	31.2	13.3	0.86	0.8	0.4	0.46	25.1
Y21-043-5	15.5	0.9	15.0	4.0	84.3	16.4	0.27	0.8	0.7	0.55	30.9
Y21-043-6	31.6	1.9	37.8	24.2	20.5	43.4	0.64	4.2	0.8	0.56	32.4
Y21-044-1	2.7	0.2	12.2	9.6	31.2	14.5	0.79	0.1	2.3	0.67	44.9
Y21-044-2	39.6	2.4	13.7	12.4	35.4	16.7	0.91	2.3	2.1	0.65	41.7
Y21-044-3	3.5	0.2	14.3	10.6	22.8	16.9	0.74	0.2	0.5	0.48	26.3
Y21-044-4	15.5	0.9	9.1	7.5	18.8	10.9	0.83	0.6	1.5	0.62	38.1
Y21-044-5	8.2	0.5	14.0	13.9	51.0	17.5	0.99	0.5	3.2	0.69	48.1

Table A2.2: Reduced Apatite (U-Th[Sm])/He Data Continued

Sample	Age, Ma	err., Ma	U (ppm)	Th (ppm)	147Sm (ppm)	[U]e	Th/U	He (nmol/g)	mass (ug)	Ft	ESR
Y21-036-1	59.6	3.6	18.9	14.9	56.8	22.7	0.79	4.5	1.6	0.62	38.0
Y21-036-2	49.9	3.0	15.9	12.8	50.7	19.1	0.80	3.4	1.9	0.65	42.8
Y21-036-3	48.7	2.9	25.8	19.6	76.9	30.7	0.76	4.2	0.5	0.51	28.4
Y21-036-4	47.8	2.9	14.2	12.6	65.6	17.5	0.89	2.7	1.2	0.60	36.1
Y21-036-5	54.2	3.3	19.5	12.9	46.0	22.7	0.66	4.3	1.7	0.64	40.6
Y21-038-1	33.1	2.0	20.1	22.0	50.4	25.4	1.10	2.5	0.78	0.54	31.0
Y21-038-2	33.4	2.0	17.5	12.5	26.6	20.5	0.71	2.5	1.90	0.66	43.6
Y21-038-3	26.1	1.6	32.8	23.8	48.8	38.5	0.73	2.6	0.46	0.48	26.2
Y21-038-4	32.9	2.0	22.2	23.2	52.6	27.8	1.04	2.6	0.64	0.51	29.0
Y21-038-5	35.5	2.1	20.4	16.4	37.4	24.4	0.81	2.4	0.60	0.52	28.9
Y21-038-6	11.5	0.7	9.2	8.4	17.8	11.2	0.91	0.5	1.89	0.65	41.9
Y21-038-7	25.5	1.5	29.5	19.4	35.7	34.1	0.66	2.8	1.10	0.60	36.2
Y21-038-8	35.8	2.1	32.4	25.6	45.2	38.5	0.79	4.1	0.87	0.55	31.3
Y21-038-9	30.8	1.9	30.8	24.0	37.4	36.5	0.78	3.0	0.60	0.48	26.7
Y21-039-1	29.8	1.8	7.7	5.3	7.0	9.0	0.69	1.0	3.3	0.71	52.3
Y21-039-2	17.0	1.0	21.1	28.5	6.1	27.7	1.35	1.4	0.9	0.56	33.2
Y21-039-3	17.9	1.1	7.9	6.0	11.5	9.4	0.76	0.6	3.0	0.68	46.2
Y21-039-4	21.9	1.3	7.0	6.3	14.0	8.5	0.90	0.8	11.1	0.79	75.0
Y21-039-7	21.4	1.3	33.6	22.9	38.1	39.0	0.68	2.1	0.4	0.47	26.0
Y21-039-6	24.6	1.5	15.1	13.1	25.2	18.2	0.87	1.3	0.7	0.52	29.5
Y21-040-1	50.5	3.0	25.6	12.8	28.2	28.7	0.50	5.5	2.6	0.70	48.7
Y21-040-2	8.7	0.5	21.8	13.4	5457.0	52.2	0.61	2.1	1.8	0.64	40.5
Y21-040-3	24.3	1.5	38.5	22.4	135.9	44.3	0.58	3.2	0.8	0.55	31.1
Y21-040-4	29.7	1.8	23.3	16.8	59.1	27.4	0.72	2.6	0.9	0.58	33.7
Y21-040-5	19.9	1.2	28.0	14.4	35.5	31.5	0.51	2.6	5.3	0.76	62.3
Y21-040-7	18.8	1.1	28.9	16.1	44.5	32.8	0.56	1.6	0.8	0.49	27.0
Y21-035-1	64.8	3.9	113.4	45.1	47.6	124.0	0.40	22.3	0.5	0.51	28.1
Y21-035-3	34.0	2.0	36.9	19.2	24.0	41.4	0.52	4.9	1.7	0.64	40.1
Y21-035-4	28.2	1.7	36.4	20.3	37.0	41.2	0.56	4.3	2.3	0.67	45.3
Y21-035-5	24.7	1.5	30.3	18.9	28.2	34.7	0.62	2.9	1.6	0.63	39.5
Y21-035-6	40.0	2.4	32.7	17.7	30.9	37.0	0.54	4.2	0.7	0.53	29.4
Y21-035-7	28.8	1.7	57.6	36.7	35.0	66.2	0.64	5.1	0.5	0.49	27.0

Table A2.2: Reduced Apatite (U-Th[Sm])/He Data Continued

Sample	Age, Ma	err., Ma	U (ppm)	Th (ppm)	147Sm (ppm)	[U]e	Th/U	He (nmol/g)	mass (ug)	Ft	ESR
Y21-045-1	17.4	1.0	16.5	11.7	20.5	19.3	0.71	1.2	2.2	0.67	44.5
Y21-045-2	18.7	1.1	14.3	10.3	18.9	16.7	0.72	0.9	0.6	0.50	28.0
Y21-045-3	28.5	1.7	15.5	9.4	8.8	17.7	0.60	1.4	0.6	0.53	29.4
Y21-045-4	17.8	1.1	12.3	10.1	21.5	14.7	0.83	0.8	0.8	0.54	31.1
Y21-045-5	7.5	0.5	11.8	9.0	20.0	14.0	0.76	0.3	1.1	0.59	35.3
Y21-045-6	18.1	1.1	8.2	7.1	10.9	9.9	0.86	0.5	0.5	0.50	27.7
Y21-046-1	9.5	0.6	46.8	16.4	53.6	50.8	0.35	1.4	0.6	0.54	29.7
Y21-046-2	19.2	1.2	47.0	16.8	35.1	51.0	0.36	3.2	1.1	0.60	34.8
Y21-046-3	17.6	1.1	64.3	22.7	66.9	69.9	0.35	4.4	2.1	0.67	43.5
Y21-046-4	14.6	0.9	38.0	20.3	77.7	43.1	0.53	2.1	1.6	0.62	37.5
Y21-046-5	12.4	0.7	50.2	19.7	66.3	55.1	0.39	2.6	2.8	0.70	48.6
Y21-046-6	19.0	1.1	51.0	19.4	63.3	55.7	0.38	3.7	2.3	0.65	41.3

All samples analyzed are apatite

Samples beingnning with Y were collected for this study, other samples collected by Cloos, 2014 and analysed for this study

Table A2.3: Raw Apatite (U-Th[Sm])/He Data

Aliquot	mineral	mass, ug	UFt	ThFt	He, nmol	err., %	238U/ 235U	err., %	232Th/2 30Th	err., %	147Sm/ 149Sm	err., %	Mean L, um	Mean W, um	ESR, um
14MCSMG-3-1	apatite	20.9	0.843	0.821	0.00000	0.93998	0.0843	0.33	0.2854	0.38	0.0185	0.23	322.33	179.27	93.82
14MCSMG-3-2	apatite	5.0	0.757	0.724	0.00000	0.60577	0.0500	0.41	0.2154	0.32	0.0093	0.60	185.84	115.57	59.13
14MCSMG-3-3	apatite	2.7	0.693	0.652	0.00000	0.72369	0.0274	0.70	0.1784	0.31	0.0083	0.36	190.23	83.90	45.75
14MCSMG-3-4	apatite	5.5	0.764	0.731	0.00001	0.31786	0.0571	0.46	0.1964	0.28	0.0104	0.19	190.92	119.18	60.93
14MCSMG-3-5	apatite	3.3	0.716	0.678	0.00000	0.56481	0.0435	0.20	0.1945	0.26	0.0066	0.35	188.35	93.42	49.94
14MCSMG-3-6	apatite	2.2	0.691	0.650	0.00000	0.78342	0.0211	0.36	0.1854	0.34	0.0046	0.40	138.03	89.60	45.42
14MCSMG-3-7	apatite	5.3	0.763	0.731	0.00005	0.23593	0.1292	0.75	0.5501	0.31	0.0126	0.33	181.54	120.42	60.75
14MCSMG-1-1	apatite	2.4	0.692	0.651	0.00000	1.30815	0.0029	0.62	0.1521	0.51	0.0087	0.20	151.81	87.80	45.60
14MCSMG-1-2	apatite	1.5	0.631	0.583	0.00000	3.22004	0.0027	0.68	0.2136	0.31	0.0094	0.33	156.95	68.10	37.23
14MCSMG-1-6	apatite	11.1	0.815	0.788	0.00000	0.69466	0.0439	0.55	0.8781	0.22	0.0228	0.24	210.64	161.73	78.82
13MCSMG-9-1	apatite	0.9	0.590	0.538	0.00000	1.62987	0.0019	7.11	0.1402	0.43	0.0053	0.32	103.62	64.55	33.01
13MCSMG-9-2	apatite	0.6	0.536	0.480	0.00000	2.09460	0.0017	4.39	0.1578	0.48	0.0065	0.29	106.44	53.59	28.57
13MCSMG-9-3	apatite	0.9	0.590	0.538	0.00000	1.98687	0.0015	2.03	0.1393	0.50	0.0052	0.53	119.98	62.21	32.99
13MCSMG-9-4	apatite	1.4	0.626	0.578	0.00000	1.89376	0.0012	1.21	0.1373	0.47	0.0051	0.11	159.92	66.81	36.74
13MCSMG-9-7	apatite	0.9	0.581	0.529	0.00000	1.01461	0.0006	7.67	0.1301	0.19	0.0060	0.28	118.11	60.72	32.25
13MCSMG-31-1	apatite	5.3	0.756	0.723	0.00003	0.13653	0.0494	0.06	0.2073	0.27	0.0064	0.72	210.06	111.47	58.86
13MCSMG-31-2	apatite	6.7	0.778	0.748	0.00001	0.29464	0.0158	0.31	0.3271	2.27	0.0104	0.41	206.54	127.29	65.25
13MCSMG-31-3	apatite	5.1	0.755	0.721	0.00003	0.13773	0.0511	0.14	0.2534	0.20	0.0094	0.08	201.68	111.60	58.46
13MCSMG-31-4	apatite	7.4	0.764	0.732	0.00000	0.22175	0.0049	0.58	0.2427	0.11	0.0131	0.30	315.92	107.82	61.00
13MCSMG-31-5	apatite	5.4	0.769	0.737	0.00001	0.19578	0.0167	0.51	0.2612	0.37	0.0162	0.26	162.01	129.08	62.32
13MCSMG-31-6	apatite	3.8	0.737	0.702	0.00001	0.22971	0.0101	0.49	0.3067	0.29	0.0122	0.23	165.95	107.06	54.34
13MCSMG-31-7	apatite	5.7	0.765	0.733	0.00004	0.16054	0.0907	0.48	0.1854	0.50	0.0186	0.10	203.49	118.24	61.35
13MCSMG-30-1	apatite	15.9	0.836	0.813	0.00008	0.12317	0.2190	0.92	0.1740	0.61	0.0223	0.19	214.16	192.29	89.91
13MCSMG-30-3	apatite	3.7	0.729	0.692	0.00013	0.13907	0.2311	0.87	0.4420	0.26	0.0100	0.24	186.70	99.43	52.47
13MCSMG-30-4	apatite	20.9	0.849	0.828	0.00017	0.09796	0.1997	0.33	0.6491	0.26	0.0291	0.11	247.78	204.88	97.97
13MCSMG-30-5	apatite	6.0	0.767	0.735	0.00005	0.12100	0.1111	0.21	0.1560	0.55	0.0205	0.21	216.05	117.51	61.76
13MCSMG-30-6	apatite	3.7	0.739	0.704	0.00000	0.38454	0.0095	0.88	0.1351	0.40	0.0074	0.19	142.71	113.19	54.71
13MCSMG-30-7	apatite	8.3	0.796	0.767	0.00003	0.10852	0.0502	0.16	0.1826	0.59	0.0265	0.19	199.53	143.92	71.22
13MCSMG-29-1	apatite	3.9	0.745	0.710	0.00000	1.50905	0.0047	1.44	0.1803	0.31	0.0162	0.36	134.70	119.46	56.05
13MCSMG-29-3	apatite	6.0	0.774	0.743	0.00000	0.29966	0.0071	3.88	0.2214	2.73	0.0229	1.20	173.17	130.77	64.00
13MCSMG-29-4	apatite	4.9	0.757	0.723	0.00001	0.28515	0.0093	0.94	0.2758	0.68	0.0167	0.60	177.99	116.75	59.05
13MCSMG-29-5	apatite	3.0	0.716	0.678	0.00000	0.55464	0.0069	0.74	0.2363	0.37	0.0162	0.23	154.74	98.06	49.97

Table A2.3: Raw Apatite (U-Th[Sm])/He Data Continued

Aliquot	mineral	mass, ug	UFt	ThFt	He, nmol	err.,%	238U/ 235U	err.,%	232Th/2 30Th	err.,%	147Sm/ 149Sm	err.,%	Mean L, um	Mean W, um	ESR, um
13MCSMG-22-1	apatite	4.7	0.751	0.717	0.00005	0.14653	0.0767	0.25	0.3830	0.25	0.0119	0.22	186.59	111.74	57.62
13MCSMG-22-2	apatite	12.8	0.821	0.795	0.00001	0.36440	0.0157	1.94	0.5007	0.40	0.0305	0.34	241.76	162.41	81.70
13MCSMG-22-3	apatite	9.3	0.804	0.776	0.00001	0.22059	0.0116	1.18	0.4183	0.65	0.0309	0.28	199.18	152.11	74.23
13MCSMG-22-4	apatite	9.0	0.785	0.756	0.00000	0.51450	0.0050	1.12	0.1600	1.12	0.0234	0.35	295.76	122.62	67.51
13MCSMG-22-6	apatite	10.7	0.810	0.783	0.00007	0.13449	0.1183	0.68	0.2564	0.49	0.0190	0.20	229.17	152.49	76.88
13MCSMG-21-1	apatite	2.5	0.703	0.663	0.00000	1.80936	0.0080	3.87	0.3295	0.44	0.0064	1.05	134.81	95.45	47.44
13MCSMG-21-2	apatite	2.6	0.703	0.663	0.00000	1.40403	0.0070	0.87	0.2698	0.62	0.0134	0.38	151.09	92.63	47.53
13MCSMG-21-3	apatite	3.7	0.738	0.702	0.00000	2.92722	0.0060	0.32	0.2025	0.63	0.0102	0.18	153.08	109.69	54.36
13MCSMG-21-5	apatite	3.0	0.721	0.683	0.00000	2.75846	0.0040	0.45	0.1549	0.54	0.0071	0.48	141.00	103.06	50.84
13MCSMG-21-6	apatite	1.9	0.682	0.640	0.00000	2.32140	0.0025	0.70	0.1431	0.42	0.0062	0.24	114.18	91.36	44.06
13MCSMG-15-1	apatite	1.8	0.676	0.633	0.00000	1.63380	0.0324	0.35	0.2702	0.22	0.0112	0.11	120.27	87.22	43.10
13MCSMG-15-2	apatite	1.8	0.672	0.628	0.00000	4.86182	0.0075	1.80	0.3060	0.33	0.0066	0.28	118.33	86.11	42.52
13MCSMG-15-3	apatite	3.6	0.727	0.690	0.00000	0.87285	0.0062	1.12	0.1721	0.50	0.0062	0.26	185.99	98.61	52.08
13MCSMG-15-4	apatite	2.1	0.693	0.652	0.00000	1.38773	0.0033	0.77	0.1921	0.43	0.0114	0.51	117.84	95.08	45.76
13MCSMG-15-5	apatite	6.1	0.764	0.731	0.00000	0.80399	0.0113	0.62	0.2990	0.49	0.0179	0.48	238.05	112.99	60.86
13MCSMG-15-7	apatite	5.3	0.760	0.727	0.00002	0.42771	0.0973	0.41	0.6422	0.30	0.0151	0.38	197.63	115.38	59.81
12MCSMG-3-1	apatite	5.1	0.757	0.724	0.00001	0.38060	0.1068	0.47	0.2682	0.55	0.0086	0.31	194.93	114.05	59.09
12MCSMG-3-2	apatite	3.7	0.739	0.703	0.00001	0.63425	0.0488	0.75	0.1725	0.94	0.0058	0.06	146.73	112.08	54.69
12MCSMG-3-3	apatite	5.5	0.760	0.727	0.00004	0.20298	0.1320	0.30	0.5945	0.55	0.0170	0.37	209.57	114.02	59.92
12MCSMG-3-4	apatite	1.5	0.640	0.593	0.00000	0.97138	0.0323	0.78	0.1652	0.92	0.0053	0.49	144.55	71.62	38.29
12MCSMG-3-5	apatite	2.8	0.708	0.668	0.00001	0.52443	0.0367	0.62	0.3016	1.90	0.0111	0.55	162.58	92.78	48.31
12MCSMG-3-6	apatite	2.4	0.690	0.649	0.00003	0.24078	0.0799	0.21	0.2299	0.83	0.0099	0.44	162.65	85.81	45.36
12MCSMG-3-7	apatite	4.9	0.757	0.724	0.00001	0.52619	0.0739	0.27	0.2669	0.47	0.0074	0.05	175.40	117.51	59.15
12MCSMG-1-1	apatite	2.2	0.691	0.649	0.00000	1.89132	0.0088	0.44	0.1872	0.56	0.0045	0.33	137.87	89.62	45.42
12MCSMG-1-2	apatite	2.8	0.704	0.664	0.00001	0.33508	0.0373	0.31	0.2097	0.47	0.0086	0.18	175.27	89.71	47.69
12MCSMG-1-3	apatite	1.6	0.649	0.604	0.00000	1.61447	0.0189	0.58	0.1584	0.77	0.0058	0.21	144.58	74.33	39.48
12MCSMG-1-4	apatite	2.9	0.697	0.657	0.00000	1.09037	0.0336	0.14	0.4011	0.26	0.0062	0.15	202.10	84.60	46.51
12MCSMG-1-5	apatite	1.7	0.660	0.616	0.00001	0.21262	0.0545	0.29	0.2710	0.93	0.0066	0.30	138.26	78.48	40.91
12MCSMG-1-6	apatite	1.4	0.629	0.581	0.00000	2.09286	0.0125	5.46	0.2037	4.50	0.0045	2.04	140.31	69.14	37.00
12MCSMG-1-7	apatite	4.3	0.744	0.709	0.00000	1.53291	0.0312	0.24	0.1938	0.55	0.0075	0.32	187.18	107.15	55.76
12MCSMG-1-8	apatite	2.9	0.712	0.673	0.00001	0.24334	0.0625	0.36	0.3365	0.74	0.0109	0.29	161.60	94.96	49.16

Table A2.3: Raw Apatite (U-Th[Sm])/He Data Continued

Aliquot	mineral	mass, ug	UFt	ThFt	He, nmol	err.,%	238U/ 235U	err.,%	232Th/2 30Th	err.,%	147Sm/ 149Sm	err.,%	Mean L, um	Mean W, um	ESR, um
Y21-048-1	apatite	3.13	0.724	0.687	0.00001	0.18568	0.0792	0.94	0.2768	1.63	0.0101	0.49	142.71	104.45	51.51
Y21-048-2	apatite	4.21	0.727	0.689	0.00006	0.14210	0.2166	0.88	0.5554	1.68	0.0160	0.77	238.39	93.68	51.99
Y21-048-3	apatite	3.94	0.738	0.702	0.00000	0.16657	0.0720	0.80	0.2875	1.62	0.0113	0.77	174.24	105.97	54.47
Y21-048-4	apatite	1.68	0.657	0.612	0.00001	0.25944	0.0618	1.01	0.2234	2.19	0.0070	0.21	139.11	77.37	40.49
Y21-048-5	apatite	1.09	0.592	0.541	0.00000	0.32565	0.0241	0.97	0.1670	0.89	0.0057	0.30	150.93	59.97	33.23
Y21-047-1	apatite	3.93	0.737	0.701	0.00000	0.24437	0.1137	0.55	0.2947	0.90	0.0104	0.48	178.60	104.51	54.15
Y21-047-2	apatite	2.79	0.704	0.665	0.00001	0.23317	0.0704	0.83	0.2803	0.74	0.0074	0.55	169.04	90.58	47.74
Y21-047-3	apatite	1.07	0.616	0.567	0.00000	0.45014	0.0266	0.71	0.1597	0.48	0.0051	0.29	107.03	70.43	35.59
Y21-047-4	apatite	0.92	0.585	0.533	0.00001	0.17790	0.0398	0.64	0.1729	0.94	0.0055	0.23	123.48	60.89	32.58
Y21-047-5	apatite	0.64	0.516	0.458	0.00000	0.79619	0.0216	0.79	0.1470	0.96	0.0047	0.23	138.27	48.09	27.14
Y21-047-6	apatite	0.28	0.436	0.372	0.00000	0.33614	0.0162	0.98	0.1404	1.16	0.0044	0.45	75.10	43.20	22.46
Y21-047-7	apatite	3.11	0.703	0.663	0.00003	0.14535	0.0993	1.27	0.3070	0.96	0.0096	0.58	207.16	86.36	47.50
Y21-046-1	apatite	0.64	0.551	0.495	0.00000	0.61647	0.0108	1.47	0.1463	1.37	0.0045	0.58	94.59	57.77	29.67
Y21-046-2	apatite	1.14	0.608	0.559	0.00000	0.42897	0.0191	1.79	0.1625	1.46	0.0046	0.46	134.62	64.82	34.83
Y21-046-3	apatite	2.14	0.679	0.636	0.00001	0.22607	0.0486	0.98	0.2179	1.63	0.0064	0.29	157.55	82.13	43.51
Y21-046-4	apatite	1.62	0.633	0.585	0.00000	0.21748	0.0219	1.19	0.1883	2.01	0.0061	0.45	178.02	67.17	37.49
Y21-046-5	apatite	2.85	0.709	0.670	0.00001	0.24708	0.0505	1.40	0.2322	1.84	0.0072	0.51	161.31	93.75	48.64
Y21-046-6	apatite	2.26	0.663	0.619	0.00001	0.23920	0.0407	1.24	0.2090	1.54	0.0064	0.29	208.78	73.29	41.31
Y21-045-1	apatite	2.18	0.685	0.643	0.00000	0.36117	0.0130	0.95	0.1745	1.41	0.0047	0.74	147.59	85.66	44.45
Y21-045-2	apatite	0.59	0.528	0.470	0.00000	0.99332	0.0032	2.17	0.1374	1.00	0.0041	0.46	108.24	52.00	27.95
Y21-045-3	apatite	0.63	0.547	0.492	0.00000	0.61753	0.0037	0.94	0.1372	0.42	0.0040	0.59	98.47	56.56	29.41
Y21-045-4	apatite	0.78	0.568	0.515	0.00000	0.84465	0.0036	0.80	0.1409	0.98	0.0042	0.89	111.21	58.90	31.11
Y21-045-5	apatite	1.12	0.613	0.564	0.00000	0.89673	0.0049	1.08	0.1450	0.81	0.0043	0.42	121.65	67.50	35.34
Y21-045-6	apatite	0.51	0.524	0.466	0.00000	0.98430	0.0017	1.65	0.1328	0.60	0.0040	0.75	86.65	54.17	27.68
Y21-044-1	apatite	2.33	0.687	0.646	0.00000	0.76384	0.0103	0.54	0.1685	0.59	0.0052	0.41	159.93	85.06	44.90
Y21-044-2	apatite	2.05	0.666	0.622	0.00000	0.34106	0.0102	0.67	0.1743	1.32	0.0052	0.52	174.70	76.38	41.70
Y21-044-3	apatite	0.49	0.502	0.443	0.00000	1.81124	0.0027	2.50	0.1358	1.36	0.0041	0.58	102.08	48.80	26.25
Y21-044-4	apatite	1.49	0.638	0.591	0.00000	0.60200	0.0050	0.39	0.1472	0.90	0.0044	0.33	147.21	70.84	38.07
Y21-044-5	apatite	3.18	0.707	0.667	0.00000	0.42182	0.0161	0.82	0.2103	1.14	0.0068	0.49	204.32	87.91	48.12

Table A2.3: Raw Apatite (U-Th[Sm])/He Data Continued

Aliquot	mineral	mass, ug	UFt	ThFt	He, nmol	err.,%	238U/ 235U	err.,%	232Th/2 30Th	err.,%	147Sm/ 149Sm	err.,%	Mean L, um	Mean W, um	ESR, um
Y21-043-1	apatite	0.39	0.457	0.395	0.00000	1.43991	0.0025	3.00	0.1485	5.79	0.0041	1.96	105.71	42.65	23.58
Y21-043-2	apatite	0.53	0.499	0.440	0.00000	0.82676	0.0027	1.62	0.1400	1.01	0.0041	0.67	120.49	46.87	26.05
Y21-043-3	apatite	0.40	0.459	0.397	0.00000	0.92377	0.0029	3.37	0.1385	1.45	0.0047	0.37	109.58	42.57	23.66
Y21-043-4	apatite	0.36	0.483	0.423	0.00000	1.24303	0.0016	0.56	0.1323	0.50	0.0041	0.36	66.97	51.48	25.08
Y21-043-5	apatite	0.73	0.566	0.512	0.00000	0.63642	0.0041	1.56	0.1315	1.12	0.0050	0.73	101.78	59.63	30.89
Y21-043-6	apatite	0.82	0.583	0.531	0.00000	0.29275	0.0112	1.11	0.1635	0.81	0.0042	0.37	100.70	63.50	32.39
Y21-040-1	apatite	2.64	0.710	0.671	0.00001	0.11395	0.0240	0.75	0.1903	1.73	0.0052	1.63	133.64	99.05	48.69
Y21-040-2	apatite	1.84	0.657	0.612	0.00000	0.27242	0.0144	1.20	0.1730	1.69	0.1551	0.54	163.30	74.71	40.49
Y21-040-3	apatite	0.8	0.568	0.514	0.00000	0.34645	0.0111	1.03	0.1602	1.98	0.0058	23.04	117.87	58.05	31.07
Y21-040-4	apatite	0.87	0.597	0.546	0.00000	0.29266	0.0074	1.87	0.1540	0.42	0.0048	6.85	92.91	68.34	33.66
Y21-040-5	apatite	5.33	0.769	0.737	0.00001	0.15792	0.0527	1.80	0.2706	1.35	0.0072	1.42	151.70	132.13	62.31
Y21-040-7	apatite	0.77	0.514	0.456	0.00000	0.54131	0.0081	0.56	0.1499	1.71	0.0045	0.56	179.28	46.30	27.04
Y21-039-1	apatite	3.26	0.728	0.691	0.00000	0.27779	0.0091	1.57	0.1592	0.75	0.0043	0.53	140.71	107.19	52.34
Y21-039-2	apatite	0.93	0.591	0.540	0.00000	0.44815	0.0072	0.73	0.1764	1.00	0.0040	0.40	115.76	63.11	33.16
Y21-039-3	apatite	2.98	0.696	0.655	0.00000	0.31337	0.0086	1.95	0.1604	1.19	0.0045	0.36	213.47	83.20	46.23
Y21-039-4	apatite	11.06	0.806	0.778	0.00001	0.17102	0.0273	1.32	0.2576	0.64	0.0066	0.69	276.17	141.02	74.99
Y21-039-6	apatite	0.68	0.548	0.493	0.00000	0.67804	0.0039	8.86	0.1433	0.58	0.0042	0.85	111.22	55.18	29.50
Y21-039-7	apatite	0.45	0.498	0.438	0.00000	0.00925	0.0056	1.20	0.1459	1.84	0.0042	0.91	91.70	49.29	25.96
Y21-038-1	apatite	0.78	0.567	0.514	0.00000	0.39780	0.0057	0.60	0.1586	0.41	0.0046	0.39	112.82	58.51	31.03
Y21-038-2	apatite	1.9	0.679	0.637	0.00000	0.24205	0.0119	0.65	0.1711	0.59	0.0048	0.22	120.00	88.65	43.62
Y21-038-3	apatite	0.46	0.501	0.442	0.00000	0.40252	0.0055	14.43	0.1469	1.34	0.0043	0.55	90.76	49.92	26.18
Y21-038-4	apatite	0.64	0.542	0.486	0.00000	0.41282	0.0052	1.47	0.1542	0.48	0.0045	0.86	107.71	54.46	29.01
Y21-038-5	apatite	0.6	0.541	0.485	0.00000	0.32482	0.0045	1.05	0.1448	0.26	0.0043	0.37	96.74	55.68	28.94
Y21-038-6	apatite	1.89	0.668	0.624	0.00000	0.36424	0.0063	0.27	0.1562	0.47	0.0045	0.36	149.10	79.45	41.92
Y21-038-7	apatite	1.1	0.621	0.573	0.00000	0.37596	0.0116	1.06	0.1666	0.21	0.0046	0.53	103.18	72.73	36.19
Y21-038-8	apatite	0.87	0.570	0.517	0.00000	0.28323	0.0101	0.48	0.1684	0.76	0.0046	0.21	132.30	57.15	31.26
Y21-038-9	apatite	0.6	0.509	0.451	0.00000	0.38729	0.0067	0.61	0.1534	0.56	0.0043	0.34	130.36	47.63	26.70
Y21-037-1	apatite	2.1	0.687	0.645	0.00000	0.96755	0.0156	1.32	0.1677	0.52	0.0047	0.95	130.82	89.28	44.75
Y21-037-2	apatite	1.23	0.633	0.585	0.00000	0.56140	0.0137	0.67	0.1623	1.89	0.0047	0.60	109.42	74.79	37.48
Y21-037-3	apatite	1.77	0.662	0.618	0.00000	0.76141	0.0107	1.90	0.1652	0.81	0.0050	0.86	142.63	78.54	41.18
Y21-037-4	apatite	1.29	0.644	0.598	0.00000	1.06850	0.0105	0.60	0.1571	1.56	0.0048	0.55	92.32	83.20	38.86
Y21-037-5	apatite	0.82	0.584	0.532	0.00000	0.60563	0.0111	1.21	0.1597	1.02	0.0045	0.40	98.67	64.18	32.52
Y21-037-6	apatite	0.49	0.488	0.428	0.00000	0.98668	0.0083	1.48	0.1513	1.71	0.0044	0.42	117.95	45.56	25.35

Table A2.3: Raw Apatite (U-Th[Sm])/He Data Continued

Aliquot	mineral	mass, ug	UFt	ThFt	He, nmol	err.,%	238U/ 235U	err.,%	232Th/2 30Th	err.,%	147Sm/ 149Sm	err.,%	Mean L, um	Mean W, um	ESR, um
Y21-036-1	apatite	1.61	0.637	0.590	0.00001	0.24852	0.0110	0.68	0.1717	2.02	0.0055	0.57	168.18	68.87	37.99
Y21-036-2	apatite	1.92	0.674	0.631	0.00001	1.35490	0.0110	1.73	0.1726	1.07	0.0056	0.56	137.32	83.29	42.84
Y21-036-3	apatite	0.52	0.534	0.477	0.00000	0.27266	0.0050	1.51	0.1457	1.44	0.0046	0.74	78.33	57.66	28.39
Y21-036-4	apatite	1.22	0.620	0.572	0.00000	0.28280	0.0064	0.60	0.1555	0.87	0.0053	0.26	131.25	68.03	36.08
Y21-036-5	apatite	1.74	0.658	0.613	0.00001	0.21615	0.0122	1.53	0.1688	1.05	0.0053	0.35	147.69	76.48	40.57
Y21-035-1	apatite	0.48	0.529	0.472	0.00001	0.18734	0.0194	1.08	0.1673	3.53	0.0043	0.39	64.96	60.76	28.08
Y21-035-3	apatite	1.67	0.654	0.609	0.00001	0.21618	0.0219	1.30	0.1870	1.20	0.0046	0.99	143.60	75.90	40.11
Y21-035-4	apatite	2.32	0.690	0.648	0.00001	0.23201	0.0299	1.28	0.2153	1.95	0.0054	0.76	152.07	86.97	45.27
Y21-035-5	apatite	1.62	0.650	0.604	0.00000	0.26222	0.0175	1.24	0.1841	1.01	0.0047	0.90	145.55	74.38	39.55
Y21-035-6	apatite	0.74	0.547	0.491	0.00000	0.23077	0.0088	1.93	0.1511	1.54	0.0043	0.38	128.93	53.34	29.38
Y21-035-7	apatite	0.49	0.514	0.456	0.00000	0.40148	0.0102	0.86	0.1604	2.17	0.0042	0.86	89.34	52.12	27.02

1. Spike P4 100 ul
2. Spike NewNormal4 1000 ul

Samples beingnning with Y were collected for this study, other samples collected by Cloos, 2014 and analysed for this study

CHAPTER 3

Effects of sedimentation on pore-pressure conditions within the Salton Trough

ABSTRACT

Rapid sedimentation and burial of saturated, porous sediment can lead to the development of fluid overpressures at depth as sediments compact and permeability is reduced. Such high pore fluid pressure likely exerts a regional control on fault behavior and promotes fault creep at shallow depths. The Fish Creek Vallecito basin (FCVB) on the western margin of the Salton Trough provides an exposure of rocks analogous to those at depth along the San Andreas fault system in the Salton Trough. Both locations experienced rapid sedimentation from the Colorado River delta. This study uses a one-dimensional model of basin deposition and compaction to test for overpressure conditions in this area using the exposure of rocks in the FCVB as a proxy for those at depth in the Salton Trough. The model results show the importance of both rapid sedimentation and the presence of caprock layers for the accumulation and maintenance of overpressure. This overpressure may also promote earthquake triggering in addition to regional fault creep.

INTRODUCTION

Pore-pressure is a first-order control on fault stress conditions and earthquake triggering (Brodsky and Prejan, 2005). High heat flow and overpressure conditions due to rapid sedimentation are hypothesized to affect fault behavior within the Salton Trough by promoting fault creep and earthquake swarms (Harris, 2017). To date, however, there has been little work in southern California on the geologic conditions that control pore-pressure at seismogenic depths outside of the narrow (meter-scale) fault zone (Faulkner and Rutter, 2001). Overpressure (pore-pressure in excess of hydrostatic) is commonly encountered in sedimentary basins, where low-permeability sediments and compaction together can reduce pore volume at depth (Bethke and Corbet, 1988; Behrmann et al., 2006) and drive pressure up to the lithostatic limit (the weight of the saturated rock column). This reduces the normal stress on faults, allowing for slip under low shear-stress conditions (Hubbert and Rubey, 1959), promoting fault creep over stick slip behavior (Harris, 2017). Modeling of actively subsiding and compacting basin sediments shows that sedimentation further contributes to excess pore pressures by steadily increasing the load on rocks and hosted fluids (Bethke and Corbet, 1988). Even a modest rate of sedimentation can sustain excess pore pressure within low-permeability strata or beneath a low-permeability caprock. This pore-pressure enhancement also applies to low-permeability basement rocks below a sedimentary basin, potentially affecting seismogenic faulting within the basement.

Seismicity in the Salton Trough has important implications for geologic hazards in southern California, including the southern terminus of the San Andreas fault, the only portion of the San Andreas fault without a historical rupture (Brodsky, 2006; Brodsky and Lajoie, 2013;

Ross et al., 2019). The region is seismically active (Ross et al., 2019), and several faults in this region creep within the uppermost crust but are locked at depth (Harris, 2017). As an active transtensional rift, high heat flow and overpressure conditions due to rapid sedimentation likely affect fault behavior within the Salton Trough, but direct observations at seismogenic depth are lacking. Elsewhere in California, drilling projects like SAFOD (San Andreas Fault Observatory at Depth) (e.g. Holdsworth et al., 2011; Lockner et al., 2011; Gratier et al., 2011; Warr et al., 2014) and at Cajon Pass (Zoback et al., 1987; Zoback and Lachenbruch, 1992) provide one of the few ways to directly measure and sample the rocks at seismogenic depths in active fault zones. Alternatively, exhumed fault zones and surrounding rocks may be studied to infer seismogenic conditions at depth, but there are few examples of exhumed fault zones that can be clearly tied to present crustal conditions.

The Salton Trough region contains active geothermal areas, which are at heightened risk of triggered and induced seismicity due to regional tectonic and anthropogenic earthquakes, respectively (Brodsky, 2006; Goebel et al., 2015). Anthropogenic and natural fluid-mediated effects on seismicity associated with geothermal energy are of direct societal concern for earthquake forecasting and hazards. For example, fluid injection at the Salton Sea Geothermal Field has been correlated to seismicity rates, and there is concern that activation of faults within the Brawley Seismic Zone could trigger a major earthquake on the nearby southern San Andreas fault (Brodsky and Lajoie, 2013) or other major faults tens of kilometers away due to far-reaching poro-elastic effects (Goebel and Brodsky, 2018). Natural and anthropogenic lake loading could also trigger major San Andreas fault earthquakes (Luttrell et al., 2007; Brothers et al., 2011; Hill et al., 2023). Naturally occurring fluid-pressure enabled fault creep events are

proposed to trigger seismic swarms in the Salton Trough region (Chen and Shearer, 2011; Lohman and McGuire, 2007). Understanding the natural, in-situ pore-pressure conditions at seismogenic depth is essential to model these processes properly.

The exceptional extent and rate of sedimentation across the Salton Trough results from far-traveled sediment delivered by the Colorado River. Regional, long-term (million-year) sedimentation rates within the Salton Trough exceed 2 mm/yr (>10 km of sediment within the past 5 Myr; Fuis et al., 1984), and within the basin, axis sedimentation has been documented to exceed 20 mm/yr adjacent to the Brawley seismic zone (Brothers et al., 2009). The Salton Trough is also the site of widespread shallow fault creep and earthquake swarm activity, both of which have been attributed to excess pore-pressure conditions and the migration of pore-fluids (e.g., Harris, 2017; Lohman and McGuire, 2007; Lindsey et al., 2014). These studies consider, but do not test, the possibility of hydraulic diffusion of elevated pore pressure deep into the sediment column. Here, I model sedimentation, compaction, and pore-pressure evolution within the Salton Trough based on natural exposures of basin strata from the Fish Creek Vallecito basin and from borehole records from the Salton Trough to construct a model of basin pore-pressure evolution. I show that while the rapid sedimentation rate within the Salton Trough does promote overpressure in fine-grained sandy strata, the presence of less permeable shale and mudstone caprock units is essential for maximizing that overpressure and maintaining it over time.

BACKGROUND

The Fish Creek Vallecito basin (FCVB), a subbasin of the Salton Trough, provides an unusually well-exposed sedimentary record of the late Cenozoic northern Gulf of California rift (Figure 3.1). This sedimentary section contains both locally sourced sediment and sediment delivered by the Colorado River and is analogous to the sedimentary section at depth in the modern Salton Trough. In prior work, I examined the structural, thermal, and subsidence record of this basin (Young, 2023, Chapters 1&2). Here, I use this context to elucidate the development of overpressure conditions under the influence of a high sedimentation rate within the Colorado River delta. The FCVB exposes the upper 2 to 4 km of the crust heated to <90°C and thus provides an opportunity to directly sample relatively unaltered rocks from the upper seismogenic zone to test whether overpressure conditions may have developed at depth. Geologic mapping from Young (2023, Chapter 1) shows that the FCVB deposition and subsidence was partitioned between two normal faults: the West Salton Detachment fault and the proto-Vallecito fault, a predecessor to the active, sinistral Vallecito fault (Figure 3.2). This model is supported by depositional relationships within marginal marine facies of the well-known Split Mountain and Imperial Groups, including newly defined proximal, scarp-derived facies along the proto-Vallecito fault.

New apatite (U-Th)/He data by Young (2023, Chapter 2) from the lower half of the FCVB section and adjacent basement show partial to no resetting, as indicated by preservation of detrital age signatures. Thermal modeling supports that rapid sedimentation depressed the geothermal gradient, keeping the section cool at depth, with maximum temperatures of about 80-90°C. Though the sediments preserved within the FCVB are analogous to those within the

greater Salton Trough, the geothermal gradient is much higher within the present-day rift axis, which has been attributed to continental rupture and magmatic underplating (Chapter 2).

Using this new structural and tectonic context for the Fish Creek Vallecito basin and borehole observations from near the Salton Sea, I seek to assess the effects of rapid sedimentation and presence of units with low hydraulic conductivity on the development of excess hydraulic head within the basin. I predict that these characteristics of the Fish Creek Vallecito basin and Salton Trough lead to the development of overpressure, or excess pore fluid pressure, which may promote regional fault creep.

METHODS

Model Set Up

To model the nonlinear coupled effects of sedimentation, compaction, and fluid flow, I developed a Python-based implementation of Bethke and Corbet's (1988) one-dimensional basin model. This model describes how fluid flow evolves in response to the effects of sediment and water added to the surface over geologic time. Because overpressure, or excess hydraulic head, is reflected in the rock record by porosity values higher than expected for a given burial depth (Bethke and Corbet, 1988; Jiang et al., 2010), I set up a model that will allow for comparison against measurable properties (e.g., porosity and permeability), allowing for future comparison of model results to measured values in the rock record.

For the case of constant of hydraulic conductivity, *K*, and specific storage, *S*, the upward diffusion of water in a growing sediment column over an impermeable basement is described analytically by the Gibson equation (Gibson, 1958):

$$\frac{K}{S}\frac{\partial^2 h}{\partial z^2} = \frac{\partial h}{\partial t} - \frac{\rho\prime}{\rho}\omega \tag{1}$$

Here, *h* is the hydraulic head in excess of hydrostatic, *z* is elevation above an effectively impermeable basement, and ω is the sedimentation rate. ρ' is the difference between the saturated sediment density, ρ, and the density of the pore fluid. The ratio *K/S* is the hydraulic diffusivity.

Bethke and Corbet (1988) extended the Gibson (1958) model to the more geologically realistic condition where both *K* and *S* evolve as sediment compaction removes porosity, ϕ. In this case, the governing equation becomes non-linear because both porosity and permeability are functions of effective stress and, thus, depth:

$$\frac{\partial}{\partial z}\left(K(\phi)\frac{\partial h}{\partial z}\right) = S(\phi)\left(\frac{\partial h}{\partial t} - \frac{\rho\prime}{\rho}\omega\right) \tag{2}$$

This equation is solved with a two-pass implicit finite difference approach. At each time step, the first pass uses an estimate of effective stress, $\sigma_{e,}$ to predict *S*. The second pass uses a revised effective stress based on the updated hydraulic head. The topmost element of this model grows over time as sediment is added, with new elements added once the topmost element attains the thickness of the other elements of the model. Porosity is parameterized with an exponential relationship (Athy, 1930):

$$\phi = \phi_0 exp\left(-\frac{b\sigma_e}{\rho\prime g}\right) \tag{3}$$

Initial porosity, ϕ_0, and the constant *b* are material parameters that depend on sediment type, and *g* is the acceleration due to gravity.

The algebraic approximation of the governing equation (eq. 2) is:

$$\frac{1}{2}[S^n + S^{n+1}]\left(\frac{h_i^{n+1} - h_i^n}{\Delta t} - \omega\frac{\rho'}{\rho}\right) = \frac{1}{2\Delta z^2}\left[K_{i+1/2}(h_{i+1} - h_i) + K_{i-1/2}(h_{i-1} - h_i)\right]^{n+1} +$$

$$\frac{1}{2\Delta z^2}[K_{i+1/2}(h_{i+1} - h_i) + K_{i-1/2}(h_{i-1} - h_i)]^n \quad (4)$$

Where Δz is the spacing of the nodal block and Δt is the time step (Bethke and Corbet 1988). Subscript *i* refers to the depth of an element within the model, and the superscript *n* refers to the time step. This equation is solved following a Crank-Nicolson approach (Crank and Nicolson, 1947), which is then represented and solved in matrix form:

$$Xh^{n+1} = Yh^n + d \quad (5)$$

The top boundary condition is dictated by the location of the depositional surface and by the condition that the top element may be thinner than the underlying element (Figure 3.3). The second derivative term for three unequally spaced elements is shown in Figure 3.3. The basal boundary condition is:

$$\frac{d}{dz} = 0: h_{i+1} - 2h_i + h_{i-1} \rightarrow -h_i + h_{i-1} \quad (6)$$

We extended the original model of Bethke and Corbet (1988) to include layers of different properties, suitable for modeling the intercalation of high- and low-permeability strata present within the Salton Trough. For a detailed list of equations used in this model and the python implementation and validation, please see Appendix 3.1 and 3.2.

Model Inputs

I use the fluvial, marine, deltaic, and lacustrine sediments in the Fish Creek Vallecito basin and the Salton Trough as model inputs for the element types, order of stratigraphy, and sedimentation rates over time. Modeled stratigraphy for the FCVB is simplified from Dorsey et al. (2011) and derived from surface exposures of the exhumed sedimentary section. I model the FCVB strata as both a continuous 5.5 km-thick section and as thinner sections deposited within a partitioned basin. For the continuous FCVB model, rates and thickness for FCVB deposition are also from Dorsey et al. (2011). For the partitioned FCVB model, depth of burial and sedimentation rates for FCVB sediment is based on the structural model in Young (2023, Chapters 1&2, Figure 3.2). Stratigraphy and sedimentation rates for the modern Salton Trough are simplified from borehole data (Babcock, 1974; Randall, 1974). Porosity and permeability values for each element were estimated based values from Mann and MacKenzie (1990). I also model a reference column of only fine sand using the same sedimentation rates over time as used when modeling the modern Salton Trough. This reference column allows for comparison between varied basin stratigraphy with high and low permeability units and uniform stratigraphy, where low permeability units are absent. Once the model column has been built to represent the respective location/basin, I add 500 m of coarse sand at 0.0001 mm/yr and 100m of coarse sand at 0.0001 m/yr. This reduction in sedimentation rate causes deposition in the model to essentially cease and shows how the observed properties change because of this cessation.

Model Validation

Samples were collected from throughout the entire FCVB section. From these samples, I can measure the density and estimate porosity of the rocks in the exhumed FCVB to compare against the model-predicted values. Methods for determining the density and porosity available to me thus far have been too imprecise for use in measuring these samples. Additional approaches remain untried and were incompatible with the timeline and the budget for this dissertation.

RESULTS

Using this model, I track how porosity, hydraulic conductivity, pore pressure ratio, and excess hydraulic head change with depth for a given sediment column and sedimentation rates. Overpressure is represented here by excess hydraulic head (h), which is measured in meters and is the height of water in excess of hydrostatic. Pore pressure ratio (λ) is the ratio of pore pressure over lithostatic stress and is unitless. Permeability is evaluated here as hydraulic conductivity (K), which is the ease with which water passes through a medium and is reported in m^{-2}. Porosity (ϕ) is the unitless percentage of void space in a volume of rock. Most plots in this section show h and ϕ. Some, but not all, show K since the shape of the curve for K is usually predictable from ϕ, and the values do not vary widely for different sedimentation rates.

First, I test the effect of sedimentation rate on excess hydraulic head with depth. To do this, I model a simple column of sand. The lower 500 m is coarse sand, mimicking the coarse

units expected on top of bedrock for the Salton Trough region. Then, I add fine sand on top. This same column is built with sedimentation rates of 0.0001, 0.001, 0.01, and 0.1 m/yr, as well as with a variable sedimentation rate similar to that expected for the Salton Trough (Figure 3.4). The excess hydraulic head builds up in the fine sand layer and more than doubles with each order of magnitude increase in sedimentation rate. The maximum rate of the varied column is 0.006 m/yr. The amount of additional excess hydraulic head for the varied rate is about twice that for the column modeled at 0.001 m/yr. The shape of the varied rate curve is comparable to the constant rate curves.

Second, I tested the effect of sedimentation rate and presence of caprock on effective hydraulic head. To do this, I modeled different stratigraphic columns at two rates: 0.0005 m/y and 0.01 m/yr (Figure 3.5). The four columns modeled all have a 500 m coarse sand layer at the base. I then varied the position of a shale layer throughout a column of fine sand and included a column without the shale layer as a control. For all modeled columns, the amount of excess hydraulic head is higher above the shale layer when the sedimentation rate is faster. For the model with shale at the base of the section, the amount of excess hydraulic head below the shale is comparable between the two sedimentation rates tested. For the model with shale in the middle of the section, the amount of excess hydraulic head below the shale is comparable but ~100 m lower for the slower rate. For the model with shale at the top of the section, the amount of excess hydraulic head below the shale for the slower rate is almost half that of the faster rate. For the column without shale, similar to the relationships shown in Figure 3.4, the slower rate has about 970 m less excess hydraulic head than the faster sedimentation rate. Porosity values do not change as dramatically, generally starting at around 0.54 and decreasing

to 0.52 in the fine sand. This decrease occurs and is preserved both below and above the shale layers. The porosity of the shale stays at about 0.625. Note that there are some edge artifacts that appear at the boundaries between fine sand and shale layers that show up in the porosity curves. These occur due to interpolation of permeability across the boundary and are ignored for this study.

Last, I replicated two simplified columns of Salton Trough stratigraphy from the FCVB and from a borehole near the Salton Sea. These columns varied in both sediment type and sedimentation rate, as shown in Figure 3.6. The FCVB was modeled as a continuous basin after Dorsey et al. (2011) and as a partitioned basin after Young (2023, Chapters 1&2). The continuous FCVB model set up assumes deposition was continuous and the full thickness of the FCVB strata occurred in a single column (Figure 3.6). The partitioned model treats the lower FCVB (Deguynos and lower) and upper FCVB (Deguynos and above) as separate columns and uses thickness and rates based on Young (2023, Chapters 1&2). Partitioning does not produce significant differences in results (Figure 3.7). The shapes of each part of the curve are the same, but in the lower FCVB, the excess hydraulic head is about 600 m, and in the upper FCVB, excess hydraulic head is about 3000 m, compared to just under 3500 m for the continuous FCVB model. Since the upper FCVB is more analogous to the Salton Trough, and since the excess hydraulic head is comparable between the two, it appears that the FCVB is a reasonable proxy for pore-pressure conditions within the Salton trough. For simplicity, additional models of the FCVB were performed using the continuous model setup.

For the Salton trough, the modeled section is based on borehole data and measured section from the western shore of the Salton Sea (Babcock, 1974; Randall, 1974)). This column

is compared with an all-sand column with the same changes in sedimentation rate as a point of reference. In the reference sand column, the increase in excess hydraulic head with depth is significantly less than in the column modeled with varied strata over the same sedimentation rate changes and duration. Porosity also decreases with depth in the reference sand column, compared to the varied strata. There is less compaction in the varied strata than in the sand column, as shown by the porosity curves in Figure 3.6. For both the FCVB and the Salton Trough columns, the pore pressure ratio (λ) is > 0.6 below 500-1000m depth (Figure 3.6).

In a final set of models, I slow deposition above the FCVB and Salton Trough and reference columns to 0.0001 m/yr for 500 m (5 Myr) and for 100 m of sediment (1 Myr). While 5 Myr m is an unrealistic period of slow sedimentation for the region, it is a way to explore the effects of prolonged slowing or cessation of deposition on the decline of overpressure conditions at depth. When deposition is slowed, fluid escape can keep up with or outpace burial. In the FCVB and Salton Trough columns, with shale layers, the excess hydraulic head is maintained and continues to increase with burial despite slow deposition. In the reference sand column, the excess hydraulic head at depth declines to nearly zero in both cases. The 500 m of slow deposition is shown in Figure 3.6, and the 100 m is similar, with excess head decreasing from over 200 m during rapid deposition to about 12 m during slowed deposition. The presence of shale caprock is thus vital to maintaining the overpressure conditions at depth when the sedimentation rate is no longer sufficient and pore fluids can escape out of unconfined layers.

DISCUSSION

In both the Salton Trough and FCVB sections, overpressure develops within the lowermost basin sediments, beneath low permeability facies like delta front shale and silt from the Colorado River. Low permeability mudstones act as caprocks, creating confined aquifers in the sand layers below them. Elevated pore pressure at depth occurs below these units and approaches lithostatic pressure more readily than when caprocks are absent. In the underlying sand units, porosity and hydraulic conductivity continue to decrease with depth/burial, though at a lower rate than in the unconfined case. The change in excess hydraulic head below the caprock is slowed almost completely as the rate of fluid migration out of the sediment is also slowed. When combined with the continued addition of sediment and water above the caprock, the relative reduction in fluid migration drives overpressure development. When caprock is present, this overpressure is maintained even when the sedimentation rate is near zero. In the all-sand reference column, however, reducing the sedimentation rate allows fluids to escape from the column, reducing the excess hydraulic head to nearly zero over 5 Myr and to a nominal value of ~12 m over 1 Myr.

Two important outcomes of these preliminary models are: 1) within the actively subsiding Salton Trough, the ratio of pore pressure to lithostatic load (λ) is probably everywhere ≥ 0.6 (Figure 3.6) due to the combination of lower-density porous sediment and excess pore pressure developed beneath fine-grained lacustrine and marine strata. This is well above the standard value of $\lambda \cong 0.4$ assumed for effective stress in bedrock under hydrostatic conditions – an assumption common in Coulomb stress transfer models (e.g., Toda, 2005). 2) Overpressure conditions are likely present and could promote fault creep in the Salton Trough.

Faults like the southern San Andreas fault, Superstition Hills fault, and the Imperial fault creep within the upper 0-4 km of the crust (Harris 2017 *and references therein*). Our modeled sediment columns show significant pore fluid pressure developing at these depths, which may lead to aseismic behavior in the brittle upper crust.

Future work may explore coulomb stress changes and lake loading, the reduction of stress on faults due to the excess pore pressure, thermal effects, and the relationship between pore pressure, creep, and seismicity. Coulomb stress changes due to periodic flooding of the Salton Trough (e.g., Lake Cahuilla) load the basin and produce associated pore-pressure changes that have been proposed and shown to trigger earthquakes along the southern San Andreas fault (Luttrell et al., 2007; Brothers et al., 2011; Hill et al., 2023). Alternatively, as pointed out by Brothers et al. (2011), direct loading of low-permeability aquicludes by the weight of flood water could also contribute to excess pore pressure at seismogenic depths. The relationship between surface water loading and excess pore fluid pressure promoting fault creep is yet unexplored. Embedded, fault-specific pore pressure conditions, which may be strongly affected by a damage zone with higher fracture permeability surrounding low-permeability fault core, may also be a topic of future study. Excess pore fluids may also change the thermal and chemical properties of rocks at depth (e.g., Kämmlein and Stollhofen, 2019) and is worth considering in models of regional heat flow. Similarly, future work to explore the relationship between model results and regional seismicity would benefit from direct testing of density and porosity from the strata exposed within the FCVB to validate modeled values.

CONCLUSIONS

The sediment columns modeled in this study support the development of overpressure at depth in the Salton Trough. This is important as overpressure likely leads to fault creep, which is observed regionally, and may promote earthquake triggering. High sedimentation rates help promote overpressure development, especially in sandy units. The presence of impermeable caprocks is essential for maintaining overpressure at depth once deposition has slowed or stopped. In the FCVB, the Deguynos Formation and the lacustrine units of the Palm Spring Group act as caprocks, elevating the excess hydraulic head. Even without these impermeable units, rapid sedimentation rates, like those seen in the Salton Trough, can produce excess hydraulic head at depth in the region.

FIGURES

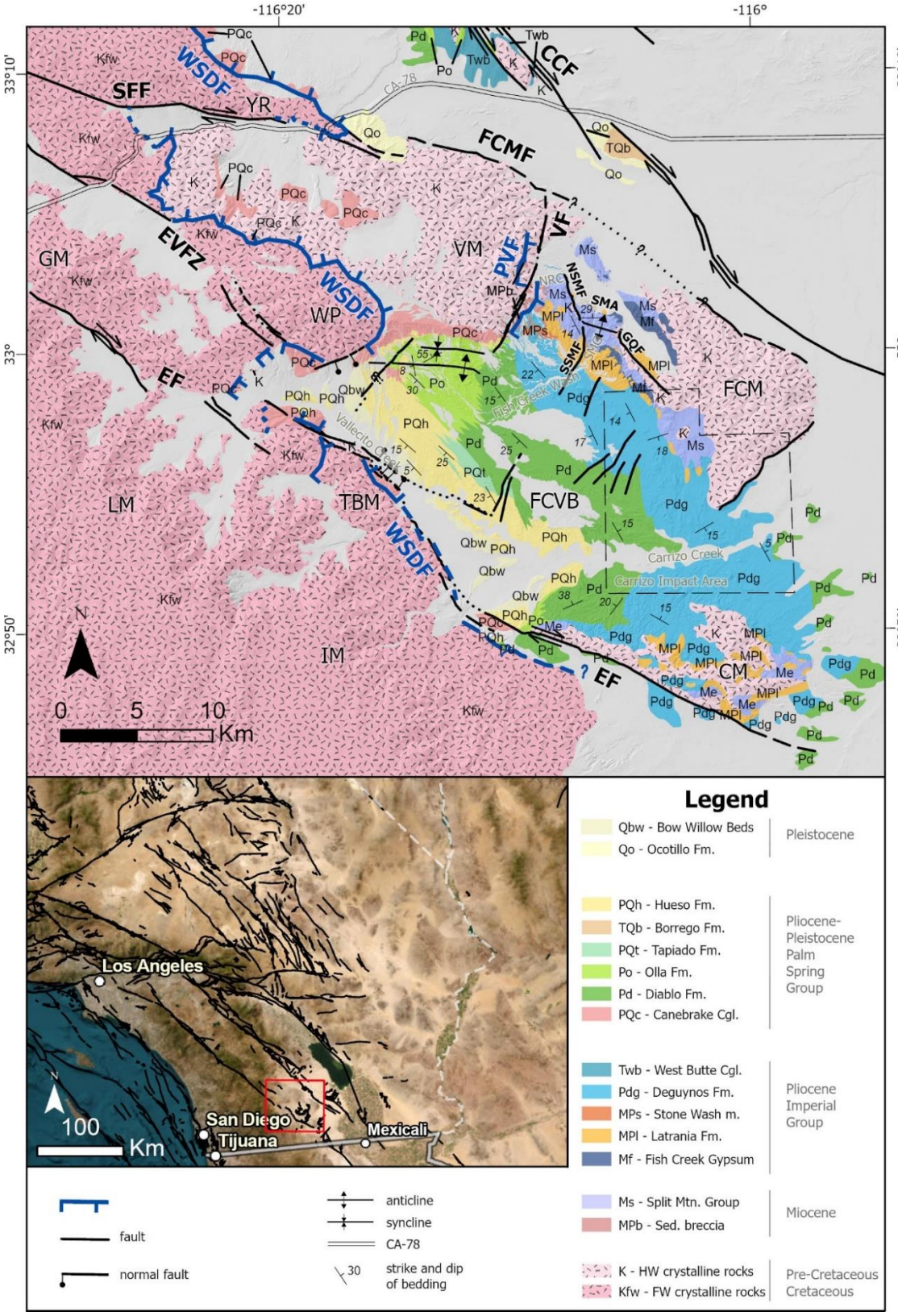

Figure 3.1. Caption on following page

Caption to Figure 3.1: Geologic map of the FCVB and surrounding region. Alluvium is not mapped. Units MPb and PQc are time transgressive, spanning the Miocene-Pliocene and the Pliocene-Pleistocene respectively; they are placed in the legend at the time of their first occurrence. Lower map shows the location of the regional map and the FCVB within southern California and the Quaternary fault and fold database (USGS and CGS). See Plate 1 for the position of the map area within the state of California. Compiled from Dorsey et al. (2011), Janecke et al. (2010), and this study.

CCF = Coyote Creek fault strand of the San Jacinto fault zone, CM = Coyote Mountains, EF = Elsinore fault, EVFZ = Earthquake Valley fault zone of the Elsinore fault system, FCM = Fish Creek Mountains, FCMF = Fish Creek Mountain fault, GM = Granite Mountain, GQF = Gypsum Quarry fault, IM = Inkopa Mountains, LM = Laguna Mountains, NRC = No Return Canyon, NSMF = Northern Split Mountain fault, PVF = proto-Vallecito fault, SFF = San Felipe fault, SMA = Split Mountain anticline, SMG = Split Mountain Gorge, SSMF = Southern Split Mountain fault, TBM = Tierra Blanca Mountains, VF = Vallecito fault, WP = Whale Peak, WSDF = West Salton Detachment fault, VM = Vallecito Mountains, YR = Yaqui Ridge.

Hillshade in regional geologic map from USGS 3DEP, imagery in lower map from ESRI World Imagery (ESRI, 2022).

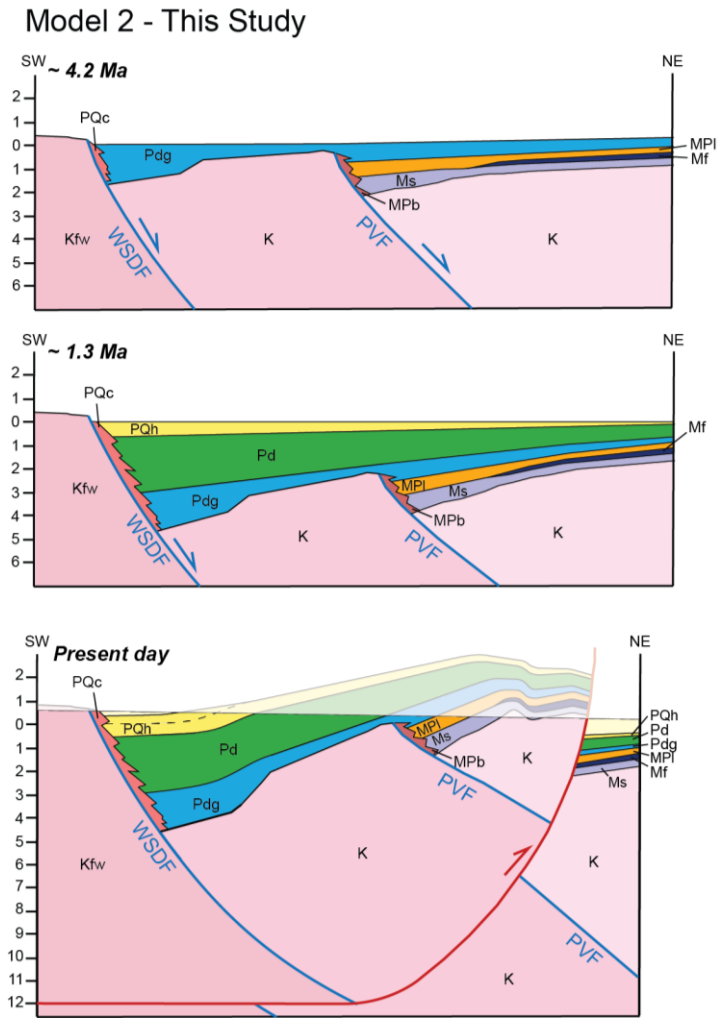

Figure 3.2. Model of FCVB evolution based on Young (2023, Chapters 1&2). Note the basin is partitioned across two normal faults.

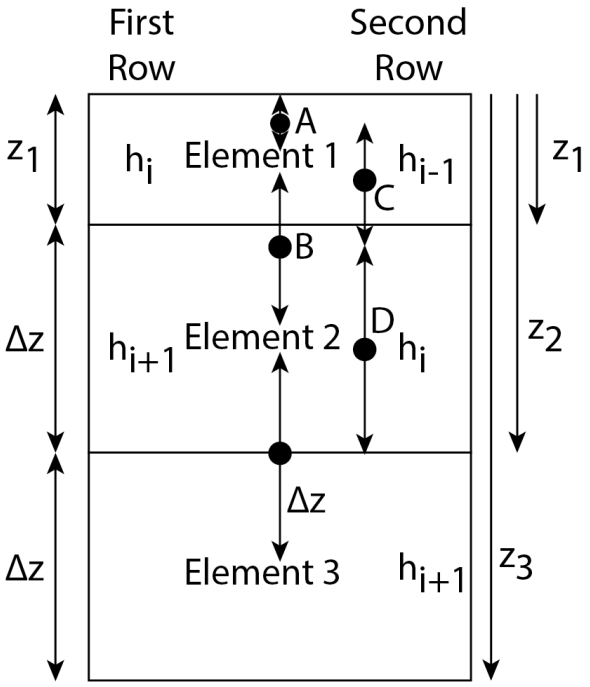

Centered on element 1:

$$\frac{d^2h}{dz^2} = \frac{\frac{h_{i+1}-h_i}{B} - \frac{h_i}{A}}{C} = \frac{h_{i+1}-h_i}{BC} - \frac{h_i}{AC}$$

Centered on element 2:

$$\frac{d^2h}{dz^2} = \frac{\frac{h_{i+1}-h_i}{\Delta z} - \frac{h_i-h_{i-1}}{B}}{D} = \frac{h_{i+1}-h_i}{D\Delta z} - \frac{h_i-h_{i-1}}{BD}$$

$A = \frac{z_1}{2}$

$B = \frac{z_1}{2} + \frac{z_2-z_1}{2} = \frac{z_2}{2}$

$C = \frac{A}{2} + \frac{B}{2} = \frac{z_1}{4} + \frac{z_2}{4} = \frac{1}{4}(z_1 + z_2)$

$D = z_2 - A - \frac{B}{2} = z_2 - \frac{z_1}{2} - \frac{z_2}{4} = \frac{3}{4}z_2 - \frac{1}{2}z_1$

As $z_1 \to \Delta z$, $A \to \frac{1}{2}\Delta z$, $B, D \to \Delta z$, and $C \to \frac{3}{4}\Delta z$

Figure 3.3. Diagram showing how elements are added to the model. Additional details available in Appendix 3.1.

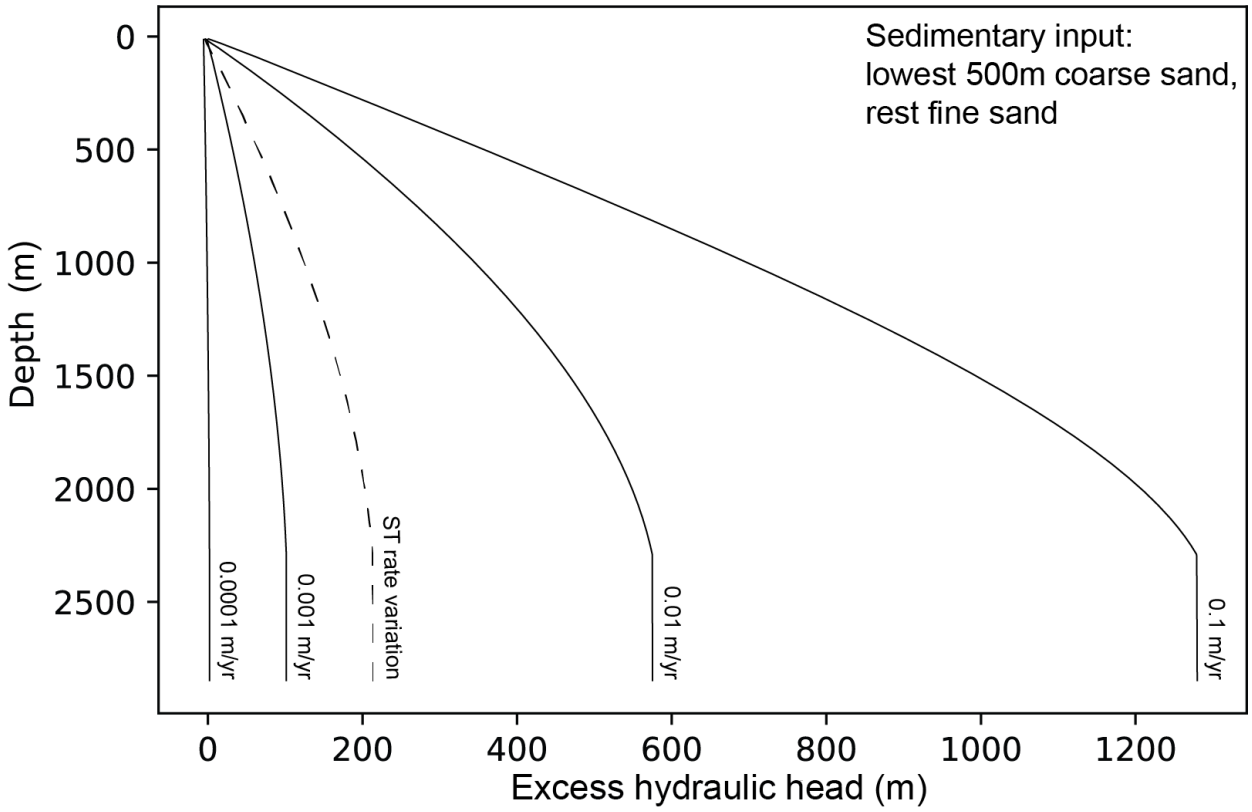

Figure 3.4. Plot of excess hydraulic head with depth for a column of all sand deposited at range of sedimentation rates.

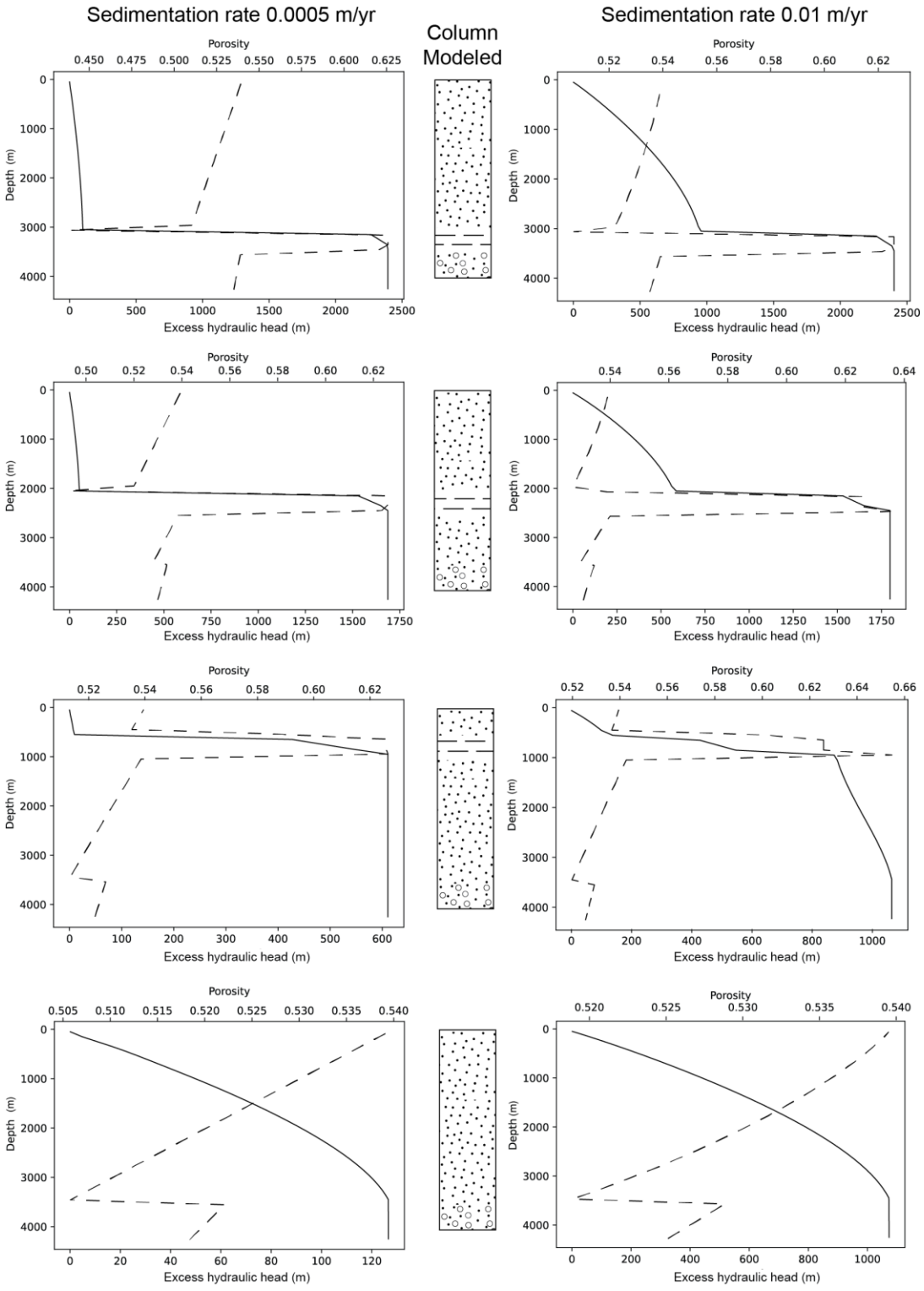

Figure 3.5. Plots of excess hydraulic head and porosity with depth for columns modeled at 0.0005 m/yr (right) and at 0.01 m/yr (left). In each column, the position of the shale layer was varied, as shown by the column modeled in the middle of the figure.

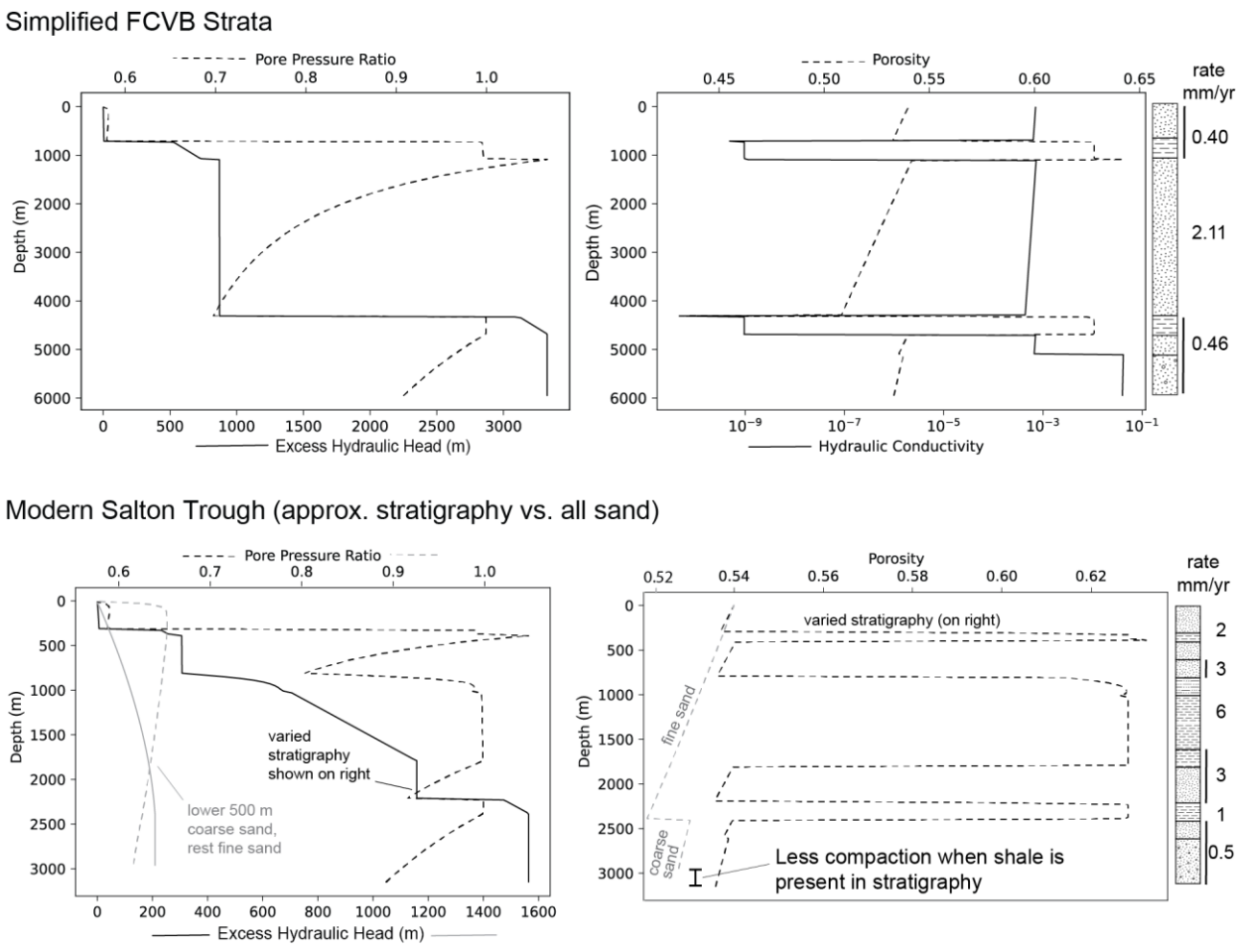

Figure 3.6. Caption on following page

Caption to Figure 3.6. Plots showing how excess hydraulic head, pore pressure ratio, hydraulic conductivity, and porosity vary with depth for three different stratigraphic columns using our 1D model. The first stratigraphic column is a simplified version of the FCVB stratigraphy deposited with rates based on Figure 7 (first row). The second stratigraphic column is an approximate version of the stratigraphy in the modern Salton Trough (Babcock, 1974; Randall, 1974). This is plotted with the third stratigraphic column, which is deposited at the same rate as the approximate modern Salton Trough but is simplified to 500 m of coarse sand at the bottom, followed by fine sand to the top. This comparison shows how important shale layers are in building excess hydraulic head (second row). The bottom left plot shows excess hydraulic head with depth for all three stratigraphic columns after having 500 m of coarse sand added to the top at 0.0001 mm/yr. For the FCVB and the approximate modern Salton Trough, the curves below this deposition shift down and to the right, but their shape is largely unchanged.

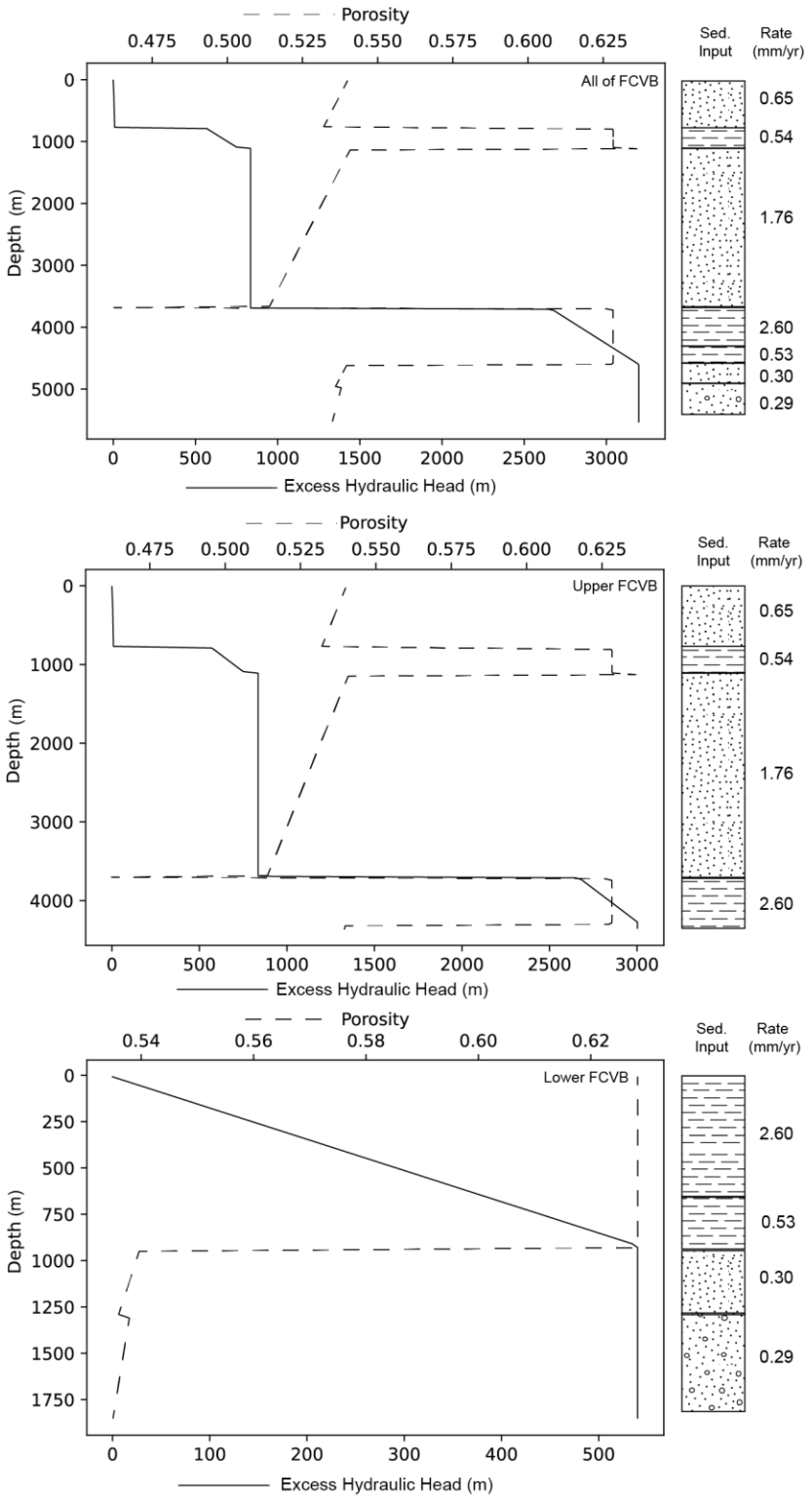

Figure 3.7. Plot of excess hydraulic head and porosity with depth for the Fish Creek Vallecito basin based on sedimentation rates consistent with the Young (2023) model of partitioned basin deposition. The upper plot is a detailed FCVB column without partition, and the lower two diagrams are that same column split into two separate columns at the Deguynos Formation.

REFERENCES

Athy, L. F., (1930) Density, Porosity, and Compaction of Sedimentary Rocks. Association of Petroleum Geologists Bulletin 34, no. 5, p. 1–24.

Babcock, E.A., 1974, Geology of the Northeast Margin of the Salton Trough, Salton Sea, California: Geological Society of America Bulletin, v. 85, p. 321, doi:10.1130/0016-7606(1974)85<321:GOTNMO>2.0.CO;2.

Behrmann, J.H., Flemings, P.B., John, C.M., and the IODP Expedition 308 Scientists, 2006, Rapid Sedimentation, Overpressure, and Focused Fluid Flow, Gulf of Mexico Continental Margin: Scientific Drilling, v. 3, p. 12–17, doi:10.5194/sd-3-12-2006.

Bethke, C.M., and Corbet, T.F., 1988, Linear and nonlinear solutions for one-dimensional compaction flow in sedimentary basins: Water Resources Research, v. 24, p. 461–467, doi:10.1029/WR024i003p00461.

Brodsky, E.E., 2006, Long-range triggered earthquakes that continue after the wave train passes: Geophysical Research Letters, v. 33, doi:10.1029/2006GL026605.

Brodsky, E., E., and Lajoie, L., J., 2013, Anthropogenic Seismicity Rates and Operational Parameters at the Salton Sea Geothermal Field: Sciencexpress Reports.

Brodsky, E.E., and Prejean, S.G., 2005, New constraints on mechanisms of remotely triggered seismicity at Long Valley Caldera: TRIGGERING CONSTRAINTS: Journal of Geophysical Research: Solid Earth, v. 110, doi:10.1029/2004JB003211.

Brothers, D. S., Driscoll, N. W., Kent, G. M., Harding, A. J., Babcock, J. M., and Baskin, R. L., 2009, Tectonic Evolution of the Salton Sea Inferred from Seismic Reflection Data: Nature Geoscience, v. 2, no. 8, p. 581–84. https://doi.org/10.1038/ngeo590.

Brothers, D., Kilb, D., Luttrell, K., Driscoll, N., and Kent, G., 2011, Loading of the San Andreas Fault by Flood-Induced Rupture of Faults beneath the Salton Sea: Nature Geoscience, v. 4, no. 7, p. 486–92. https://doi.org/10.1038/ngeo1184.

Chen, X., and Shearer, P. M., 2011, Comprehensive Analysis of Earthquake Source Spectra and Swarms in the Salton Trough, California: Journal of Geophysical Research, v. 116, no. B9: B09309. https://doi.org/10.1029/2011JB008263.

Crank, J., and Nicolson, P., 1947, A practical method for numerical evaluation of solutions of partial differential equations of the heat-conduction type: Mathematical Proceedings of the Cambridge Philosophical Society, v. 43, p. 50–67, doi:10.1017/S0305004100023197.

Dorsey, R.J., Housen, B.A., Janecke, S.U., Fanning, C.M., and Spears, A.L.F., 2011, Stratigraphic record of basin development within the San Andreas fault system: Late Cenozoic Fish Creek-Vallecito basin, southern California: Geological Society of America Bulletin, v. 123, p. 771–793, doi:10.1130/B30168.1.

Esri, 2022, "Topographic" [basemap]. 1:6,500,000. "World Topographic Map". https://www.arcgis.com/home/item.html?id=10df2279f9684e4a9f6a7f08febac2a9. (September, 2023)

Faulkner, D.R., and Rutter, E.H., 2001, Can the maintenance of overpressured fluids in large strike-slip fault zones explain their apparent weakness? Geology, v. 29, p. 503, doi:10.1130/0091-7613(2001)029<0503:CTMOOF>2.0.CO;2.

Fuis, G.S., Mooney, W.D., Healy, J.H., McMechan, G.A., and Lutter, W.J., 1984, A seismic refraction survey of the Imperial Valley Region, California: Journal of Geophysical Research: Solid Earth, v. 89, p. 1165–1189, doi:10.1029/JB089iB02p01165.

Gibson, R. E., 1958, The Progress of Consolidation in a Clay Layer Increasing in Thickness: Geotechnique v. 8, p. 171–82.

Goebel, T.H.W., and Brodsky, E.E., 2018, The spatial footprint of injection wells in a global compilation of induced earthquake sequences: Science, v. 361, p. 899–904, doi:10.1126/science.aat5449.

Goebel, T.H.W., Hauksson, E., Aminzadeh, F., and Ampuero, J.-P., 2015, An objective method for the assessment of fluid injection-induced seismicity and application to tectonically active regions in central California: Journal of Geophysical Research: Solid Earth, v. 120, p. 7013–7032, doi:10.1002/2015JB011895.

Gratier, J.-P., Richard, J., Renard, F., Mittempergher, S., Doan, M. L., Di Toro, G., Hadizadeh, J., and Boullier, A.-M., 2011, Aseismic sliding of active faults by pressure solution creep: Evidence from the San Andreas Fault Observatory at Depth: Geology, v. 39, p. 1131–1134, doi:10.1130/G32073.1.

Harris, R.A., 2017, Large earthquakes and creeping faults: Large Earthquakes and Creeping Faults: Reviews of Geophysics, v. 55, p. 169–198, doi:10.1002/2016RG000539.

Hill, R.G., Weingarten, M., Rockwell, T.K., and Fialko, Y., 2023, Major southern San Andreas earthquakes modulated by lake-filling events: Nature, v. 618, p. 761–766, doi:10.1038/s41586-023-06058-9.

Holdsworth, R.E., van Diggelen, E.W.E., Spiers, C.J., de Bresser, J.H.P., Walker, R.J., and Bowen, L., 2011, Fault rocks from the SAFOD core samples: Implications for weakening at shallow depths along the San Andreas Fault, California: Journal of Structural Geology, v. 33, p. 132–144, doi:10.1016/j.jsg.2010.11.010.

Hubbert, M.K., and Rubey, W.W., 1959, Role of Fluid Pressure in Mechanics of Overthrust Faulting I: Mechanics of Fluid-Filled Porous Solids and Its Application to Overthrust Faulting: Bulletin of the Geological Society of America, v. 70, p. 115–166.

Hulen, J., Norton, D., Kaspereit, D., Murray, L., van de Putte, T., and Wright, M., 2003, Geology and a Working Conceptual Model of the Obsidian Butte (Unit 6) Sector of the Salton Sea Geothermal Field, California: Geothermal; Resources Council Transactions, v. 27, p. 12–15.

Jiang, X.-W., Wang, X.-S., and Wan, L., 2010, Semi-empirical equations for the systematic decrease in permeability with depth in porous and fractured mdia: Hydrogeology Journal, v. 18, p. 839–850, doi:10.1007/s10040-010-0575-3.

Kämmlein, M., and Stollhofen, H., 2019, Pore-fluid-dependent controls of matrix and bulk thermal conductivity of mineralogically heterogeneous sandstones: Geothermal Energy, v. 7, p. 13, doi:10.1186/s40517-019-0129-4.

Lindsey, E. O., Fialko, Y., Bock, Y., Sandwell, D. T., and Bilham, R., 2014, Localized and Distributed Creep along the Southern San Andreas Fault: Journal of Geophysical Research: Solid Earth, v. 119, no. 10, p. 7909–22. https://doi.org/10.1002/2014JB011275.

Lockner, D.A., Morrow, C., Moore, D., and Hickman, S., 2011, Low strength of deep San Andreas fault gouge from SAFOD core: Nature, v. 472, p. 82–85, doi:10.1038/nature09927.

Lohman, R. B., and McGuire, J. J., 2007, Earthquake Swarms Driven by Aseismic Creep in the Salton Trough, California: Obsidian Buttes Swarm: Journal of Geophysical Research: Solid Earth, v. 112, no. B4. https://doi.org/10.1029/2006JB004596.

Luttrell, K., Sandwell, D., Smith-Konter, B., Bills, B., and Bock, Y., 2007, Modulation of the Earthquake Cycle at the Southern San Andreas Fault by Lake Loading: Journal of Geophysical Research, v. 112, no. B8, p. B08411. https://doi.org/10.1029/2006JB004752.

Mann, D.M., and Mackenzie, A.S., 1990, Prediction of pore fluid pressures in sedimentary basins: Marine and Petroleum Geology, v. 7, p. 55–65, doi:10.1016/0264-8172(90)90056-M.

Randall, W., 1974, An Analysis of the Subsurface Structure and Stratigraphy of the Salton Sea Geothermal Anomaly, Imperial Valley, California [PhD]: University of California, Riverside.

Ross, Z.E., Trugman, D.T., Hauksson, E., and Shearer, P.M., 2019, Searching for hidden earthquakes in Southern California: Science, v. 364, p. 767–771, doi:10.1126/science.aaw6888.

Toda, S., 2005, Forecasting the Evolution of Seismicity in Southern California: Animations Built on Earthquake Stress Transfer: Journal of Geophysical Research, v. 110, no. B5. https://doi.org/10.1029/2004JB003415.

U.S. Geological Survey, 20220815, USGS Lidar Point Cloud CA_Eastern_San_Diego_Co_Lidar_2016_B16: U.S. Geological Survey. Distributed by OpenTopography. Accessed: December 2019.

U.S. Geological Survey and California Geological Survey (2004). Quaternary fault and fold database for the United States, from USGS website available at https://www.usgs.gov/naturalhazards/ earthquake-hazards/faults (last accessed February 2021).

Warr, L.N., Wojatschke, J., Carpenter, B.M., Marone, C., Schleicher, A.M., and van der Pluijm, B.A., 2014, A “slice-and-view” (FIB–SEM) study of clay gouge from the SAFOD creeping section of the San Andreas Fault at ∼2.7 km depth: Journal of Structural Geology, v. 69, p. 234–244, doi:10.1016/j.jsg.2014.10.006.

Zoback, M.D. et al., 1987, New Evidence on the State of Stress of the San Andreas Fault System: Science, v. 238, p. 1105–1111, doi:10.1126/science.238.4830.1105.

Zoback, M.D., and Lachenbruch, A.H., 1992, Introduction to Special Section on the Cajon Pass Scientific Drilling Project: Journal of Geophysical Research, v. 97, p. 4991, doi:10.1029/91JB03110.

A3 – APPENDIX TO CHAPTER 3

The appendix to Chapter 3 has two parts listed below.

Appendix 3.1 – Finite Difference Scheme of Bethke and Corbet, 1988

Appendix 3.2 – Python Implementation of the Finite Difference Scheme

Appendix 3 References

Bethke, C.M., and Corbet, T.F., 1988, Linear and nonlinear solutions for one-dimensional compaction flow in sedimentary basins: Water Resources Research, v. 24, p. 461–467, doi:10.1029/WR024i003p00461.

Mann, D.M., and Mackenzie, A.S., 1990, Prediction of pore fluid pressures in sedimentary basins: Marine and Petroleum Geology, v. 7, p. 55–65, doi:10.1016/0264-8172(90)90056-M.

Appendix 3.1 – Finite Difference Scheme

This is the supplementary information for Chapter 3. This document walks through the solutions applied to the equations from Bethke and Corbet (1988) that are then used to make the compaction model presented in Chapter 3. The python implementation of this is found in Appendix 3.2.

Finite difference scheme based on Bethke and Corbet (1988) eq. 11

This equation is not used in the model but is kept here as a record.

$$\frac{1}{2}[S^n + S^{n+1}]\left(\frac{h_i^{n+1} - h_i^n}{\Delta t} - \omega\frac{\rho'}{\rho}\right) = \frac{K}{2\Delta z^2}[(h_{i+1} - 2h_i + h_{i-1})^{n+1} + (h_{i+1} - 2h_i + h_{i-1})^n]$$

Solving this equation follows a Crank-Nicolson approach (Crank and Nicolson, 1944). Elements from the $n+1$ time step are moved to the left hand side of the finite-difference equation:

$$\left(h_i^{n+1} - h_i^n - \omega\Delta t\frac{\rho'}{\rho}\right) = \frac{K\Delta t}{[S^n + S^{n+1}]\Delta z^2}[(h_{i+1} - 2h_i + h_{i-1})^{n+1} + (h_{i+1} - 2h_i + h_{i-1})^n]$$

$$r = \frac{K\Delta t}{[S^n + S^{n+1}]\Delta z^2}$$

$$-rh_{i-1}^{n+1} + (1+2r)h_i^{n+1} - rh_{i+1}^{n+1} = rh_{i-1}^n + (1-2r)h_i^n + rh_{i+1}^n + \omega\Delta t\frac{\rho'}{\rho}$$

This equation may be represented and solved in matrix form:

$$Xh^{n+1} = Yh^n + d$$

where the diagonal of X and Y are $1+2r$ and $1-2r$, respectively, and the immediate off diagonal components are $-r$ or $+r$, respectively. The solution is found by:

$$h^{n+1} = X^{-1}[Yh^n + d]$$

Because X is tridiagonal, finding X^{-1} is a fast (order n) operation.

Boundary conditions of the model change the coefficients of the first, second, and last rows of X and Y:

Basal boundary condition, $dh/dz = 0$: $h_{i+1} - 2h_i + h_{i-1} \rightarrow -h_i + h_{i-1}$. The coefficients for the last row of the matrix become $-r, 1+r$ or $r, 1-r$ for X and Y, respectively. Note that there is no coefficient for h_{i+1} in the last row.

Top boundary condition dictated by location of depositional surface, and that the thickness of the top element may be less than the underlying element. As illustrated here:

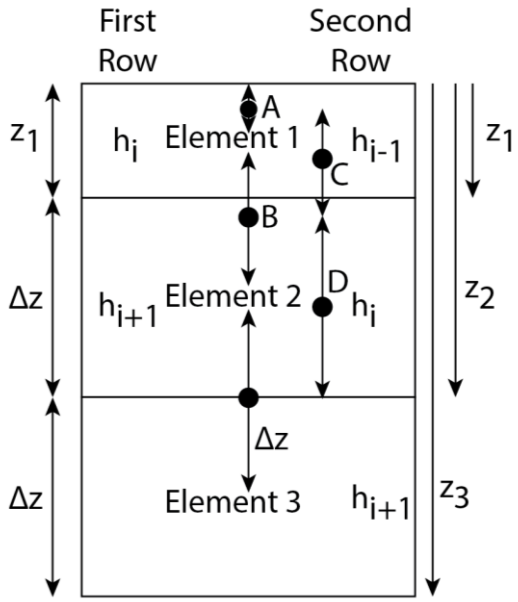

Figure A3.1. Visualization of top boundary condition

The second derivative term for three equally spaced elements:

$$\frac{d^2h}{dz^2} = \frac{\frac{h_{i+1} - h_i}{\Delta z} - \frac{h_i - h_{i-1}}{\Delta z}}{\Delta z}$$

The second derivative term for three unequally spaced elements (see figure):

Centered on element 1: $\frac{d^2h}{dz^2} = \frac{\frac{h_{i+1}-h_i}{B} - \frac{h_i}{A}}{C} = \frac{h_{i+1}-h_i}{BC} - \frac{h_i}{AC}$

Centered on element 2: $\frac{d^2h}{dz^2} = \frac{\frac{h_{i+1}-h_i}{\Delta z} - \frac{h_i-h_{i-1}}{B}}{D} = \frac{h_{i+1}-h_i}{D\Delta z} - \frac{h_i-h_{i-1}}{BD}$

From the geometry shown above:

$A = \frac{z_1}{2}$

$B = \frac{z_1}{2} + \frac{z_2 - z_1}{2} = \frac{z_2}{2}$

$C = \frac{A}{2} + \frac{B}{2} = \frac{z_1}{4} + \frac{z_2}{4} = \frac{1}{4}(z_1 + z_2)$

$D = z_2 - A - \frac{B}{2} = z_2 - \frac{z_1}{2} - \frac{z_2}{4} = \frac{3}{4}z_2 - \frac{1}{2}z_1$

As $z_1 \to \Delta z$, $A \to \frac{1}{2}\Delta z$, $B, D \to \Delta z$, and $C \to \frac{3}{4}\Delta z$

We wish to retain the values of r calculated above. Doing this requires factoring out Δz^2. We replace z_1 and z_2 with:

$\zeta_1 = \frac{z_1}{\Delta z}, \zeta_2 = \frac{z_2}{\Delta z}$

Recalculating the denominators above with Δz^2 factored:

$$\frac{1}{\Delta z^2} BC = \beta_1 = \frac{\zeta_2}{8}(\zeta_1 + \zeta_2)$$

$$\frac{1}{\Delta z^2} AC = \beta_2 = \frac{\zeta_1}{8}(\zeta_1 + \zeta_2)$$

$$\frac{1}{\Delta z^2} D\Delta z = \beta_3 = \frac{3}{4}\zeta_2 - \frac{1}{2}\zeta_1$$

$$\frac{1}{\Delta z^2} BD = \beta_4 = \frac{\zeta_2}{8}(3\zeta_2 - 2\zeta_1)$$

Rewriting eq. 11 in second derivative form:

$$\left(h_i^{n+1} - h_i^n - \omega \Delta t \frac{\rho'}{\rho}\right) =$$

$$\frac{K\Delta t}{[S^n + S^{n+1}]\Delta z^2}[(h_{i+1} - h_i)^{n+1} - (h_i - h_{i-1})^{n+1} + (h_{i+1} - h_i)^n - (h_i - h_{i-1})^n]$$

In the first row, $h_{i-1} = 0$ and with the correction coefficients the equation becomes:

$$\left(h_i^{n+1} - h_i^n - \omega \Delta t \frac{\rho'}{\rho}\right) = \frac{K\Delta t}{[S^n + S^{n+1}]\Delta z^2}\left[\frac{(h_{i+1} - h_i)^{n+1}}{\beta_1} - \frac{h_i^{n+1}}{\beta_2} + \frac{(h_{i+1} - h_i)^n}{\beta_1} - \frac{h_i^n}{\beta_2}\right]$$

From this, for row 1, we derive a new coefficient for h_i (note that the 1 comes from the h_i on the original left hand side). Use plus for X and minus for Y.

$$1 \pm r\left[\frac{1}{\beta_1} + \frac{1}{\beta_2}\right]$$

We also find a new coefficient for h_{i+1}. Use minus for X and plus for Y

$$\mp r \frac{1}{\beta_1}$$

Note that there is no coefficient for h_{i-1} for the first row.

For the second row:

$$\left(h_i^{n+1} - h_i^n - \omega \Delta t \frac{\rho'}{\rho}\right) = \frac{K\Delta t}{[S^n + S^{n+1}]\Delta z^2}\left[\frac{(h_{i+1} - h_i)^{n+1}}{\beta_3} - \frac{(h_i - h_{i-1})^{n+1}}{\beta_4} + \frac{(h_{i+1} - h_i)^n}{\beta_3} - \frac{(h_i - h_{i-1})^n}{\beta_4}\right]$$

For row 2, we similarly derive a new coefficient for h_i (note that the 1 comes from the h_i on the original left hand side). Use plus for X and minus for Y.

$$1 \pm r\left[\frac{1}{\beta_3} + \frac{1}{\beta_4}\right]$$

The new coefficients for h_{i+1} and h_{i-1}, respectively. Use minus for X and plus for Y

$$\mp r\frac{1}{\beta_3}, \mp r\frac{1}{\beta_4}$$

Finite difference scheme based on Bethke and Corbet (1988) eq. 13

$$\frac{1}{2}[S^n + S^{n+1}]\left(\frac{h_i^{n+1} - h_i^n}{\Delta t} - \omega\frac{\rho'}{\rho}\right) =$$

$$\frac{1}{2\Delta z^2}\left[K_{i+1/2}(h_{i+1} - h_i) + K_{i-1/2}(h_{i-1} - h_i)\right]^{n+1} + \frac{1}{2\Delta z^2}\left[K_{i+1/2}(h_{i+1} - h_i) + K_{i-1/2}(h_{i-1} - h_i)\right]^n$$

Solving this equation follows a Crank-Nicolson approach (Crank and Nicolson, 1944) very similar to what we employed for eq. 11. Elements from the $n+1$ time step are moved to the left hand side of the finite-difference equation:

$$\left(h_i^{n+1} - h_i^n - \omega\Delta t\frac{\rho'}{\rho}\right) =$$

$$\frac{\Delta t}{[S^n + S^{n+1}]\Delta z^2}\left[K_{i+1/2}(h_{i+1} - h_i) + K_{i-1/2}(h_{i-1} - h_i)\right]^{n+1} + \frac{\Delta t}{[S^n + S^{n+1}]\Delta z^2}\left[K_{i+1/2}(h_{i+1} - h_i) + K_{i-1/2}(h_{i-1} - h_i)\right]^n$$

$$r = \frac{\Delta t}{[S^n + S^{n+1}]\Delta z^2}$$

$$-rK_{i-1/2}h_{i-1}^{n+1} + \left(1 + rK_{i+1/2} + rK_{i-1/2}\right)h_i^{n+1} - rK_{i+1/2}h_{i+1}^{n+1} = rK_{i-1/2}h_{i-1}^n + \left(1 - rK_{i+1/2} - rK_{i-1/2}\right)h_i^n + rK_{i+1/2}h_{i+1}^n + \omega\Delta t\frac{\rho'}{\rho}$$

This equation may be represented and solved in matrix form:

$$Xh^{n+1} = Yh^n + d$$

where the diagonal of X and Y are $1 + r\left(K_{i+1/2} + K_{i-1/2}\right)$ and $1 - r\left(K_{i+1/2} + K_{i-1/2}\right)$, respectively, and the immediate off diagonal components are $-rK_{i-1/2}$ and $-rK_{i+1/2}$ or $rK_{i-1/2}$ and $rK_{i+1/2}$, respectively. The solution is found by:

$$h^{n+1} = X^{-1}[Yh^n + d]$$

Boundary conditions of the model change the coefficients of the first, second, and last rows of X and Y:

Basal boundary condition, $dh/dz = 0$: $h_{i+1} - h_i = 0$. The finite difference equation simplifies to:

$$\left(h_i^{n+1} - h_i^n - \omega \Delta t \frac{\rho'}{\rho}\right) = r\left[K_{i-1/2}(h_{i-1} - h_i)\right]^{n+1} + r\left[K_{i-1/2}(h_{i-1} - h_i)\right]^n$$

Re-arranging so that n and $n+1$ terms are separated:

$$h_i^{n+1} - rK_{i-1/2}(h_{i-1} - h_i)^{n+1} = h_i^n + rK_{i-1/2}(h_{i-1} - h_i)^n + \omega \Delta t \frac{\rho'}{\rho}$$

$$-rK_{i-1/2}h_{i-1}^{n+1} + \left(1 + rK_{i-1/2}\right)h_i^{n+1} = rK_{i-1/2}h_{i-1}^n + \left(1 - rK_{i-1/2}\right)h_i^n + \omega \Delta t \frac{\rho'}{\rho}$$

The coefficients for the last row of the matrix become $-rK_{i-1/2}, 1 + rK_{i-1/2}$ or $rK_{i-1/2}, 1 - rK_{i-1/2}$ for X and Y, respectively. Note that there is no coefficient for h_{i+1} in the last row.

The top boundary condition requires careful consideration of the distances between elements, that $h_{i-1} = 0$, and that $K_{i-1/2} \to K_i$. Starting with eq. 13 with r factored out and geometric factors derived above for Eq. 11. For the first row:

$$\left(h_i^{n+1} - h_i^n - \omega \Delta t \frac{\rho'}{\rho}\right) = r\left[\frac{K_{i+1/2}(h_{i+1} - h_i)}{\beta_1} - \frac{K_i h_i}{\beta_2}\right]^{n+1} + r\left[\frac{K_{i+1/2}(h_{i+1} - h_i)}{\beta_1} - \frac{K_i h_i}{\beta_2}\right]^n$$

The coefficient for h_i, below. Use plus for X and minus for Y.

$$1 \pm r\left[\frac{K_{i+1/2}}{\beta_1} + \frac{K_i}{\beta_2}\right]$$

The coefficient for h_{i+1}. Use minus for X and plus for Y. There is no coefficient for h_{i-1}.

$$\mp r\frac{K_{i+1/2}}{\beta_1}$$

And for the second row:

$$\left(h_i^{n+1} - h_i^n - \omega \Delta t \frac{\rho'}{\rho}\right) =$$

$$r\left[\frac{K_{i+1/2}(h_{i+1} - h_i)}{\beta_3} + \frac{K_{i-1/2}(h_{i-1} - h_i)}{\beta_4}\right]^{n+1} + r\left[\frac{K_{i+1/2}(h_{i+1} - h_i)}{\beta_3} + \frac{K_{i-1/2}(h_{i-1} - h_i)}{\beta_4}\right]^n$$

The coefficients for h_i become $1 + r\left[\frac{K_{i+1/2}}{\beta_3} + \frac{K_{i-1/2}}{\beta_4}\right]$ and $1 - r\left[\frac{K_{i+1/2}}{\beta_3} + \frac{K_{i-1/2}}{\beta_4}\right]$ for X and Y, respectively. The immediate off diagonal components are $\mp r\frac{K_{i-1/2}}{\beta_3}$ For h_{i-1} and $\mp r\frac{K_{i+1/2}}{\beta_4}$ for X and Y.

Appendix 3.2 – Python Implementation

Python Implementation of Bethke and Corbet (1988) Sediment Compaction Algorithm

Using the algebraic approximation of the governing equation, which is eq. 13 from Bethke and Corbet (1988):

$$\frac{1}{2}[S^n + S^{n+1}]\left(\frac{h_i^{n+1} - h_i^n}{\Delta t} - \omega\frac{\rho'}{\rho}\right) =$$

$$\frac{1}{2\Delta z^2}\left[K_{i+1/2}(h_{i+1} - h_i) + K_{i-1/2}(h_{i-1} - h_i)\right]^{n+1} +$$

$$\frac{1}{2\Delta z^2}\left[K_{i+1/2}(h_{i+1} - h_i) + K_{i-1/2}(h_{i-1} - h_i)\right]^{n}$$

This model also employs values and equations from Mann and Mackenzie, 1990

```
# Import libraries here
import numpy as np
import math
import matplotlib.pyplot as plt

# Global constants here
GRAVITY = 9.81 #m/s^2
FLUID_DENSITY = 1000 #kg/m^3
```

The first step is to define an element objects for experimenting and for building stratigraphy. For experimenting we make a toy model where we can vary the values used for the element properties, sometimes beyond what is geologically reasonable, for the sake of experimenting and testing the model function. For building stratigraphy we make coarse sand, fine sand, silt, and shale elements. Model validation is discussed below. Each element object has the following properties:

- Initial porosity
- A porosity function based on effective stress
- Sediment density
- Fluid density
- Initial hydraulic conductivity
- A hydraulic conductivity function based on porosity

```
 class toy_element: # For experimenting!
    def __init__(self):
        self.initial_void_ratio = 1.174 #fine sand appendix Table 1 Mann and
Mackenzie 1990
        self.initial_porosity = self.initial_void_ratio / (1 + self.initial_v
oid_ratio) #Mann and Mackenzie eq. 10
        self.sediment_density = 2600 #kg/m^3
        self.saturated_sediment_density = (FLUID_DENSITY * self.initial_poros
ity) + (self.sediment_density * (1-self.initial_porosity))
        self.compaction_coefficient = 0.25 #fine sand appendix Table 1 Mann a
nd Mackenzie 1990
        self.permeability_A = 10e-9 #m^2, fine sand appendix Table 1 Mann and
Mackenzie 1990
        self.permeability_B = 8 #m^2, fine sand appendix Table 1 Mann and Mac
kenzie 1990
        self.ATHY_CONSTANT = 10e-5 #cm^-1?

    def porosity(self,effective_stress):
        p = self.initial_porosity * math.exp(-self.ATHY_CONSTANT*effective_st
ress/
                                             (self.saturated_sediment_density
- FLUID_DENSITY)/GRAVITY) # Bethke and Corbet, 1988 eq. 8
        return(p)

    def hydraulic_conductivity(self,effective_stress):
        p = self.porosity(effective_stress)
        k = self.permeability_A * p**self.permeability_B #Mann and Mackenzie
appendix eq. 9 for clastics
        K = k * FLUID_DENSITY * GRAVITY / 1e-3 #1e-3 kg/m-s is dynamic viscos
ity of water
        return(K)

    def rhoprime(self):
        return(self.saturated_sediment_density - FLUID_DENSITY)

    def storativity(self,effective_stress):
        p = self.porosity(effective_stress)
        S = FLUID_DENSITY/self.rhoprime() * self.ATHY_CONSTANT * p / (1 - p)
        return(S)
```

```
class coarse_sand_element: # For coarse sand / Conglomerate
    def __init__(self):
        self.initial_void_ratio = 1.174 #coarse sand appendix Table 1 Mann an
d Mackenzie 1990
        self.initial_porosity = self.initial_void_ratio / (1 + self.initial_v
oid_ratio) #Mann and Mackenzie eq. 10
        self.sediment_density = 2600 #kg/m^3
        self.saturated_sediment_density = (FLUID_DENSITY * self.initial_poros
ity) + (self.sediment_density * (1-self.initial_porosity))
        self.compaction_coefficient = 0.25 #coarse sand appendix Table 1 Mann
and Mackenzie 1990
        self.permeability_A = 10e-8 #m^2, coarse sand appendix Table 1 Mann a
nd Mackenzie 1990
        self.permeability_B = 5.1 #m^2, coarse sand appendix Table 1 Mann and
Mackenzie 1990
        self.ATHY_CONSTANT = 10e-6 #cm^-1? #from Bethke Fig 2

    def porosity(self,effective_stress):
        p = self.initial_porosity * math.exp(-self.ATHY_CONSTANT*effective_st
ress/
                                             (self.saturated_sediment_density
- FLUID_DENSITY)/GRAVITY) # Bethke and Corbet, 1988 eq. 8
        return(p)

    def hydraulic_conductivity(self,effective_stress):
        p = self.porosity(effective_stress)
        k = self.permeability_A * p**self.permeability_B #Mann and Mackenzie
appendix eq. 9 for clastics
        K = k * FLUID_DENSITY * GRAVITY / 1e-3 #1e-3 kg/m-s is dynamic viscos
ity of water
        return(K)

    def rhoprime(self):
        return(self.saturated_sediment_density - FLUID_DENSITY)

    def storativity(self,effective_stress):
        p = self.porosity(effective_stress)
        S = FLUID_DENSITY/self.rhoprime() * self.ATHY_CONSTANT * p / (1 - p)
        return(S)
```

```
class fine_sand_element: # For fine-med sands
    def __init__(self):
        self.initial_void_ratio = 1.174 #fine sand appendix Table 1 Mann and
Mackenzie 1990
        self.initial_porosity = self.initial_void_ratio / (1 + self.initial_v
oid_ratio) #Mann and Mackenzie eq. 10
        self.sediment_density = 2600 #kg/m^3
        self.saturated_sediment_density = (FLUID_DENSITY * self.initial_poros
ity) + (self.sediment_density * (1-self.initial_porosity))
        self.compaction_coefficient = 0.25 #fine sand appendix Table 1 Mann a
nd Mackenzie 1990
        self.permeability_A = 10e-9 #m^2, fine sand appendix Table 1 Mann and
Mackenzie 1990
        self.permeability_B = 8 #m^2, fine sand appendix Table 1 Mann and Mac
kenzie 1990
        self.ATHY_CONSTANT = 2*(10e-6) #cm^-1? #from Bethke Fig 2

    def porosity(self,effective_stress):
        p = self.initial_porosity * math.exp(-self.ATHY_CONSTANT*effective_st
ress/
                                             (self.saturated_sediment_density
- FLUID_DENSITY)/GRAVITY) # Bethke and Corbet, 1988 eq. 8
        return(p)

    def hydraulic_conductivity(self,effective_stress):
        p = self.porosity(effective_stress)
        k = self.permeability_A * p**self.permeability_B #Mann and Mackenzie
appendix eq. 9 for clastics
        K = k * FLUID_DENSITY * GRAVITY / 1e-3 #1e-3 kg/m-s is dynamic viscos
ity of water
        return(K)

    def rhoprime(self):
        return(self.saturated_sediment_density - FLUID_DENSITY)

    def storativity(self,effective_stress):
        p = self.porosity(effective_stress)
        S = FLUID_DENSITY/self.rhoprime() * self.ATHY_CONSTANT * p / (1 - p)
        return(S)
```

```
class silt_element: # For silt
    def __init__(self):
        self.initial_void_ratio = 1.695 #silt appendix Table 1 Mann and Macke
nzie 1990
        self.initial_porosity = self.initial_void_ratio / (1 + self.initial_v
oid_ratio) #Mann and Mackenzie eq. 10
        self.sediment_density = 2600 #kg/m^3
        self.saturated_sediment_density = (FLUID_DENSITY * self.initial_poros
ity) + (self.sediment_density * (1-self.initial_porosity))
        self.compaction_coefficient = 0.4 #silt appendix Table 1 Mann and Mac
kenzie 1990
        self.permeability_A = 4*10e-13 #m^2, silt appendix Table 1 Mann and M
ackenzie 1990
        self.permeability_B = 8 #m^2, silt appendix Table 1 Mann and Mackenzi
e 1990
        self.ATHY_CONSTANT = 5*(10e-6) #cm^-1? #from Bethke Fig 2

    def porosity(self,effective_stress):
        p = self.initial_porosity * math.exp(-self.ATHY_CONSTANT*effective_st
ress/
                                             (self.saturated_sediment_density
- FLUID_DENSITY)/GRAVITY) # Bethke and Corbet, 1988 eq. 8
        return(p)

    def hydraulic_conductivity(self,effective_stress):
        p = self.porosity(effective_stress)
        k = self.permeability_A * p**self.permeability_B #Mann and Mackenzie
appendix eq. 9 for clastics
        K = k * FLUID_DENSITY * GRAVITY / 1e-3 #1e-3 kg/m-s is dynamic viscos
ity of water
        return(K)

    def rhoprime(self):
        return(self.saturated_sediment_density - FLUID_DENSITY)

    def storativity(self,effective_stress):
        p = self.porosity(effective_stress)
        S = FLUID_DENSITY/self.rhoprime() * self.ATHY_CONSTANT * p / (1 - p)
        return(S)
```

```
class shale_element: # For shale
    def __init__(self):
        self.initial_void_ratio = 1.695 #shale appendix Table 1 Mann and Mack
enzie 1990
        self.initial_porosity = self.initial_void_ratio / (1 + self.initial_v
oid_ratio) #Mann and Mackenzie eq. 10
        self.sediment_density = 2600 #kg/m^3
        self.saturated_sediment_density = (FLUID_DENSITY * self.initial_poros
ity) + (self.sediment_density * (1-self.initial_porosity))
        self.compaction_coefficient = 0.43 #shale appendix Table 1 Mann and M
ackenzie 1990
        self.permeability_A = 4*10e-16 #m^2, shale appendix Table 1 Mann and
Mackenzie 1990
        self.permeability_B = 8 #m^2, shale appendix Table 1 Mann and Mackenz
ie 1990
        self.ATHY_CONSTANT = 10e-5 #cm^-1?

    def porosity(self,effective_stress):
        p = self.initial_porosity * math.exp(-self.ATHY_CONSTANT*effective_st
ress/                        (self.saturated_sediment_density - FLUID_DENSITY
)/GRAVITY) # Bethke and Corbet, 1988 eq. 8
        return(p)

    def hydraulic_conductivity(self,effective_stress):
        p = self.porosity(effective_stress)
        k = self.permeability_A * p**self.permeability_B #Mann and Mackenzie
appendix eq. 9 for clastics
        K = k * FLUID_DENSITY * GRAVITY / 1e-3 #1e-3 kg/m-s is dynamic viscos
ity of water
        return(K)

    def rhoprime(self):
        return(self.saturated_sediment_density - FLUID_DENSITY)

    def storativity(self,effective_stress):
        p = self.porosity(effective_stress)
        S = FLUID_DENSITY/self.rhoprime() * self.ATHY_CONSTANT * p / (1 - p)
        return(S)
```

Build Model

Once the elements objects are defined, we build the model.

```
def tridiag(a,b,c):
    # builds a triadiagonal matrix from three sets of coefficients
    # first row of a and last row of c are omitted.
    return np.diag(a[1:], -1) + np.diag(b, 0) + np.diag(c[:-1], 1)

def TDMAsolver(a, b, c, d):
    # TDMA solver, a b c d can be NumPy array type or Python list type.
    # refer to http://en.wikipedia.org/wiki/Tridiagonal_matrix_algorithm

    nf = len(a)     # number of equations
    ac, bc, cc, dc = map(np.array, (a, b, c, d))     # copy the array

    for it in range(1, nf):
        mc = ac[it]/bc[it-1]
        bc[it] = bc[it] - mc*cc[it-1]
        dc[it] = dc[it] - mc*dc[it-1]

    xc = ac
    xc[-1] = dc[-1]/bc[-1]

    for il in range(nf-2, -1, -1):
        xc[il] = (dc[il]-cc[il]*xc[il+1])/bc[il]

    del bc, cc, dc  # delete variables from memory

    return xc

class compaction_model:
    def __init__(self,element_type,deltaz):
        self.h = np.array([0,0,0]) # initial excess head = 0
        self.elements = [element_type(),element_type(),element_type()] # init
ial list of elements
        self.deltaz = deltaz # size of each complete element
        self.z = np.array([(3 - i) * deltaz + deltaz/2 for i in range(3)]) #
depth of each element center
        rhoprime = self.elements[0].rhoprime() # solid density - fluid densit
y
        self.prior_effective_stress = rhoprime * GRAVITY * self.z

    def effective_stress(self,excess_head = None):
        if excess_head is None:
            excess_head = self.h
        dstress = np.array([element.saturated_sediment_density
                            * GRAVITY * self.deltaz
                            for element in self.elements])
        stress = np.flip(np.flip(dstress).cumsum()) - dstress / 2
```

```
        effective_stress = stress - (excess_head+self.z) * GRAVITY * FLUID_DE
NSITY
        return(effective_stress)

    def storativity(self,effective_stress):
        S = np.array([self.elements[i].storativity(effective_stress[i])
                      for i in range(0,len(self.h))])
        return(S)

    def hydraulic_conductivity(self,effective_stress):
        K = np.array([self.elements[i].hydraulic_conductivity(effective_stres
s[i])
                      for i in range(0,len(self.h))])
        return(K)

    def porosity(self,effective_stress):
        phi = np.array([self.elements[i].porosity(effective_stress[i])
                      for i in range(0,len(self.h))])
        return(phi)

    def compacted_depth(self):
        p_initial = np.array([self.elements[i].initial_porosity
                      for i in range(0,len(self.h))])
        p = self.porosity(self.effective_stress())
        compacted_thickness = self.deltaz * (1 - p_initial + p)
        compacted_z = np.flip(np.flip(compacted_thickness).cumsum()) - compac
ted_thickness / 2
        return(compacted_z)

    def Lambda(self):
        dstress = np.array([element.saturated_sediment_density
                            * GRAVITY * self.deltaz
                            for element in self.elements])
        stress = np.flip(np.flip(dstress).cumsum()) - dstress / 2
        effective_stress = stress - (self.h + self.z) * GRAVITY * FLUID_DENSI
TY
        L = 1 - effective_stress / stress
        return(L)


    def run(self,new_element_type,omega,steps_per_element):
        # This function adds one element to the model and
        # iterates through the growth of this element to deltaz.
        # Longer model runs iterate on this function.

        # define model time step
        deltat = self.deltaz/omega/steps_per_element

        # define fractional element height added per time step
```

```
        fracz = self.deltaz/steps_per_element

        # Generate new element at top of section
        new_element = new_element_type()
        self.elements = np.append(self.elements,new_element)
        self.h = np.append(self.h,0)
        nelements = len(self.h)

        # Calculate increment of loading from sedimentation
        d = omega * deltat * new_element.rhoprime() / FLUID_DENSITY

        # Update prior effective stress with new element
        initial_effective_stress = (fracz * GRAVITY *
                                    new_element.rhoprime())/2
        self.prior_effective_stress = np.append(self.prior_effective_stress,i
nitial_effective_stress)

        for step in range(steps_per_element):
            # Calculate z positions for each element
            self.z = np.array([(nelements - i - 1) * self.deltaz - self.delta
z/2 + (step + 1) * fracz
                               for i in range(nelements)])
            self.z[nelements - 1] = (step + 1) * fracz / 2 # correct last (to
p) element

            # Calculate geometric correction factors for topmost elements
            zeta_1 = (step + 1) * fracz/self.deltaz
            zeta_2 = zeta_1 + 1
            beta_1 = zeta_2/8 * (zeta_1 + zeta_2)
            beta_2 = zeta_1/8 * (zeta_1 + zeta_2)
            beta_3 = 3/4 * zeta_2 - 1/2 * zeta_1
            beta_4 = zeta_2/8 * (3*zeta_2 - 2*zeta_1)

            #indices for last and second to last row
            i0 = nelements - 1
            i1 = nelements - 2

            # Calculate effective stress and estimate new effective stress
            effective_stress = self.effective_stress()
            new_effective_stress = 2 * effective_stress - self.prior_effectiv
e_stress

            # Get hydraulic conductivity between elements
            K = self.hydraulic_conductivity(effective_stress)
            Ksums = (K[:-1] + K[1:])/ 2 # mean hydraulic conductivity between
elements
            Kplus = np.append(Ksums, K[0]) # top hydraulic conductivity from
first element.
            Kminus = np.insert(Ksums,0,0) # impermeable base of model
```

```
            for iteration in range(2):
                # First iteration uses estimated effective stress, above
                # Second iteration uses newly determined effective stress fro
m first iteration

                # Estimate S n and S n+1 from rate of change of effective str
ess
                S_n = self.storativity(effective_stress)
                S_nplus1 = self.storativity(new_effective_stress)

                # Calculate coefficients
                r = deltat/(S_n + S_nplus1)/self.deltaz/self.deltaz

                # X n+1 matrix
                xa = -r * Kminus
                xb = 1 + r * (Kminus + Kplus)
                xc = -r * Kplus
                # fix last row
                xa[i0] = -r[i0] * Kminus[i0] / beta_1
                xb[i0] = 1 + r[i0] * (Kplus[i0]/beta_1 + Kminus[i0]/beta_2)
                xc[i0] = -r[i0] * Kplus[i0] / beta_1
                # fix second to last row
                xa[i1] = -r[i1] * Kminus[i1] / beta_3
                xb[i1] = 1 + r[i1] * (Kplus[i1]/beta_3 + Kminus[i1]/beta_4)
                xc[i1] = -r[i1] * Kplus[i1] / beta_4

                # Y n matrix
                ya = r * Kminus
                yb = 1 - r * (Kminus + Kplus)
                yc = r * Kplus
                # fix last row
                ya[i0] = r[i0] * Kminus[i0] / beta_1
                yb[i0] = 1 - r[i0] * (Kplus[i0]/beta_1 + Kminus[i0]/beta_2)
                yc[i0] = r[i0] * Kplus[i0] / beta_1
                # fix second to last row
                ya[i1] = r[i1] * Kminus[i1] / beta_3
                yb[i1] = 1 - r[i1] * (Kplus[i1]/beta_3 + Kminus[i1]/beta_4)
                yc[i1] = r[i1] * Kplus[i1] / beta_4

                # Build vector Y h + d
                Y = tridiag(ya,yb,yc)
                Yh_d = np.matmul(Y,self.h) + d

                # Solve linear system X^-1 [Yh + d]
                h_nplus1 = TDMAsolver(xa,xb,xc,Yh_d)
```

```
        # Find new effective stress based on h_nplus1
        new_effective_stress = self.effective_stress(h_nplus1)

        #End inner two-iteration loop

    # move excess head into current time step
    self.h = h_nplus1

    # store effective stress for next step
    self.prior_effective_stress = effective_stress

    # end fractional deposition loop
```

```
def plot_h(self):
        fig, ax = plt.subplots()
        ax.plot(self.h,self.z)
        ax.invert_yaxis()
        ax.set_xlabel('Excess Hydraulic Head (m)')
        ax.set_ylabel('Depth (m)')
        plt.savefig("ploth.svg")
        plt.show()


    def plot_K(self):
        fig, ax = plt.subplots()
        ax.plot(self.hydraulic_conductivity(self.effective_stress()),self.z)
        ax.invert_yaxis()
        ax.set_xscale('log')
        ax.set_xlabel('Hydraulic Conductivity')
        ax.set_ylabel('Depth (m)')
        plt.savefig("plotK.svg")
        plt.show()


    def plot_p(self):
        fig, ax = plt.subplots()
        ax.plot(self.porosity(self.effective_stress()),self.z)
        ax.invert_yaxis()
        ax.set_xlabel('Porosity')
        ax.set_ylabel('Depth (m)')
        plt.savefig("plotp.svg")
        plt.show()


    def plot_effective_stress(self):
        fig, ax = plt.subplots()
        ax.plot(self.effective_stress(),self.z)
        ax.invert_yaxis()
        ax.set_xlabel('Effective Stress')
        ax.set_ylabel('Depth (m)')
        plt.savefig("plotefs.svg")
        plt.show()

    def plot_L(self):
        fig, ax = plt.subplots()
        ax.plot(self.Lambda(),self.z)
        ax.invert_yaxis()
        ax.set_xlabel('Pore Pressure Ratio')
        ax.set_ylabel('Depth (m)')
        plt.savefig("plotL.svg")
        plt.show()
```

Begin Using Model

The first step is to define the model (here the variable q). Model begins with three elements of the type passed to the compaction_model class. The second parameter is the (uncompacted) thickness of each element in meters.

```
#variable = compaction_model(element_type, element_thickness_meters)
q = compaction_model(coarse_sand_element,20)
```

Run model while changing the element type, sedimentation rate, and number of elements in each step.

Begin with some coarse sand and slow deposition.

Here, we run the model for 5 loops with sedimentation rate of 0.5 mm/yr, or 0.0005m/yr. Each loop uses the run method to add a sediment element.
The run method takes the element type (a class), sedimentation rate in m/yr, and the number of steps per added element. The value after range (e.g. range(10)) is the number of elements added.

The option to plot *h* with each step is provided as a comment.

```
for i in range(25): q.run(coarse_sand_element,0.0005,10)
#q.plot_h()
```

And more sediment a little faster, this time fine sand.

```
for i in range(10): q.run(fine_sand_element,0.001,10)
#q.plot_h()
```

And a lot of sediment faster, this time fine sand.

```
for i in range(200): q.run(fine_sand_element,0.006,10)
#q.plot_h()
```

Slow things down and add shale

```
for i in range(10): q.run(shale_element,0.0002,10)
#q.plot_h()
```

Optional: Relax or "pause" sedimentation by adding sediment very very slowly to see effect on maintenance of excess hydraulic head. If using one of these steps, it is helpful to plot the previous step for comparison.

```
#for i in range(5): q.run(fine_sand_element,0.001,10)
#q.plot_h()

#for i in range(5): q.run(fine_sand_element,0.0005,10)
#q.plot_h()

#for i in range(5): q.run(fine_sand_element,0.0001,10)
#q.plot_h()

#for i in range(25): q.run(fine_sand_element,0.00001,10)
#q.plot_h()

#for i in range(50): q.run(fine_sand_element,0.000001,10)
#q.plot_h()
```

And now we plot all the things!

```
#This will also save plots based on file names specified above
q.plot_h()
q.plot_K()
q.plot_p()
q.plot_effective_stress()
q.plot_L()
```

Model Validation

Before using the model, we validate that it is working correctly by reproducing Figure 5 from Bethke and Corbet, 1988 where they plot excess hydraulic head and porosity with depth for various sedimentation rates.

First we make an element object that matches the values used in Bethke and Corbet (1988) to produce their figure 5. The properties in the validation element vary from ours, which is discussed more below.

```
class validation_element: # to validate approach by comparing to Bethke and C
orbet, 1988 Fig. 5
    def __init__(self):
        #self.initial_void_ratio = 1.174
        self.initial_porosity = 0.5 #assumed by Bethke and Corbet 1988
        #used in our model: self.initial_void_ratio / (1 + self.initial_void_
ratio) #Mann and Mackenzie eq. 10
        self.sediment_density = 3600 #kg/m^3 #value used to produce saturated
sed density of 2300 via (1000*0.5)+(3600*(1-0.5))
        self.saturated_sediment_density = (FLUID_DENSITY * self.initial_poros
ity) + (self.sediment_density * (1-self.initial_porosity))
        #self.compaction_coefficient = 0.25 #fine sand appendix Table 1 Mann
and Mackenzie 1990
        #self.permeability_A = 10e-9 #fine sand appendix Table 1 Mann and Mac
kenzie 1990
        #self.permeability_B = 8 #fine sand appendix Table 1 Mann and Mackenz
ie 1990
        self.ATHY_CONSTANT = 0.0003 #m^-1, Bethke and Corbet use 0.000003 cm^
-1. Our previous value was 10e-5, which seems like it's also in cm


    def porosity(self,effective_stress):
        p = self.initial_porosity * math.exp(-self.ATHY_CONSTANT*effective_st
ress/(self.saturated_sediment_density - FLUID_DENSITY)/GRAVITY) # Bethke and
Corbet, 1988 eq. 8
        return(p)

    def hydraulic_conductivity(self,effective_stress):
        p = self.porosity(effective_stress)
        K  = math.exp(14.3 * p - 26.30)/100*3.15e7 #Bethke and Corbet, 1988 e
q. 14
        return(K)

    def rhoprime(self):
        return(self.saturated_sediment_density - FLUID_DENSITY)
    def storativity(self,effective_stress):
        p = self.porosity(effective_stress)
        S = FLUID_DENSITY/self.rhoprime() * self.ATHY_CONSTANT * p / (1 - p)
        return(S)
```

Properties used in our elements that are not used to reproduce the Bethke and Corbet 1988 figure 5:

- initial void ratio
- compaction coefficient
- permeability A
- permeability B

We used these properties so that more element properties are calculated rather than assumed.

Properties that are different between our elements and the element used to reproduce the Bethke and Corbet 1988 Figure 5:

- porosity - we calculate a value for porosity based on the initial void ratio, they assume a value
- sediment density and saturated sediment density - they report a density that we infer is the saturated sediment density based on the text. We use a unsaturated sediment density and then calculate the saturated sediment density based on that sediment density, the fluid density, and the porosity. Using their values of fluid density and porosity, we determine that a unsaturated sediment density of 3600 kg/m^3 must be used to produce the saturated sediment density of 2300 that they report. This value is much higher than expected for the rock types represented and likely illuminates an error in the original paper where anunsaturated value was included as a saturated sediment density.
- Athy's constant - we used 10e-5, they use 3e-6 cm^-1, which must be converted to m to reproduce their plots. In the validation element this is 3e-4 m^-1
- hydraulic conductivity. We calculate K from permeability values, fluid density, and dynamic viscosity. They use an equation (their eq. 14) that is representative of marine sediment from the Gulf Coast (clay, silt, sandy clay)

Running the model with the validation element:

The model is defined four times as different variables (A,B,C, and D) for each sedimentation rate used.

Model Variable	Sedimentation Rate (m/yr)
A	0.00005
B	0.0005
C	0.005
D	0.05

As before, the model begins with elements of the type passed to the compaction_model class. The second parameter is the (uncompacted) thickness of each element in meters. Each loop uses the run method to add a sediment element. The run method takes the element type (a class), sedimentation rate in m/yr, and the number of steps per added element.

```
A = compaction_model(validation_element,20) #this sets element thickness
for i in range(500): A.run(validation_element,0.00005,10)

B = compaction_model(validation_element,20) #this sets element thickness
for i in range(500): B.run(validation_element,0.0005,10)

C = compaction_model(validation_element,20) #this sets element thickness
for i in range(500): C.run(validation_element,0.005,10)

D = compaction_model(validation_element,20) #this sets element thickness
for i in range(500): D.run(validation_element,0.05,10)
```

We then plot the results from each model and sedimentation rate together:

```
#Plot excess hydraulic head with depth for each model
fig, ax = plt.subplots()
ax.plot(A.h,A.z)
ax.plot(B.h,B.z)
ax.plot(C.h,C.z)
ax.plot(D.h,D.z)
ax.invert_yaxis()
ax.set_xlabel('Excess Head (m)')
ax.set_ylabel('Depth (m)')
plt.savefig("ploth_VABCD.svg")

#Plot porosity with depth for each model
fig, ax = plt.subplots()
ax.plot(A.porosity(A.effective_stress()),A.z)
ax.plot(B.porosity(B.effective_stress()),B.z)
ax.plot(C.porosity(C.effective_stress()),C.z)
ax.plot(D.porosity(D.effective_stress()),D.z)
ax.invert_yaxis()
ax.set_xlabel('Porosity')
ax.set_ylabel('Depth (m)')
plt.savefig("plotp_VABCD.svg")
```

This python implementation reproduces the results from Bethke and Corbet, 1988 as shown by the figure on the following page.

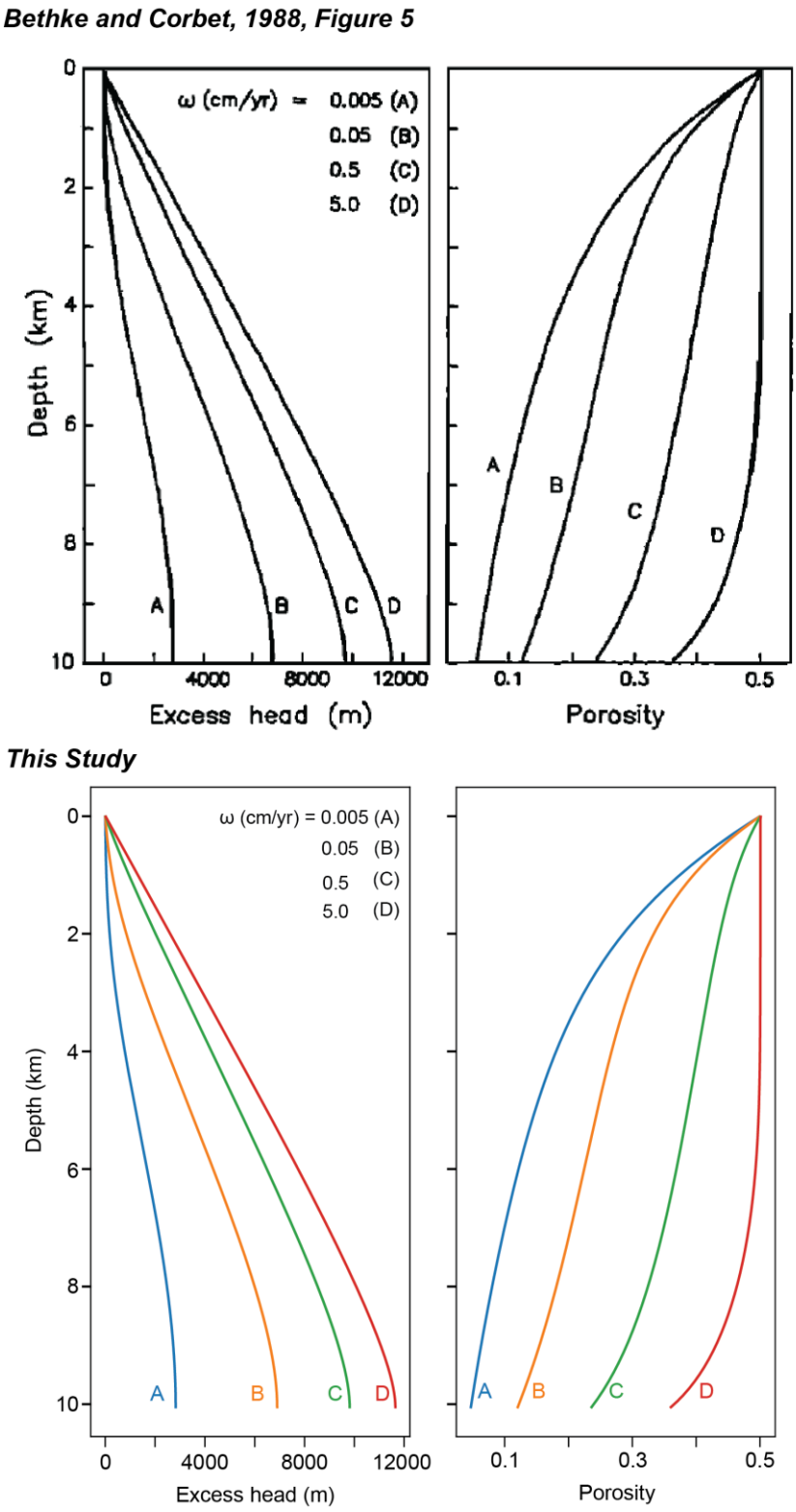

Figure A3.2. Upper plot is model results from Bethke and Corbet, 1988. Lower plot is model results using the inputs from Bethke and Corbet 1988 in the python implementation developed in this study.